Desalination of Brackish Water by a Batch Reverse Osmosis DesaLink System for use with Solar Thermal Energy

Tianyu Qiu

Doctor of Philosophy

Aston University

December 2013

Aston University

Desalination of Brackish Water by a Batch Reverse Osmosis DesaLink System for use with Solar Thermal Energy

Tianyu Qiu

Doctor of Philosophy

December 2013

For remote, semi-arid areas, brackish groundwater (BW) desalination powered by solar energy may serve as the most technically and economically viable means to alleviate the water stresses. For such systems, high recovery ratio is desired because of the technical and economical difficulties of concentrate management. It has been demonstrated that the current, conventional solar reverse osmosis (RO) desalination can be improved by 40–200 times by eliminating unnecessary energy losses. In this work, a batch-RO system that can be powered by a thermal Rankine cycle has been developed. By directly recycling high pressure concentrates and by using a linkage connection to provide increasing feed pressures, the batch-RO has been shown to achieve a 70% saving in energy consumption compared to a continuous single-stage RO system. Theoretical investigations on the mass transfer phenomena, including dispersion and concentration polarization, have been carried out to complement and to guide experimental efforts. The performance evaluation of the batch-RO system, named DesaLink, has been based on extensive experimental tests performed upon it. Operating DesaLink using compressed air as power supply under laboratory conditions, a freshwater production of approximately 300 litres per day was recorded with a concentration of around 350 ppm, whilst the feed water had a concentration range of 2500–4500 ppm; the corresponding linkage efficiency was around 40%. In the computational aspect, simulation models have been developed and validated for each of the subsystems of DesaLink, upon which an integrated model has been realised for the whole system. The models, both the subsystem ones and the integrated one, have been demonstrated to predict accurately the system performance under specific operational conditions. A simulation case study has been performed using the developed model. Simulation results indicate that the system can be expected to achieve a water production of 200 m^3 per year by using a widely available evacuated tube solar collector having an area of only 2 m^2. This freshwater production would satisfy the drinking water needs of 163 habitants in the Rajasthan region, the area for which the case study was performed.

Keywords: Brackish water; Reverse osmosis; Desalination; Batch-mode; Rankine cycle.

ACKNOWLEDGEMENTS

I am fortunate to have received such sources that made the past four year's long journey fulfilling. Completing this thesis would not have been possible without the help of numerous mentors, colleagues, friends, and family.

First and foremost, I would like to gratefully and sincerely thank Dr Philip Davies, for his help and patience, tremendously inspirational guidance and most importantly, his encouragement not only as an experimental engineer but also as an independent thinker all the way along. His extensive knowledge laid the essential foundation for this thesis, and he has been a constant source of advice and ideas. I am deeply grateful for his academic excellence and open-minded spirit, which made my Ph.D. an enjoyable journey.

I would also like to thank Dr Abul Hossain. I am immensely grateful to him for helping me to learn about those fascinating experimental aspects of desalination. Furthermore, my heartfelt gratitude goes to my brilliant collaborator, Opubo Igobo, who made significant contributions to the creation and success of this work. Without him, it would not have been even half the fun, but certainly many times the effort.

My profound gratitude goes to Zhangming Wu, Ashwatha Rajamani and Masoud Assadi and Zahran Khudzairi for all the good times that we had. I would also like to thank all the administrative and technical support staff for maintaining a pleasant working environment and helping with the system construction. Financial supports from the MED group and my company Evolve Analytics are gratefully acknowledged.

Finally, I want to thank and dedicate this thesis to my family, especially my mother. I have received nothing but uncompromising love from her, which motivated me all the way along. My last special thanks goes to Lin-jiang Chen who has always been a role model for me. I thank him for sharing the joys and tears with me.

TABLE OF CONTENTS

LIST OF TABLES

LIST OF FIGURES

LIST OF SYMBOLS

a	m	half height (or radius) of the channel
a_{Sh}		constant in Sherwood correlation
A	m^2	cross section area of channel
a_1		solar collector efficiency parameter
a_2		solar collector efficiency parameter
B		constant
b		constant
C	kg/m^3	concentration of solution
c		constant
CPF		concentration polarization factor
D	m^2 /s	diffusion coefficient
d	m	displacement
d_h	m	hydraulic diameter
F	N	force
G_Gh	W/m^2	average hourly horizontal global irradiance
h	m	height of the solute parabolic profile in a flow channel
He		Hermite polynomial function
I	W/m^2	irradiance
J	$m^3/(m^2 \cdot s)$	flux
k	m/s	mass transfer coefficient
k_{dis}	m^2/s	dispersion coefficient
K		coefficient vector
L	m	length
L_h	m	heterogeneous flow paths difference length
L_p	$m^3/(m^2 \cdot s \cdot Pa)$	membrane permeability
M	mol/m^3	molarity of the solute
$\dot{m}$	kg/s	rate of transfer of solute across the channel section
m_{in}	kg	Salt mass supplied during refill phase
m_{out}	kg	Net salt mass eluted during purging phase
n		polytropic index
n_s		number of stages
$OsmP$	Pa	osmotic pressure
P	Pa	pressure
Pe		Péclet number

P_s	m/s	salt permeability coefficient
Q	m^3 /s	flow rate
r		recovery ratio
R		rejection fraction
R^2		regression factor
Re		Reynolds number
R_{gas}	m^3/(Pa·mol·K)	gas constant
R_u	m	pump crank radius
R_w	m	power crank radius
s		number of the stage
Sc		Schmidt number
SEC	kWh/m^3	specific energy consumption
Sh		Sherwood number
t	s	time
T	K	absolute temperature
T_u	N·m	torque of linkage connection point
T_w	N·m	torque of power linkage connection point
u	m/s	crossflow velocity
$\bar{u}$	m/s	mean velocity
u_0	m/s	peak velocity
V	m^3	volume
v	m^2/s	kinematic viscosity
V_0	m^3	volume of the reverse osmosis module, or initial volume in the fluid system
$\dot{V}_p$	m^3/s	unit volume of permeate water
W	kWh	work
w	m	width of the channel
x		input variable, or longitudinal position
x_{off}	m	offset of power cylinder axis from crank pivot
y		output variable
y_{off}	m	offset of pump cylinder axis from crank pivot
z		non-dimensional position from the channel midline
α		retained salt ratio
α_u	°	pump linkage angle
α_{Sh}		constraint of the Reynolds number
α_w	°	power linkage angle
β		purge cut-off point

β_{Sh}		constraint of the Schmidt number
γ		correction coefficient for SWM channels
γ_{Sh}		constraint in the Sherwood correlation
δ	m	thickness of boundary layer
ΔP	Pa	operating pressure
η		efficiency
η_0		efficiency parameter
η_r		efficiency ratio
σ		constant to convert the concentration to the osmotic pressure
σ_1		reflection coefficient
σ_2		salt and water coupling factor
Θ	°	crank angle

Subscripts

air	air cylinder or power cylinder
avg	average
b	bulk
comp	compressor
diff	diffusive
dis	dispersion
f	feed
flu	fluid
h	hydraulic
he	heterogeneous
ini	initial
initial	the measured values at the beginning of operation
m	membrane
max	maximum
mem	membrane
o	observed
out	parameters measured at the RO module outlet
p	permeate
piston	the piston of power or pump cylinder
power	air cylinder or power cylinder
pur	purging
r	residual
res	residence

s	solute
Taylor	Taylor dispersion
theory	theoretical predicted values
u	pump linkage system
v	solvent
w	power linkage system
water	water cylinder or pump cylinder

LIST OF ABBREVIATIONS

BW	brackish water
RO	reverse osmosis
MED	multi-effect desalination
MSF	multi-stage flash
ED	electrodialysis
VC	vapour compression
RES	renewable energy sources
PV	photovoltaic
MEH	multiple effect humidification
CPC	compound parabolic collector
FPC	flat plate collector
PTC	parabolic trough collector
ETC	evacuated tube collector
ERD	energy recovery device
SEC	specific energy consumption
RC	Rankine cycle
SWM	spiral wound module
CP	concentration polarization
KS	Kimura-Sourirajan theory
SK	Spiegler-Kedem theory
OLS	ordinary least-squares
RR	robust regression
GA	genetic algorithm

Chapter 1
INTRODUCTION

The motivation and objectives of the work are introduced. The adopted methodology is described and the outline of this thesis is presented.

1.1. The motivation

1.1.1. Water crisis

Our planet is blue, however, 97.5% of Earth's water is salt water and contained in seas and oceans, which leaves only 2.5% to be freshwater. Around 70% of the freshwater represents ice and snow cover in mountainous regions, and 30% is stored underground in the form of groundwater. Less than 0.5% of the freshwater occurs in the earth's liquid surface freshwater (i.e. lakes and rivers). Seawater typically has a salt concentration in the range of 10,000 ppm (Baltic Sea) to 45,000 ppm (Arabian Gulf) total dissolved solids (TDS). Brackish ground water (BW), which is normally found as surface water in estuaries and as groundwater in salty aquifers has a salt concentration between 3,000 and 10,000 ppm. For drinking water, 500 ppm TDS is the maximum limitation with the considerations of health and taste matters (DeZuane 1997).

Humans are over-consuming freshwater resources. The inadequate access to clean and pathogen free drinking water is one of the most pervasive problems threatening people lives throughout the world (*Figure 1.1*). More than a third of the world's population already suffers from shortages of potable water. To make the situation particularly severe, in the following decades, most population growth will occur in developing countries, mainly

in regions that are already experiencing water stress and with limited access to safe drinking water (UN Water, 2012).

Figure 1.1 Spreading water shortages from (SERVICE 2006) — presently, 1 billion people do not have access to clean water; 2.3 billion people live in water-stressed areas, together with other critical *influences on freshwater resources, e.g. climate change, surging population growth, industrialization and pollutant emissions, this number expected to climb to 3.5 billion by 2025.*

1.1.2. Desalination

To address the water scarcity, a tremendous amount of research has been conducted to identify new solutions. Among them, desalination is one of the most attractive means to purify salt water at low cost and with little energy. Nowadays, desalination has become the essential to increase water supply (*Figure 1.2*).

Figure 1.2 Over the past 50 years, the world wide desalination capacity had increased exponentially. Nowadays, there are almost 16,000 desalination facilities contributing to the enormous capacity of 64 million m^3/d. Additionally, 3,800 worldwide plants are now considered to be offline or decommissioned, making up 6.4 million m3/d of old capacity. According to the Global Water Intelligence report, the global water production by desalination is expected to be twice of this capacity in 2015 (Schiermeier 2008).

In 1990s, the multi-stage flash (MSF) water desalination has made an essential contribution in the production of freshwater for some of the gulf cooperation council (GCC) countries (including Saudi Arabia, Kuwait, the United Arab Emirates, Qatar, Bahrain, and Oman) (*Centre, Zones et al. 2001*), followed by reverse osmosis (RO) desalination technology. Nowadays, the volume of desalinated water for GCC countries has been doubled since 1990 (*Figure 1.3*). In addition, RO technology has taken over the dominant position from MSF because of its high energy efficiency and low cost (*Figure 1.3*) (Shafaghat et al 2012). Soon, the UAE will commission the world's largest solar-powered RO desalination plant which will process more than 100,000 m^3 of potable water per day. One of the project leaders said: ‘‘the gulf countries have abundance of sunshine throughout the year and the plant aim will be to harness this free energy and channel it to UAE residents at extremely low cost.’’ (ZeeNews, 2013).

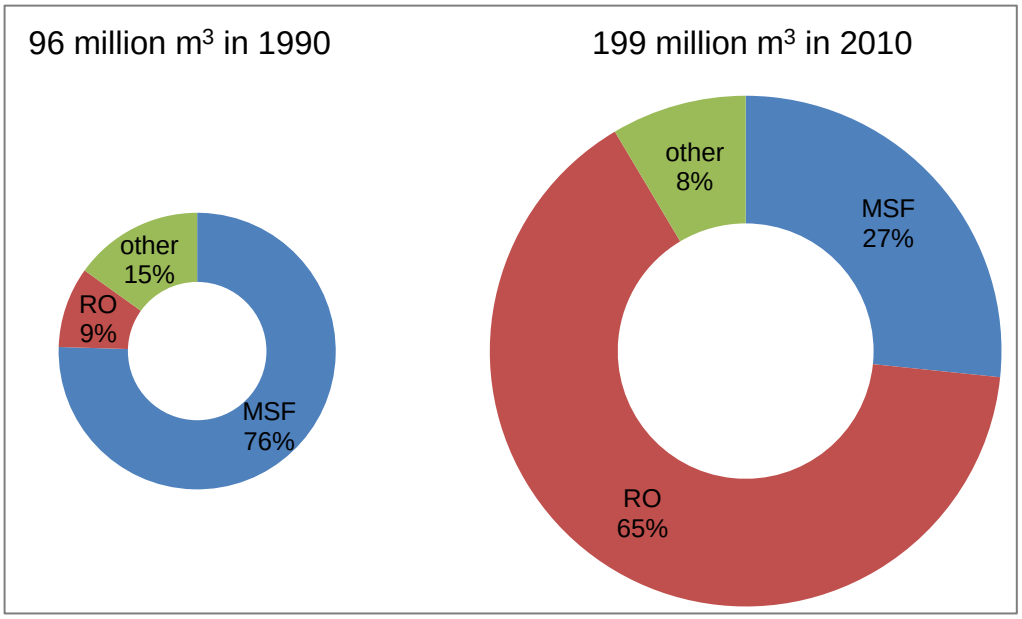

Figure 1.3 Total volumes of desalinated water in GCC countries in 1990 and 2010, based on information from (Centre, Zones et al. 2001; Dawoud 2012)

1.1.3. Inland desalination

Similarly, for inland, semi-arid regions far from the coast but with adequate brackish ground water (BW), desalination is urgently needed to increase the water supply necessary to support inhabitants, sustain agriculture and promote economic development. With appropriate implementation, the desalination system may make good use of the brackish water resources available in inland regions of some developed countries, such as India, China, or even rich countries, like U.S (*Figure 1.4*). Take reverse osmosis (RO) technology as an example, owing to its comparably low energy consumption, the implementation of BWRO desalination systems in such regions usually costs far less than freshwater transport from coastal regions in U.S. by truck or pipeline (Zhou and Tol 2005, Karagiannis and Soldatos 2008).

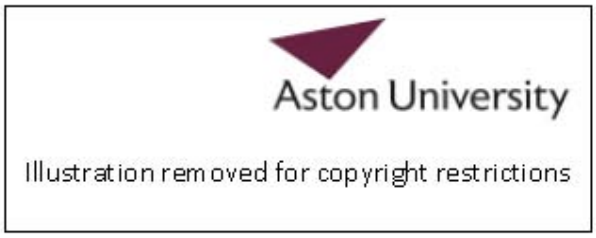
Aston University
Illustration removed for copyright restrictions

Figure 1.4 (a) Depth to saline ground water in the U.S.; (b) Total dissolved-solids (TDS) concentrations of brackish water in different locations, TDS (selected area: Arizona and New Mexico) is typically less than 1,000 ppm, but can be much higher in some inland areas (Alley 2003).

Brackish ground water (BW) resources have various compositions depending on the location (see *Appendix A.3*) (Van Weert, van der Gun et al. 2009). For example, in *Figure 1.4*, areas of higher concentrations include: low parts of some basins where dissolved solids are concentrated by evapotranspiration from shallow ground water; basins with smaller fluxes of water naturally circulating through the ground-water system, near deposits of saline minerals; and areas of salt buildup from intensive irrigation (Alley 2003). Appropriate pre-treatment process utilizing either chemical or membrane filtration should be designed according to the BW composition, to reduce the RO membrane fouling or scaling potential.

1.1.4. Concentrate disposal and management

Almost every water resource management method raises environmental sustainability concerns; inland BWRO desalination is no exception. One of the major concerns critical to the wider use of current desalination systems is addressing the environmental issues of concentrate and salt disposal. For RO desalination plants in coastal area, the concentrate can be directly discharged to the sea with little environmental concern due to the vast seawater resource. On the other hand, for the concentrate from inland BWRO systems, instead of direct disposal, which has an unacceptable impact on groundwater resource, the concentrate will be evaporated to reduce its volume prior to disposal. The concentrate disposal options include surface water discharge, sewer discharge, and land application can increase the salt load level in the receiving water and soil, which contaminates water resources and reduces soil fertility. The other methods, such as deep well injection and evaporation ponds, not only depend on the plant location, but more importantly, they require high technical condition (Xu, Cath

et al. 2013). The cost of brine disposal can vary considerably depending on the method employed and it is site-specific. It is reported the cost of RO concentrate treatment is estimated at 5–33% of desalted water cost (Turek, Was et al. 2009). This concentrate management problem is magnified in less developed countries, due to the inevitable dilemma between sacrificing the environment and financially burdening the high technical operation.

Current research is focused on reducing the impact of RO concentrates by reducing the volume and/or by diminishing the pollutant load of these concentrates (Pérez-González, Urtiaga et al. 2012). As shown in *Table 1.1*, the current common solution is evaporation ponds, however, it is problematic because of the large land requirement and evaporation condition limitation. Therefore, it is desired to build a BWRO system with high recovery ratio, to reduce the concentrate volume.

Table 1.1 Evaluation of viability of treatment technologies applied to RO desalination concentrates, adapted from (Pérez-González, Urtiaga et al. 2012, Subramani and Jacangelo 2014)

Technology	Technological maturity	Operation drawbacks and economic considerations
Evaporation ponds	Industrial application	▪ Large land areas ▪ Low productivity ▪ Moderate investment and maintenance cost
Wind aided intensified evaporation	Pilot plant scale	▪ Industrial feasibility not proved ▪ Moderate investment cost
Membrane distillation	Laboratory level	▪ Difficult operational control ▪ Scaling and fouling ▪ Moderate energy consumption
Liquid-liquid extraction	Laboratory level	▪ Several treatment stages ▪ Extractants consumption
Forward osmosis	Laboratory level	▪ Limited full-scale application ▪ Low operational flux when compared

		to RO resulting in high footprint requirement

1.1.5. Solar thermal desalination

Desalination is recognized as an energy intensive process. It is estimated that about 203 million tons of oil per year is required to produce 8030 million cube meters per year (m^3/yr) desalted water (Kalogirou 2005). With consideration of the practical energy issues that relate to most water shortage areas, e.g. limited electrical supplies, soaring energy prices and the sustainable development intention (minimizing the use of fossil fuels which impact on the environment), a desalination system powered by a renewable energy source is both economically and environmentally favourable.

One of the most promising combinations of renewable energy sources (RESs) and desalination is solar RO technology (Li, Goswami et al. 2013), which includes photovoltaic (PV) RO and solar thermal RO. Currently, the PV-RO combination is particularly popular, accounting for almost two-fifths of all the solar powered desalination processes (Ali, Fath et al. 2011). Despite the continuous improvement in PV solar cells' performance, the high investment costs for PV modules which is about 3 dollars per watt-peak ($/Wp), low efficiency (10% for the polycrystalline-based solar panels) and the solar panel efficiency degradation (usually 3% in the first year) still hinder their application for inland BWRO desalination. Conversely, another combination —solar thermal Rankine Cycle (RC) RO technology— starts to show its great advantages over the PV-RO systems. Such systems exhibit great flexibility, automatic and continuous operation, low maintenance requirements and long lifetime (Ali, Fath et al. 2011). More importantly, the ability of RC-RO to be combined with different grades of input heat (depending on system requirements) (Delgado-Torres and García-Rodríguez 2012) is a distinct advantage, as the RC-RO desalination system can be a part of a co-generation system, e.g. recovering the industry waste heat for water production. Some preliminary solar RC-RO studies have shown the system efficiencies are comparable with PV-RO systems (around 15%,

Rankine cycle efficiency more than 20%), but lower specific capital cost (around 0.95 $/m^3, depends on solar collector types and RC configurations, maintenance and operation requirements (Nafey and Sharaf 2010, Li, Besarati et al. 2013). Therefore, solar thermal RC-RO system is preferred in this project. However, a principal drawback in using the steam RC at small scales is that the steam turbines tend to become unattractive at the low power outputs due to the large blade friction losses and leakage losses. Another possible alternative of the expansion mechanism is to use a piston to expand the steam (e.g. steam pump). The disadvantage with steam pumps is that the force provided by the power piston varies as the piston moves over its cycle. To overcome these disadvantages, new solutions and designs are proposed and examined in this project. Furthermore, in view of the above, this work also focuses on achieving high recovery ratio with low energy consumption along the process of solar RC-RO system development.

1.2. Proposed Work

As discussed above, the research work described in this thesis comprises both theoretical and experimental studies of a stand-alone, small-scale BWRO desalination system powered by solar thermal energy. Reverse osmosis (RO) was used because of its high energy efficiency (Li, Goswami et al. 2013). The configurations of this proposed system can be distinguished from the conventional ones in several aspects, including operating RO system in a batch mode, utilizing mechanical power directly, and so on. The main concept of designing such a system involves the ability of operating efficiently from a solar power supply that is of variable and of low thermodynamic quality and re-using of the high pressure energy contained in the rejected concentrate, therefore, the system can achieve high recovery without the necessity of extra energy. Particular focus on system design and optimisation were supported by theory and modelling. Such a system is certainly attractive for providing safe drinking water for small and medium communities in semi-arid remote regions, because of its technological and commercial feasibilities.

1.3. Origins of the project

The Science Bridge Project was initiated in 2009 as collaboration between several UK Universities research groups and Indian Partners, i.e. Indian Institute of Technology Delhi (IITD). The project had the overall objective to implement efficient decentralised bio-energy systems that would be operated using renewable fuel sources. The initial focuses of the project were on implementing a hybrid solar-biomass energy plant using a steam turbine in India, assessing the scope for using wasteland and wastewater resources to cultivate energy crops in selected areas of India. As the project developed, the analytical data of the local ground water samples from the Rajasthan region of India indicated that the ground water was in general alkaline in nature and the electric conductivity of the ground water resources varied from 810 to 9200 micro-Siemens per centimetre (µS/cm) (i.e. 400 to 5000 ppm). Because much of the ground water is brackish (>3000 ppm), and in view of the inadequate water supply for local communities, the group pursued the idea of using solar thermal energy or bioenergy to power BWRO desalination systems to increase freshwater supply for the region. With huge interests in water treatment and environmental protection in general, the author joined the Davies research group in 2010 and focused on developing a novel solar energy powered RO desalination system with an improved performance compared to most traditional solar BWRO systems. The initial objectives of the Science Bridge Project provided not only the foundation but also motivations for this project, especially in the aspect of developing a small scale BWRO system that can be combined with low grade heat sources. The emphasis, which evolved during this work, on energy losses of current market available systems facilitated the herein proposed innovative designs. The newly developed system is named DesaLink.

1.4. Aims and objectives

The aim of this thesis is to define and develop a solution for desalination of brackish groundwater, suitable for use with low grade thermal energy such as solar energy. That is an improvement on the state-of-the-art with regard to energy efficiency

and recovery. To achieve this aim, the following specific objectives need to be accomplished:

1. Review the state-of-the-art in solar powered desalination technologies, to critically assess and evaluate current popular solar RO systems and compare their performances, e.g. energy efficiencies to the theoretical ideal limit (related to *Chapter 2*).
2. Understand the loss mechanisms in solar powered desalination systems with focus on solar thermal systems (related to *Chapters 2*).
3. Compare different configurations of RO system with regard to efficiencies and recovery ratios, including multistage systems, system with and without energy recovery and batch or closed circuit systems (related to *Chapter 3*).
4. Study in-depth specific loss mechanisms in the batch-RO system associated with solute transfer (longitudinal dispersion and concentration polarization) through theory and experiments (related to *Chapters 5 and 6*).
5. Develop a practical system based on batch mode RO (the DesaLink system) and characterise its performance through experimentation and modelling (related to *Chapters 4 and 7*).
6. Apply the model to a specific case study of practical interest and investigate the influence of design parameters (related to *Chapter 8*).

1.5. Overall approach

The development strategy consists of the following stages: (i) defining a preliminary configuration for the system with the main objective being to reduce the number of energy conversion steps. (ii) establishing satisfactory mathematical models for each of the constituent subsystems and applying the models to help evaluate and optimize the system configuration parameters; (iii) pre-testing, building and testing a prototype system in the laboratory; (iv) proposing and refining mathematical models of the components of the system on the basis of the detailed laboratory testing results; and (v) combining the individual models via implementing a control strategy to build a full model

which characterizes and quantifies the produced freshwater throughout the system operation process with respect to the variations in solar irradiance from an hour-by-hour prediction to a whole year.

1.6. Achievements

The most significant contribution of this work is the design, construction and optimization of a novel functional BWRO system, without the need for separate energy recovery devices, which is achieved by a batch-RO operation and a mechanical energy transfer mechanism. Other achievements include the development and implementation of the theoretical models of dispersion and concentration polarization related to RO performance, the analysis and modelling of the DesaLink performance on site, and implementation of the system control strategy.

1.6.1. Publications

The publications and presentations are listed as follow:

T. Qiu and P. A. Davies (2011), ‘’The scope to improve the efficiency of solar-powered reverse osmosis’’, *Desalination and water treatment* 35(1-3): 14-32. This work was presented at the 3rd Oxford Water and Membranes Research Event, Oxford, UK (12–14 September 2010). The main content of this paper is reflected in *Chapter 2*.

T. Qiu, P.A. Davies and O. Igobo, a poster presentation on “Preliminary design study of a novel solar thermal-powered brackish and groundwater reverse osmosis system” on 1st International Conference on Desalination and Environment: A Water Summit, Abu Dhabi, UAE (29 Octorber–01 November, 2011).

T. Qiu, O. Igobo and P. A. Davies (2012), ‘’DesaLink: solar powered desalination of brackish groundwater giving high output and high recovery’’, *Desalination and Water Treatment*. The main content of this paper is reflected in *Chapters 3* and *4*.

T. Qiu, and P. A. Davies (2012), ‘’Longitudinal dispersion in spiral wound RO modules and its effect on the performance of batch mode RO operations’’, *Desalination* 288(0): 1-7. The main content of this paper is reflected in *Chapter 5*.

T. Qiu and P. A. Davies (2012), ‘’Comparison of Configurations for High-Recovery Inland Desalination Systems’’, *Water* 4, no. 3: 690-706. The main content of this paper is reflected in *Chapter 3*.

1.7. Outline of Thesis Structure

The structure of this thesis is illustrated in *Figure 1.5*, followed by detailed information about each chapter.

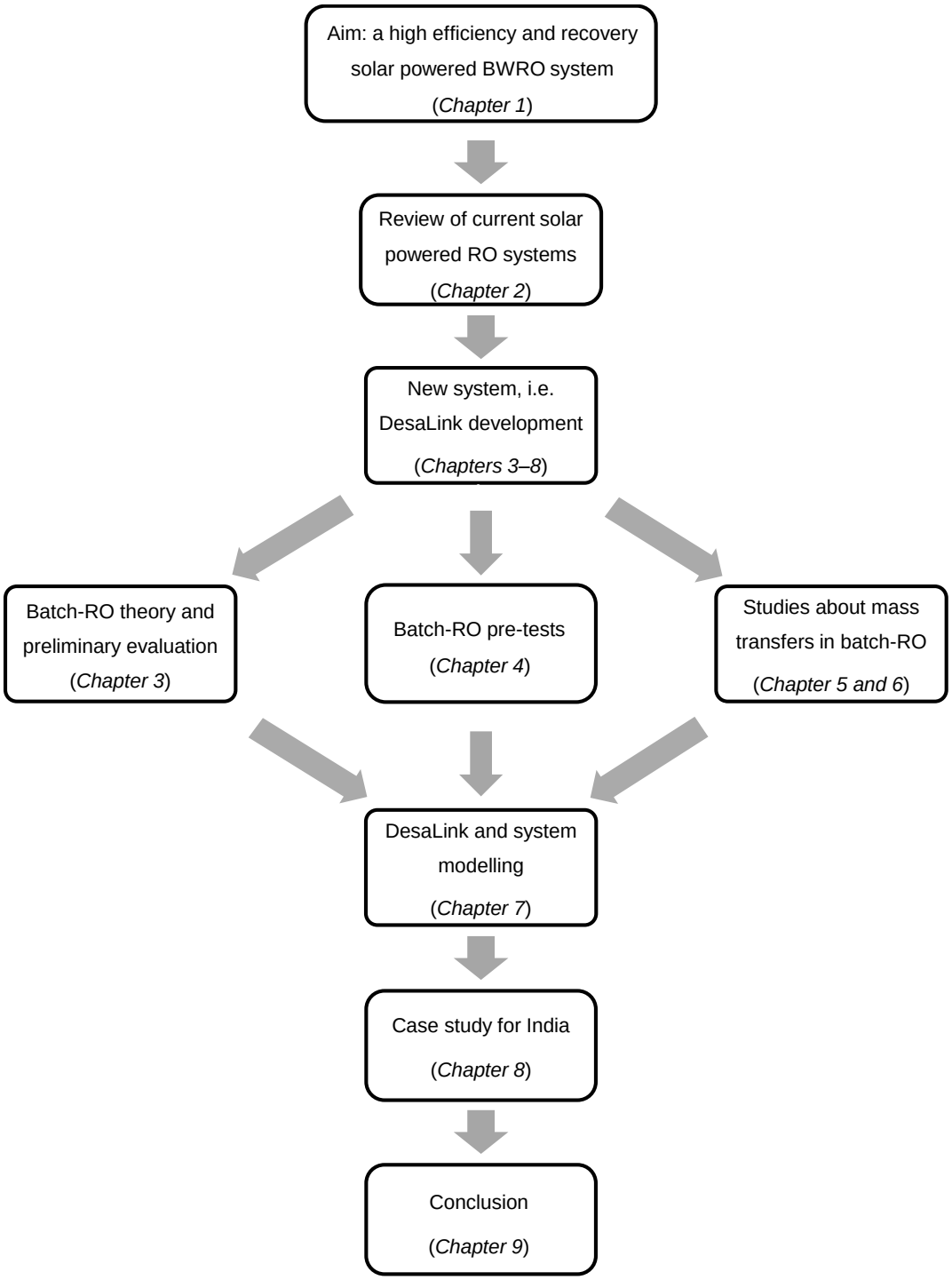

Figure 1.5 Thesis structure and the relation among chapters

In *Chapter 1*, the motivation and scope as well as the objectives of the work are introduced. The main achievements are presented.

In *Chapter 2*, a literature review that introduces main desalination technologies is presented. Emphasis is placed on RO systems and their viability of integration with solar power.

In *Chapter 3*, the concept of the batch-RO configuration is introduced. System components are described and their theory of operation is outlined. The energy efficiency of the system is analysed and compared with other high performance system designs. The comparison results are used as a guideline for the development of DesaLink.

In *Chapter 4*, the construction of the DesaLink prototype is presented. Preliminary results are reported and analysed in light of the expected system behaviour derived from the performance predictions discussed in the preceding chapters.

In *Chapters 5* and *6*, two phenomena (namely, dispersion and concentration polarization) that occur during batch-RO operation are described. The energy consumption related issues are analysed in detail, the prediction models are built and discussed. Based on the models, the operation of batch-RO is optimized; moreover, the models are implemented in the final full model of DesaLink.

In *Chapter 7*, the experimental work is extended. Models of individual subsystems are built based on physical relations between input and output parameters, and models are then validated by experiments results. The full model that combines the individual model is implemented within the Matlab®/Simulink® environment. The full model is thereafter refined, validated and optimised through extensive testing of DesaLink.

In *Chapter 8*, a case study is presented, demonstrating the system performance in a practical situation (Rajasthan region, India). The full model is adopted, together with a new model component dealing with solar thermal cycle using thermodynamic analyses.

In *Chapter 9*, conclusions drawn from this work are presented. The results obtained experimentally and computationally are discussed, highlighting the significance of the observations and measurements. Main contributions to the scientific objectives

outlined in *Section 1.4* are summarized. Recommendations for possible continuations of the current work are made.

Chapter 2
A REVIEW OF DESALINATION SYSTEMS USING RENEWABLE ENERGY

A literature review that examines some of the prototypical desalination technologies and their ability of being combined with renewable energy sources is presented. Special attention is given to solar photovoltaic and solar thermal powered reverse osmosis systems, as they are of primary interest and relevance to this work. An analysis of the energy efficiency in ideal systems and of the energy losses in real systems provides the motivation behind the engineering developments of the project.

As discussed in the previous chapter, there is an urgent shortage of freshwater in many world regions. Desalination of seawater or brackish groundwater can help satisfy such growing needs. Desalination is an energy-intensive process and, therefore, a sustainable energy provision is highly desirable. In this chapter, we review the state-of-the-art in solar-powered desalination technologies.

2.1. Desalination techniques

Desalination processes can be classified according to the types of energy sources such as (i) thermal energy, for example multi-effect desalination (MED) and multi-stage flash (MSF) technologies; (ii) electrical energy, for example electrodialysis (ED) technology and (iii) mechanical energy, for example reverse osmosis (RO) and vapour compression (VC) technologies. Since the successful commercialization of RO technology in the early 1970s, it has been rapidly overtaking the thermal desalination market, thanks to its relatively low initial investment, plant modularity, reduced environmental impact and short construction times (Fritzmann and Löwenberg et al. 2007; Cipollina et al. 2009). Currently, RO is a major

desalination technology, parallel to thermal distillation technologies (*Figure 2.1*). It already accounts for 43% of the installed capacity and tends to increase substantially in the future (Loo et al. 2012).

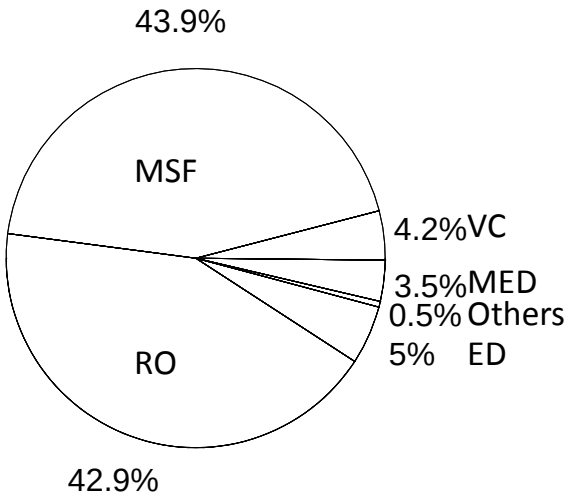

Figure 2.1 Distribution of global desalination production capacity by process technology

2.1.1. Reverse osmosis

Reverse osmosis (RO) desalination is a membrane separation process. The mechanism of this technology is better described by comparing with the direct osmosis phenomenon. The direct osmosis phenomenon (*Figure 2.2*) arises when two solutions of different concentration are separated by a semi-permeable membrane (allows the passage of the solvent and not of the solute). Due to the difference in the chemical potentials across the membrane, the solvent spontaneously moves through the membrane to the high solute concentration side until the equilibrium of chemical potential between the two sides is reached. The osmotic pressure $OsmP$ is defined to be the pressure required to maintain equilibrium, with no net movement of solvent. Besides, a small amount of the solute is transported (from the high concentration side to the other) through the membrane via diffusion, since semi-permeable membranes cannot reject 100% of the solute in practice. On the contrary, the reverse osmosis phenomenon is created by applying an external pressure P which is larger than the osmotic pressure $OsmP$ to the higher concentration side.

Consequently, the direction of the solvent flux is reversed and the solute passing through the membrane is driven by both diffusion and convection.

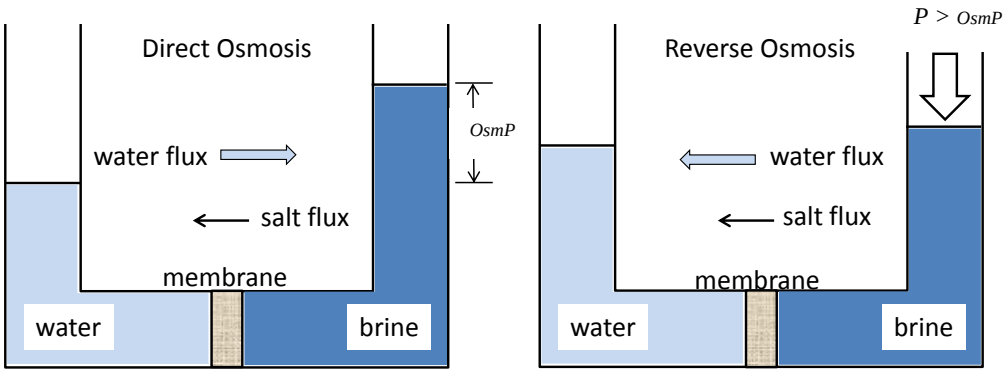

Figure 2.2 Schematic drawing of direct and reverse osmosis phenomena

2.1.2. Desalination technologies comparison

Conventional thermal desalination processes are inefficient in terms of energy usage and suffer particularly from corrosion and scaling. For the RO process, there are no water phase changes, all energy is used to provide pressure to the saline feed and high pressure energy in concentrate can be recovered. Additionally, pressure recovery is adoptable for RO process, Therefore, to achieve the same production of freshwater the overall energy consumption of RO is much lower than the thermal desalination technologies as indicated in *Table 2.1*. Since RO is currently considered the state-of-the-art desalination technology and has been shown to exhibit many advantages over the more conventional techniques, it was the chosen system of interest to be subjected to extensive study in this thesis. Detailed discussions on the various aspects of the RO desalination are provided in the following, respective sections.

Table 2.1 Comparisons of desalination processes (Cipollina and Micale et al. 2009,

Karagiannis and Soldatos 2008*)*

Features	MSF	MED	RO
Global energy consumption	high (15-17 kWh/m^3)	medium (10-14 kWh/m^3)	low (2-6 kWh/m^3)
Capital and maintenance Cost[a]	medium (0.52–1.75 \$/m^3)	medium (0.52–1.95 \$/m^3)	low (0.26–1.72 \$/m^3)
Tolerance to feed water quality	high	medium	low
Adaptability to scaling	low	low	low
Product water quality	very high (2-5 ppm)	very high (2-5 ppm)	drinking (300-400 ppm)
Investment costs	medium/high	medium	low
Easy of operation	good	good	very good
Environmental impact	medium	medium	low

[a] Depend on the size of the plant

2.2. Renewable energies for desalination

Desalination is an energy intensive process. Enormous amounts of thermal and/or electric energy consumed not only lead to high costs, but also result in large emissions of air pollutants and greenhouse gases that further exacerbate climate change. Thus, instead of using substantial quantities of fossil fuels to power desalination systems, the use of renewable energy such as solar that is usually available in abundance in arid areas is the alternative solution and, more importantly, can constitute an environmentally friendly and sustainable development.

Most renewable energy sources (RES's) are directly or indirectly produced by the sun, including: solar thermal and photovoltaic (PV) energy, wind energy, bioenergy and so on. Some of the most promising combinations of renewable energy source and desalination are shown in *Figure 2.3*. The most adopted RES is clearly solar energy, and its combination with desalination technologies accounts for 70% of all the RES powered desalination

processes *(Eltawil et al. 2009)*. Among them, the PV-RO combination is particularly popular, especially for small and medium-scale applications.

Figure 2.3 the combinations of renewable energy sources and desalination technologies (Eltawil et al. 2009)

Depending on the local resources and the desalination process in use, energy may be required in the form of either heat, electronic power or even a combination of both. Thus, hybrid desalination plants, i.e., thermally enhanced electric-powered desalination, have also been demonstrated. The hybrid system consumes less electrical energy per unit of product water, while achieving higher water recoveries than can RO alone (El-Ghonemy 2012). However, it inherently requires much higher capital and maintenance costs, which inevitably hinder its wider application.

2.2.1. Solar RO desalination systems

These systems involve either solar collectors or solar photovoltaic (PV) panels to gather solar thermal energy or generate electricity. Solar-driven RO desalination technology has been developed since the 1980s (Delgado-Torres and García-Rodríguez 2007). Both of solar thermal and PV energies have been implemented with the state-of-art RO technology (Ghermandi and Messalem 2009). Detailed overviews of PV-RO and solar thermal RO desalination are presented in *Section 2.4* and *2.5* respectively.

2.3. Energy losses in RO desalination

2.3.1. Theoretical energy limit

The ideal RO desalination process could be considered as a batch system as depicted in *Figure 2.4*. The piston is the semi permeable membrane. As the piston is pushed towards the right side, only freshwater flows through the membrane, while salt is rejected. Assuming such an ideal batch RO system has 100% salt rejection and performs without any leakage, pressure or frictional losses, it will consume a theoretical minimum energy when desalinating a portion of salt solution. Ideally, this theoretical minimum work would only depend on the osmotic pressure $OsmP$ of the solution and the recovery ratio r, but needless to say, it cannot be achieved in practice. Nevertheless, the theoretical minimum energy consumption provides a standard value against which to evaluate the performance of practical RO systems.

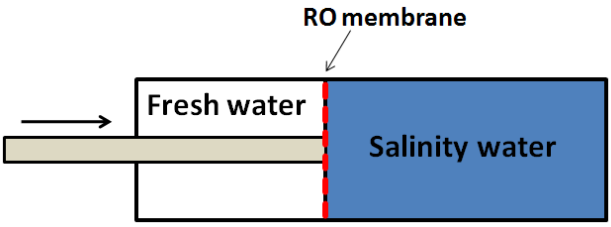

Figure 2.4 An ideal RO batch desalination system

For minimum energy consumption, the pressure applied to the solution should be just sufficient to overcome the osmotic pressure. Since the bulk concentration increases as freshwater is extracted through the RO membrane, the osmotic pressure $OsmP$ of the solution increases correspondingly; thus, the theoretical energy of desalination depends not only on the osmotic pressure but also on the fractional recovery r of pure water removed from the solution (i.e. $r = volume\ of\ pure\ water\ obtained / volume\ of\ feed\ saline\ water$). If the water permeating the membrane is completely free of salt, the theoretical minimum work W to desalinate a volume V of feed solution is given by:

$$W = \int p \cdot dV = \int_{V_1 \cdot (1-r)}^{V_1} \frac{nR_{gas}T}{V} \cdot dV = OsmP \cdot V \cdot \ln\left(\frac{1}{1-r}\right) \quad (2.1)$$

So, the ideal specific energy consumption (*SEC)* corresponding to mechanical work (or electricity) for desalinating unit volume of recovered solution is:

$$SEC = OsmP \cdot \frac{1}{r} \ln \frac{1}{(1-r)} \quad (2.2)$$

Thus, the ideal solar energy usage SEC_{ideal} is:

$$SEC_{ideal} = OsmP \cdot \frac{1}{r} \ln \frac{1}{(1-r)} \frac{1}{\eta_{solar}} \quad (2.3)$$

where η_{solar} is the ideal efficiency of solar energy conversion to mechanical work, which is equal to 86.8% (de Vos 1980).

For instance, ideally, to desalinate 1 m^3 of freshwater from Mediterranean seawater with concentration of 35,000 ppm, i.e. osmotic pressure is around 27 bar, at recovery ratio of 25% will require at least 0.94 kWh of solar energy (note: pre-treatment energy consumption is not considered here), which indicates that in a sunny coastal location receiving 7200 MJ/m^2/year, 1850 m^3 of water per year per m^2 of land covered by solar collectors could theoretically be desalinated. To desalinate brackish water of 3000 ppm, 11570 m^3 of freshwater could theoretically be obtained under the same conditions. According to the U.S. Environmental Protection Agency, drinking water per person per day must be at least 2 litres. If the ideal solar-RO system is realized, only 1 m^2 of land is required to provide enough solar energy to produce an abundance of clean water from brackish water for 5785 people,

In practice, the electrical energy requirement for seawater RO desalination systems coupled with renewable energy is usually in the range 7−15 kWh/m^3. With energy recovery devices (ERDs), this value can only be reduced to around 5 kWh/m^3. And for brackish water, the minimum specific energy usage for feed water of osmotic pressure 2.7 bar with 70% recovery ratio is 0.15 kWh/m^3. Nevertheless, the practical energy needed is 1−3 kWh/m^3 (Laborde et al. 2001; Al-Karaghouli et al. 2010).

The higher practical energy consumption is because of various energy losses which are associated with the fact that the pressure needed in the RO system is, in practice, significantly greater than the ideal minimum. For a practical example, for Mediterranean seawater (salinity of about 35000 ppm) osmotic pressure (when at equilibrium with freshwater) is around 27 bar, whereas in RO units pressures higher than 60 bars are usually adopted. These losses include: inverter and pump loss, concentrate loss, high-pressure pipe losses and hydraulic friction (*Figure 2.5*). The detailed information about these losses and the recommendations to minimise them were presented in the author's earlier paper (Qiu and Davies, 2010). Here, only longitudinal concentration loss and concentration polarization loss were introduced and discussed (*Sections 2.3.2* and *2.3.3*), as they are highly related to this research.

To identify the performance of practical solar-powered RO desalination systems, the following sections are going to review several noteworthy solar PV-RO and solar thermal-RO desalination systems, with particular focus on comparing their performances with the ideal cases. Further, by evaluating the various losses occurring in the RO and the losses in PV and Rankine cycle subsystems consecutively, recommendations will be made for minimising energy losses, and ultimately increasing the overall brackish water RO system efficiency.

Figure 2.5 Sankey diagram illuminates various energy losses in BWROs system without ERDs

2.3.2. Losses due to longitudinal concentration increase

In RO separation, there occurs a longitudinal gradient of concentration (*Figure 2.6*) as the water is progressively removed from the solution while it moves along the membrane channel. Moreover the water pressure drops along the channel. The osmotic pressure increases with the increasing longitudinal concentration of the feed solution. Therefore, in order to maintain a flux of water over the entire membrane surface, the solution must be pressurised according to the concentration at the outlet of membrane channel, even though this exceeds the pressure required at the inlet where the concentration is the least.

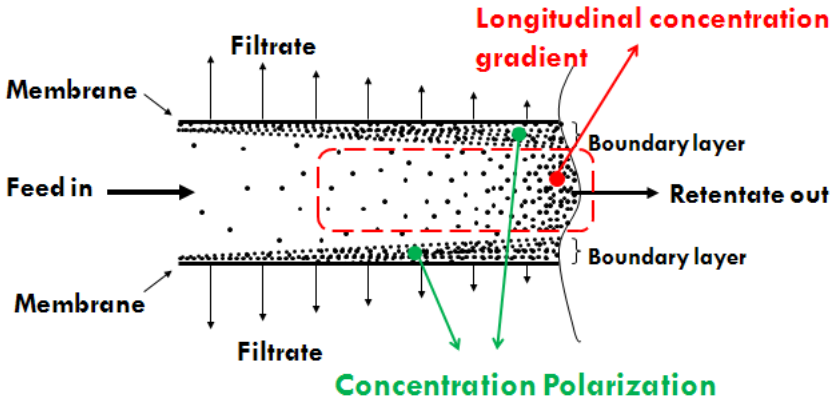

Figure 2.6 The phenomenon of longitudinal concentration gradient and concentration polarization in membrane filtration

One possible approach to minimize the effect of longitudinal concentration gradient is to divide one whole channel into several stages in series, with intermediate pumps to apply the appropriate pressure to each one. This mode of operation allows smaller volumes of water to be brought to higher pressures, thereby consuming less energy (Elimelech and Phillip 2011). Another better way is using batch-RO design, that can achieve same outcome but eliminating the intermediate pumps and RO modules. The mechanisms and comparisons of these two designs that intend to decrease longitudinal concentration related energy loss are discussed in greater details in *Chapter 3*.

2.3.3. Losses due to concentration polarization

Aside from the longitudinal gradient of salt concentration mentioned in the last section, there also occurs a transverse gradient of salt concentration. In the RO process, the flux of water through the membrane results in a build-up of salts near the membrane surface (*Figure 2.6*). Thus, the salt concentration near the surface of the membrane exceeds that in the bulk of the solution by a factor CPF. This transverse gradient of concentration across the channel enclosed by the membranes is referred to as concentration polarisation (CP). Since the osmotic pressure is, to a good approximation, proportional to the concentration it can be expected that the required operation pressure will be increased by the factor CPF, and the pumping power will be increased correspondingly. Moreover CP can cause many other negative effects on the RO process (Merten 1963; Brian 1965), such as decreasing permeate fluxes, increasing salinity of the product water, leading to membrane fouling and thus decreasing membrane lifetime.

Based on the mechanism, there are two types of method that could be adopted to reduce CP: (1) increasing membrane cross flow velocity, in other words, increasing applied pressure, but this requires more energy and may be limited because of the pressure drop along the channel, and (2) increasing mass transport, which can be done by new design concepts of RO modules, such as adding turbulence promoters, rotating and vibrating membranes. More analyses about CP and the method to reduce it for the studied system in this thesis were presented in *Chapter 6*.

2.4. PV-RO systems

PV-RO systems for SW and BW desalination which were built in the last 10 years and exhibited relatively good performance are reviewed in *Table 2.2*. Based on the assumptions mentioned before, the theoretical minimum energy usage for every PV-RO system can be obtained from *Eq. (2.3)*. *Table 2.2* shows that even the best existing systems may theoretically be improved some 40 times for seawater and 200 times for brackish water (indicated by efficiency ratio). The reasons for the low efficiency ratio of such PV-RO systems are mainly twofolds: low efficiency solar photovoltaic cells and energy losses in RO subsystem. For the brackish PV-RO systems, the efficiency ratios are about 10 times lower than the seawater PV-RO systems, this is because the absence of energy recovery devices in such systems.

Table 2.2 Overview of recent state-of-the-art PV-RO systems

Author, year & source	Feed water	Recovery ratio	Ideal solar energy Usage	PV material	PV capacity	Energy recovery devices	Actual solar energy usage	Efficiency ratio*
	(ppm)	%	(kWh/m^3)		(kWp)		(kWh/m^3)	(η_r)
Mohammed et al., 2006, (Mohamed et al. 2005; Mohamed et al. 2008)	30425	0.1	0.82	Mono Si	0.85	Clark pump	54.7	0.015
Herold et al., 2006 (Herold et al. 1998; Herold and Neskakis 2001)	35500	0.15	0.98	Mono Si	4.8	No	75.4	0.013
Mohamed et al., 2003 (Mohamed and Papadakis 2004)	40000	0.23	1.16	Mono Si	31.2	Brine hydraulic	114.2	0.01
Thomson et al., 2003 (Thomson and Infield 2003)	29000	0.1	0.78	Mono Si	1.53	Clark pump	34.7	0.023
Tzen et al., 1998 (Tzen et al. 1998)	40000	0.23	1.16	Multi Si	26.3	Yes	34.2	0.034
Kelley et al., 2013 (Kelley and Dubowsky 2013)	30000	0.09	0.78	-	1	Yes	21.3	0.036
Qiblawey et al., 2007 (Qiblawey et al., 2006)	720	0.37	0.02	Mono Si	0.11	No	110.5	0.0002
Ahmad et al., 2000 (Ahmad and Schmid 2002)	2000	0.5	0.07	Mono Si	1.1	No	55	0.0013
Carvalho et al., 2000	1200	0.27	0.04	-	1.1	No	8.9	0.004

(de Carvalho et al. 2004)								
Munari et al., 2005 (De Munari et al. 2009)	3982	0.18	0.11	Multi Si	0.6	No	90.2	0.0012
Richards et al., 2003 (Richards and Schafer 2003)	3500	0.55	0.13	Mono Si	0.26	No	25.4	0.005
Riffel et al., 2006 (Riffel and Carvalho 2009)	800	0.13	0.02	-	0.17	No	30.9	0.0007
Fraidenraich et al., 2012 (Fraidenraich, Vilela et al. 2012)	5000	0.33	0.15	Mono Si	0.81	No	20.6	0.007
Peterson et al., 2011 (Peterson and Gray 2012)	1900	0.4	0.06	Multi Si	0.3	No	15.3	0.004

Notes: *solar energy available for desalination = solar irradiance × PV panel area; thus, actual solar energy usage= total input solar energy/freshwater production. Efficiency ratio η_r = ideal solar energy usage / actual energy usage.

2.4.1. The physical basis of PV solar cell operation

In PV-RO applications, PV modules and panels are formed by connecting and encapsulating numerous solar cell units. Solar cells are made from solar PV materials which are semiconductors. Generally, PV energy conversion consists of two essential steps as shown in Fig. 9: (i) electron-hole pair generation: because the semiconductor materials have weakly bonded electrons occupying valence band, once photons are absorbed by these electrons, they can jump over the energy gap, and move to conduction band; (ii) electron collection: the generated electrons and holes are separated and collected by the structure of solar cell and electricity is thus conducted through the solar cell.

Most commercial solar cells are made of mono- or multi-crystalline silicon; these accounted for 90% of the world market in 2000 (Luque and Hegedus 2011). Other materials employed include amorphous silicon, cadmium telluride and even polymers. Solar cell developments have already been through three generations. The first generation was based on silicon wafers, which still dominate the solar cell market thanks to their high efficiency. In early 1980s, thin-film solar cells started to show promise and these became known as the second generation. Thin-fi lm solar cells are super light and flexible, although they do not have advantages regarding efficiency compared to silicon solar cells, they do save a lot of materials, therefore cutting costs. And now researchers are trying to invent and develop novel designed solar cells of the so-called ‘third generation’ that have both higher efficiency and lower cost (Green 2006). This generation represents the cutting edge of solar technology and with operating principles quite different from the traditional semiconductor p-n junction. The third generation includes emerging solar cells such as polymer solar cells, dye-sensitized solar cells, etc., and the research on them is still at a very early stage.

2.4.2. Energy losses in PV subsystem

An overview about the losses in solar cells and potential methods to improve their efficiency has been reported in our previous paper (Qiu and Davies 2010), only efficiencies of different types of solar cells are presented in this section.

Several studies (Trivich and Flinn 1953; Shockley and Queisser 1961; Mathers 1977; Ruppel and Wurfel 1980) about the efficiency limit of tandem solar cell structures reveal that, for an infinite number of stacked solar cells in concentrated sunlight, the maximum efficiency is 86.8%. Comparing this theoretical number to the practical laboratory observed efficiencies of various solar cells shown in *Figure 2.7*, which collates the best solar cells efficiencies achieved in recent decades for all the major PV technologies, it is obvious that various losses happen during the conversion process of solar cells (*Figure 2.8*).

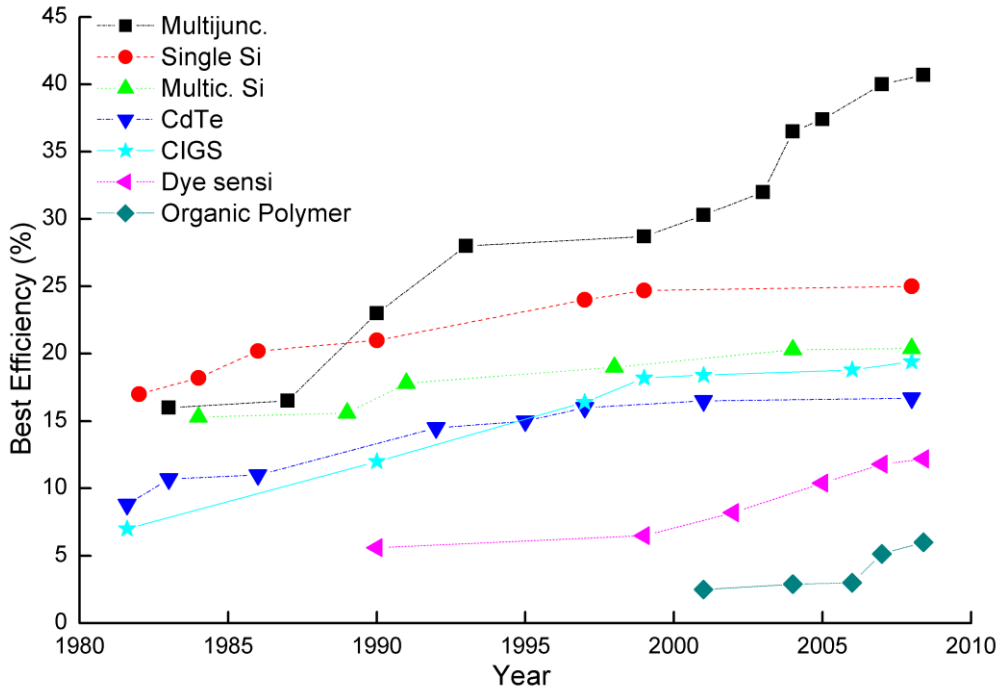

Figure 2.7 The trends in best efficiency achieved over the past decades, compiled by the author based on Solar Cell Efficiency Tables (multi versions, to Version 40), (Green 1993 to Green 2009).

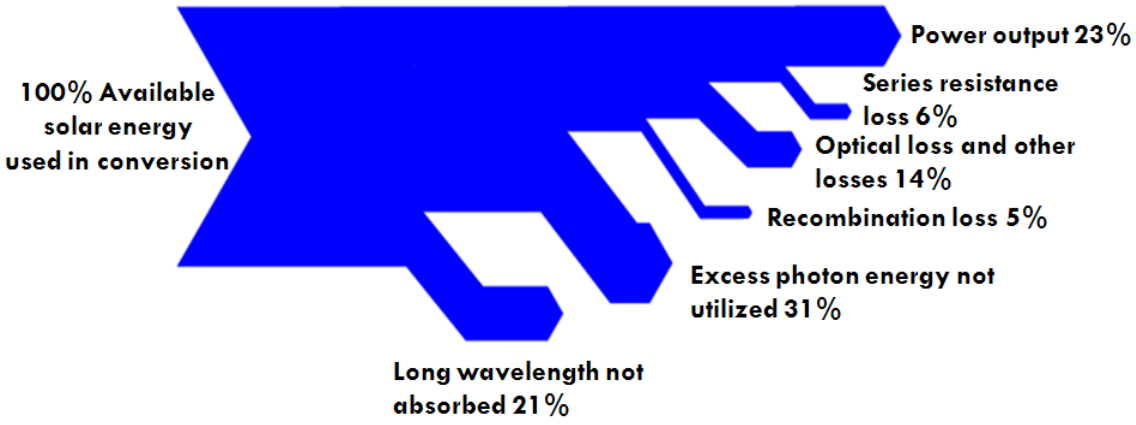

Figure 2.8 Various energy losses in a silicon solar cell

2.5. Solar Rankine cycle RO system

The solar thermal RO technology involves application of the solar Rankine cycle (RC) to generate electricity from mechanical power. This technology has recently received a lot of attention as a potential alternate to PV-RO. Despite extensive design studies on RC-RO, to date, few experimental studies have demonstrated a higher efficiency for desalination compared to PV-RO systems.

2.5.1. The Rankine cycle

In a Rankine cycle (RC), thermal energy is converted into mechanical energy. For a typical RC, the working fluid is water which is evaporated in a boiler. Then the generated vapour is adiabatically expanded through a steam turbine to generate mechanical work. The remaining vapour is cooled and condensed into liquid and pumped back to the boiler and the cycle starts again. The working fluid flows in a closed circuit and its volume and pressure change during the RC operation (*Figure 2.9*).

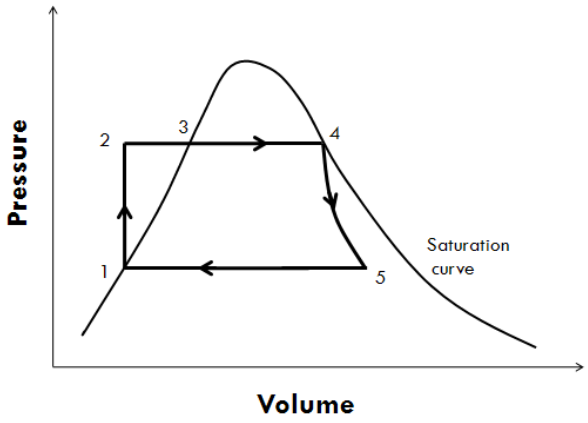

Figure 2.9 The volume and pressure changes of working fluid during RC operation. Line 1-2 represents the compression of the working fluid by the feed pump to the boiler. Line 2-4 indicates the vaporization of the working fluid at constant pressure (non-superheat). Line 4-5 refers to the steam expansion in the turbine, and then line 5-1 represents the condensation of the vapour-liquid mixture at constant pressure.

2.5.2. The RC-RO desalination

The RC has been applied for various purposes for decades, such as electricity generation which is the conventional application of RC, others like vapour compression chillers, water pumping for irrigation or water distribution and so on (Aghamohammadi et al. 2001). Besides solar-thermal energy, the RC can also be powered by biomass combustion and geothermal plants (Schuster et al. 2009). The emerging applications of the RC include waste heat recovery from biogas digestion plants and micro combined heat and power generation and, of course, RO desalination. Nevertheless, except for small water pumping systems, none of the above applications have been thoroughly analysed or developed and very few implementations exist (García-Rodríguez and Blanco-Gálvez 2007). The application of the RC in RO desalination is still at an early stage; therefore, the knowledge and experience on solar RC-RO desalination is very limited. Among the few published studies on the design of solar RC-RO systems, as shown in *Table 2.3*, only three such systems had been implemented by the time this work was conducted.

Table 2.3 Overview of solar RC-RO systems

Authors, date and source	Feed Water type	System configuration	Solar collector type	Working fluid	Freshwater production ($l \cdot m^{-2}$ per day)	RC thermal efficiency (%)
Libert et al., 1981 (Libert and Maurel 1981)	BW	-	FPC	Freon	130	2.2
Manolakos et al., 2005[d] (Manolakos et al. 2005)	SW	HTF	ETC	HFC-134a	240	7
Delgado-Torres et al., 2007[d] (Delgado-Torres and García-Rodríguez 2007; Delgado-Torres and García-Rodríguez 2007)	-	DVG	PTC	Toluene	-	21
				D4	-	19
				MM	-	18
		HTF		Toluene	-	14-20.6
				D4	-	12-18.3
				MM	-	10-17
Delgado-Torres et al., 2007[d] (Delgado-Torres et al. 2007)	SW	DVG	PTC	Toluene	1800-2640	23-32
				D4	1200-2160	16-27
				MM	1200-2160	15-26
		HTF		Toluene	1540-2400	23-30
				D4	1080-1848	15-27
				MM	1130-1780	15-25
Burno et al., 2008[d] (Bruno et al. 2008)	SW	HTF	FPC	Octafluoropropan	21-30	8
			ETC	R-245	42-53	13.3
			PTC	Isopentane/N-prpylbenzene	75-260	28/32

	BW		FPC	Octafluoropropan	60-100	8
			ETC	R-245	140-170	13.3
			PTC	Isopentane/N-prpylbenzene	170-830	28/32
Manolakos et al., 2009 (Manolakos et al. 2009)	SW	HTF	ETC	HFC-134a	80-140	0.73-1.17
Delgado-Torres et al., 2010[d] (Delgado-Torres and García-Rodríguez 2010)	SW	-	CPC	R245fa	504-744	9-12
			FPC		552-960	9-13
			ETC		984-1224	13.5-16
	BW	-	CPC		1782-2600	9-12
			FPC		1920-3310	9-13
			ETC		3408-4752	13.5-16
Nafey and Sharaf, 2010[d] (Nafey and Sharaf 2010)	SW	DVG	FPC	Butane	166	8-8.1
				Water	188-192	9-10
			PTC	Toluene	520	25.8-26
				Water	590-600	30-30.5
			CPC	Hexane	200-230	14-14.5
				Water	220-280	13-18
Li et al., 2012[d] (Li, Kosmadakis et al. 2013)	SW	HTF		MM	112	21

Note: HTF= heat transfer fluid configuration; DVG= direct vapour generation configuration; CPC= compound parabolic collector; FPC=flat plate collector; ETC=evacuated tube collector; PTC=parabolic trough collector; VTC=vacuum tube solar collector; HFC-134a=1,1,1,2-Tetrafluoroethane; R245fa=1,1,1,3,3-Pentafluoropropane; D4=Octamethylcyclotetrasiloxane; MM= Hexamethyldisiloxane; [d]=design study

2.5.3. Working fluids

One of the most attractive topics as regards improving the RC performance is the use of alternative working fluids. Basically, the RC's efficiency is determined by the difference between evaporation and condensation temperatures, which are highly related to the thermal properties of the working fluids. Additionally, environmental issues about various working fluids should be considered carefully. That is why researchers have been searching and selecting the most appropriate working fluids for decades (Badr et al. 1985; Angelino and Colonna di Paliano 1998; Saleh et al. 2007; Tchanche et al. 2009).

Water is the conventional working fluid used for RCs. Other types of inorganic fluids (e.g. ammonia) can be used as well. However water has some drawbacks, such as low molecular weight, and the moisture content of steam may be too high, leading to the erosion of the turbine blades. To overcome the shortcomings of the steam-based RC, organic working fluids can be utilised such as freon, or butane, propane and other new environmentally friendly refrigerants. Their higher molecular weights lead to slower rotations of the turbines, while lowering the pressure and erosion of the metallic parts and blades. It has been found that for low-temperature levels of heat source, the system will be more efficient with the use of organic working fluids instead of water (Yamamoto et al. 2001; Liu et al. 2004). Moreover, because of the different critical temperatures and pressures of various organic compounds, the organic RC can be utilized for different heat sources of low energy and temperature levels, for instance solar thermal, geothermal (Madhawa Hettiarachchi et al. 2007), biomass or waste heat from various industries (Maizza and Maizza 2001). The conclusions concerning the best working fluids for RC-RO systems are controversial. Delgado-Torres and Garcia-Rodriguez (Delgado-Torres and García-Rodríguez 2010) presented a working fluid selection study for low-temperature RC coupled with a RO desalination system. After considering the thermodynamic efficiencies of 12 working fluids with their environmental characteristics and unit aperture area factors, four fluids were selected: isopentane, isobutene, R245ca and R245fa. For a heat transfer fluid (HTF) configuration RC, isopentane is the best fluid which gave the highest RC thermal efficiency of

10−16.6% and the lowest unit aperture area no matter what type of solar collector was used. Delgado-Torres and Garcia-Rodriguez (Delgado-Torres and García-Rodríguez 2010) also pointed out that the size of RC-RO compounds, such as the vapour turbine and the condenser, are affected by the choice of working fluid. They found out that for the same power output of the RC, the smallest devices were with isobutene as the working fluid whereas isopentane would yield the biggest devices. Kosmadakis and Manolakos (2009) also presented a working fluid selection study for the top cycle of a high temperature two-stage RC -RO system. The study considered 33 organic working fluids. After a selection which was not only based on their thermodynamic performances but also various other criteria, the most appropriate working fluid found was R245fa.

There is no certain answer as to which working fluid is the most suitable for a RC-RO system, since the working fluid cannot be optimised in isolation from the rest of the system. For instance, the solar collector efficiency will be decreased by increasing the evaporation temperature of the working fluid. If the expansion system is a conventional turbine, dry fluids and superheating the fluid are preferred. Besides those factors mentioned above, the application, size of the system, operation time and conditions should also be considered.

2.5.4. Solar thermal collector

Currently, there are several solar collectors available on the market (Figure 2.10) including: the compound parabolic collector (CPC), the flat plate collector (FPC), the parabolic trough collector (PTC) and the evacuated tube collector (ETC) (see *Table 2.4*).

Table 2.4 Solar thermal collectors, from (Soteris A 2005)

Motion	Collector type	Absorber type	Concentra-tion ratio	Indicative temperature range (°C)
Stationary	Flat plate collector (FPC)	Flat	1	30-80
	Evacuated tube collector (ETC)	Flat	1	50-200
	Compound parabolic collector (CPC)	Tubular	1-5	60-240
Single-axis tracking	High-temperature parabolic trough collector (CPC)	Tubular	15-45	60-300
	Linear Fresnel reflector (LFR)	Tubular	10-40	60-250
	Cylindrical trough collector (CTC)	Tubular	10-50	60-300
Two-axes tracking	Parabolic dish reflector (PDR)	Point	100-1000	100-500
	Heliostat field collector (HFC)	Point	100-1500	150-2000

Note: Concentration ratio is defined as the aperture area divided by the receiver/absorber area of the collector

Figure 2.10 Various solar collectors: (a) Flat plate solar collector; (b) Evacuated tube collector (c) Parabolic trough collector; (d) Solar thermal collector dish (Wiki 2014)

For solar RC-RO systems, researches have been carried out to compare the performances of these solar collectors in the Rankine system as shown in *Table 2.3* (Delgado-Torres and García-Rodríguez et al. 2007; Delgado-Torres and García-Rodríguez 2010; Nafey and Sharaf 2010). In Delgado-Torres's study, the ETC coupled with R245fa as working fluid showed the best RC thermal efficiency of 16%. In another study, Nafey (2010) reported in a design study that by using the parabolic trough collector with either toluene or water, the system could yield more than 25% efficiency.

2.6. Summary

PV-RO technology is mature for commercial implementation, and it is better suited to large scale seawater desalination applications with regard to system overall efficiency. Despite the great improvement in PV solar cells, the high investment costs for PV modules and short lifetime still hinder their application, especially for small scale BW desalination.

Another novel desalination combination —solar RC-RO technology— is also on the horizon. Although the experience of the RC-RO desalination is limited, such systems exhibit great flexibility, automatic and continuous operation, low maintenance requirements, long lifetime and the ability to recover low to medium grades of input heat. The results shown in *Table 2.3* may be not attractive at first sight, but they are comparable with PV-RO systems which have usually given around 15% efficiency of solar-electricity conversion (García-Rodríguez and Delgado-Torres 2007). These authors pointed out that the specific energy consumption of the RO process driven by the RC is lower than PV-RO systems and solar distillation as well. Thus, solar RC-RO systems hold promising features for desalination for rural communities without access to electricity. However, a principal drawback in using the steam RC at small scales is that the steam turbines typically used tend to become unattractive at the low power outputs due to the blade friction losses and leakage losses. Instead of using turbines that convert the steam enthalpy into rotary motion, a possibly more advantageous alternative is to use a piston to expand the steam. A steam pump may be used in a way that the piston is directly coupled to the piston of a reciprocating pump. However, a deficiency with steam pumps is that the force provided by the power piston

varies as the piston moves over its cycle. Thus, solutions that overcome the adverse effects of varying forces should be proposed and examined.

There are several key areas that need to be studied to improve RO systems' energy efficiency including (i) optimised designs for RO system configuration, (ii) effective pretreatment systems, (iii) improvements in membrane elements, and (iv) improved ERDs. Given the difficult-to-eliminate limitations of thin film membranes, along with rarely applicable ERDs for BWRO desalination systems, the advanced system design becomes the prioritised factor worthy of investigation to improve the energy efficiency. The in-house designed batch mode RO operation will be clearly demonstrated in this thesis to be a novel design that can accomplish the desired goals for an ideal desalination system. Some of the most advantageous and promising features of the batch-RO include reduced energy conversion steps, rearranged better-performing RO system configuration, and recycling of high pressure brine without an ERD. *Chapter 3* will describe the batch-RO system in greater details.

Chapter 3

THEORY AND DESIGN OF BATCH MODE RO SYSTEM

The critical design considerations and criteria for the BWRO plant are discussed. Several popular candidate RO configurations, such as single and multi-stage RO with/without ERD, are carefully investigated through theoretical analysis of their SEC. An innovative batch-RO system is extensively compared with other conventional designs based on continuous flow. Advantages of the proposed batch-RO are further elucidated with an emphasis on real-world applications.

3.1. Introduction

Most of the current RO plants are still prone to energy intensity when it comes to the desalination of BW on small-scale, due to relatively smaller components e.g. pumps, and absence of ERDs (Qiu and Davies 2011). Therefore, improving the energy efficiency of BW desalination, increasing water output per land area, minimising the discharged brine, and eventually reducing cost are some of the desirable outcomes when designing the BWRO system. Optimum designs of BWRO systems provide an effective approach to achieve these goals (Davies 2011; Efraty and Gal 2012).

Usually, BWRO desalination plants implement a basic configuration of one stage (*Figure 3.1*), and the membrane module may contains one or several RO elements in series. The RO module arrangement with an additional membrane module (*Figure 3.2*) must be operated at a pressure well above the osmotic pressure of the feed water, to overcome the osmotic pressure reached at the exit of the second module.

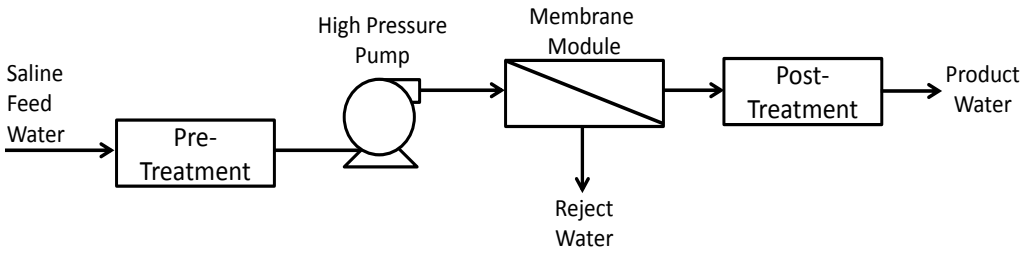

Figure 3.1 Conventional one stage brackish water reverse osmosis (BWRO) system

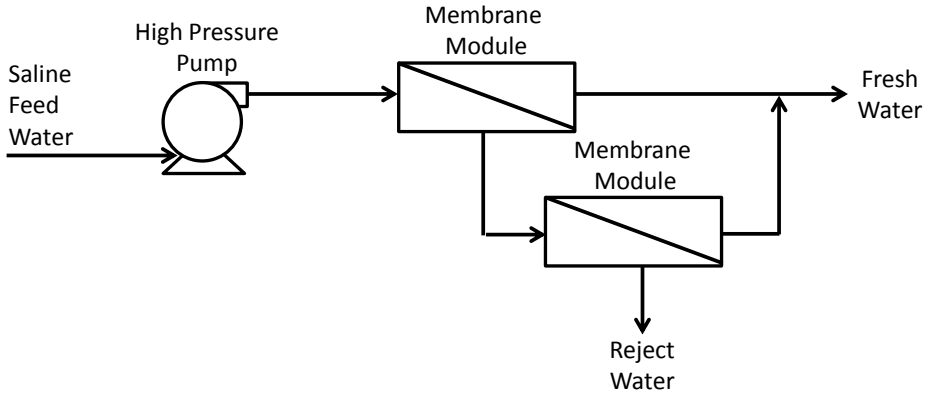

Figure 3.2 BWRO system with additional membrane module connected to the reject water

3.2. Designs of BWRO System

A BWRO desalination system can be modified in several ways to improve its performance. One approach is to develop and implement the optimized system configurations. For example, a BWRO system may be operated in a batch mode (i.e. operating RO in a non-continous mode, increase the operation pressure with the increasing feed solution concentration without introducing more feed water) and without an ERD. To date, most of the small-scale RO systems were built without an ERD. This may keep capital costs down but at the expense of a heavy penalty in energy costs.

3.2.1 Multi-stage Configuration

For an RO system, a serial arrangement of the RO membrane elements is more energy efficient than a parallel one as shown in *Figure 3.3* (Laborde et al. 2001). For serial arrangements, however, a substantial longitudinal gradient in concentration will occur. In the

desalination process, freshwater is progressively removed along the RO membrane module, the salt concentration along the channel increases to a value almost twice (for seawater) or three times (for BW) that at the inlet. To maintain a flux of water over the entire feed channel, the operation pressure is determined by the concentration at the outlet rather than the inlet, as illustrated in *Figure 3.4 (a)*. Thus, part of the feed energy is lost due to the longitudinal concentration gradient (see *Section 2.5.2*).

Figure 3.3 Energy consumption for different RO module arrangements (Laborde et al. 2001).

One example of system design that can eliminate this loss is a multi-stage configuration. This design adopts several stages in series along with several booster pumps. The first stage operates at a lower pressure, because of the lower salinity of the feed water. The concentrate from the first stage is then fed into a second stage, where the salinity becomes higher. The inter-stage booster pump provides higher pressure correspondingly, thus removing the necessity to have the first-stage pump providing extra pressure. Consequently, the energy loss associated with the increased longitudinal concentration can be minimized. *Figure 3.4 (b)* gives a direct illustration of the energy savings achieved by the 3-stage RO system with the three pumps providing pressure P_1, P_2 and P_3 (as shown in *Figure 3.6)*.

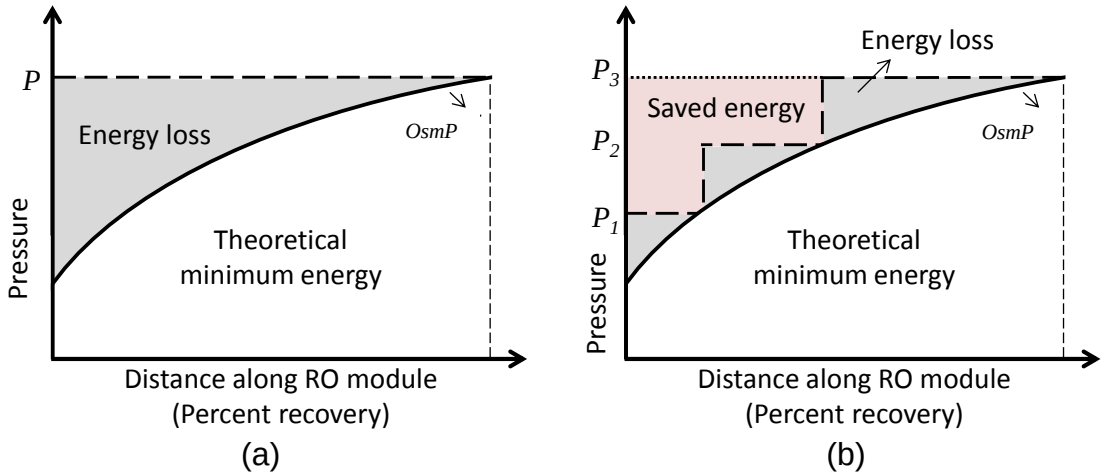

Figure 3.4 Energy usage of RO systems and the effect of longitudinal concentration gradient. The theoretical minimum energy demand for desalination, which is represented by the area under the osmotic pressure curve, is equal to the energy needed to bring saline water to the maximum osmotic pressure in the corresponding module. (a) for a single-stage system, the operation pressure P must be at least equal to the osmotic pressure π of the solution at the outlet of the membrane module. The applied energy is represented by the area under the dash line. The difference between these two areas (grey area) is the provided extra energy, i.e., energy loss, (b) for a 3-stage system, by providing appropriate pressure for each stage, the energy loss (grey area) is reduced, and some of the extra energy is saved (pink area). Based on (Elimelech and Phillip 2011).

The configurations of multi-stage BWRO systems with or without an ERD are depicted in *Figures 3.5* and *3.6*. A Design study by Vince 2008 has shown that multi-stage systems, with modules connected to reject water with booster pumps, are able in principle to minimize the electricity consumption. Lu 2007 also recommended that for low feed concentration (around 3000 mg/L), the optimal design is a 3-stage system with ERD that can increase recovery ratio. When high operating pressures are necessary, the simple, one-stage configuration is favoured (Alghoul et al. 2009).

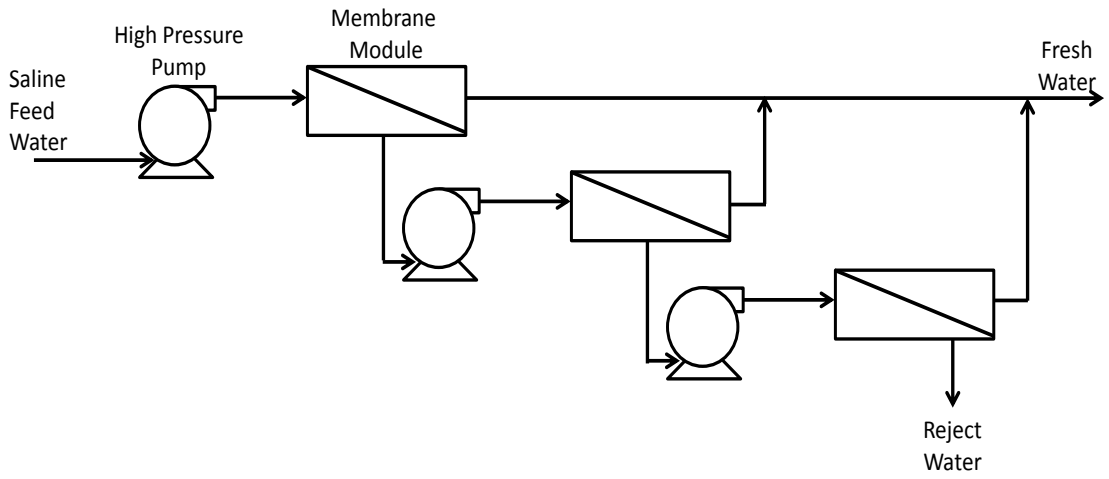

Figure 3.5 3-stage system with intermediate pumps

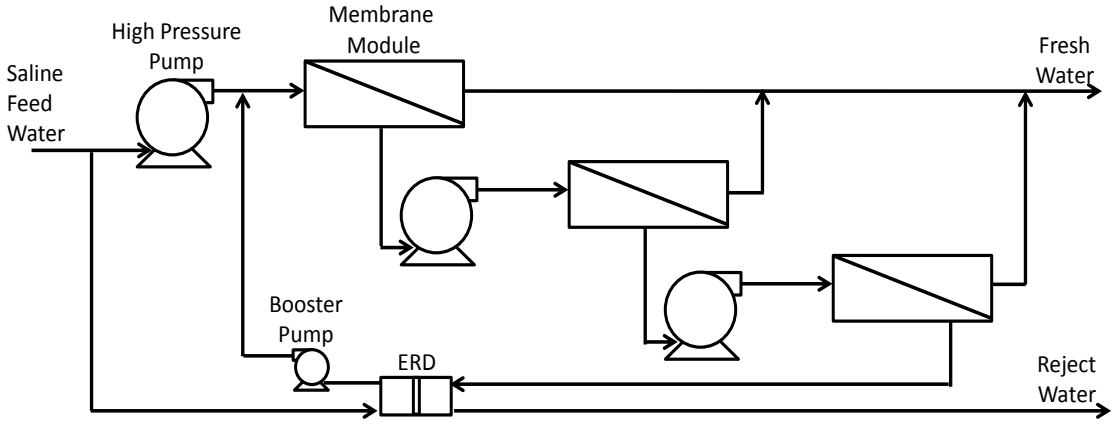

Figure 3.6 Multi-stage system with work exchanger type ERD

3.3. Innovative designs

Multi-staging attempts to overcome the problem of longitudinal concentration gradient by spatial separation of the system into modules working at different pressures. A contrasting approach is temporal separation, whereby a single module is operated at time-varying pressure as the concentration and osmotic pressure gradually increase. An advantage of the time-varying (i.e., non-steady) approach is that it is possible in principle to attain the theoretical minimum energy of desalination; whereas with multi-staging, this would only be possible if an infinite number of stages were employed.

3.3.1. Batch Mode RO Operation

For RO, batch operations are used in laboratory filtration cells for experimental purposes, but they have rarely been employed at process scale with a view to optimizing energy efficiency (Davies 2011). The design philosophy of the batch mode operation is illustrated in *Figure 3.7*. Saline water is contained in a water cylinder. The cylinder piston driven by the input work pressurizes the saline water against the RO membrane and the permeate is expelled. To diminish the undesirable concentration polarization effects at the membrane surface, a stirring mechanism is needed.

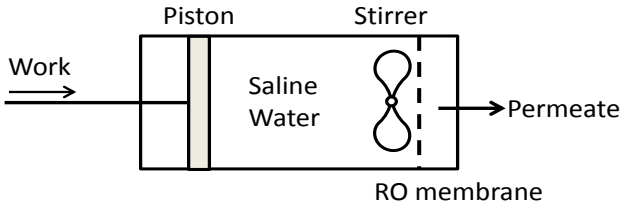

Figure 3.7 The essence of the batch mode RO process

A practical realization is shown in *Figure 3.8*, in which stirring is achieved by recirculation through an external RO module. During the pressurization stage, the pressurized concentrate is fed back into the pump cylinder with the help of the re-circulation pump. Therefore, this cyclic mode operation process obviates the need for costly ERDs by re-circulating the pressurized concentrate back to the water cylinder directly.

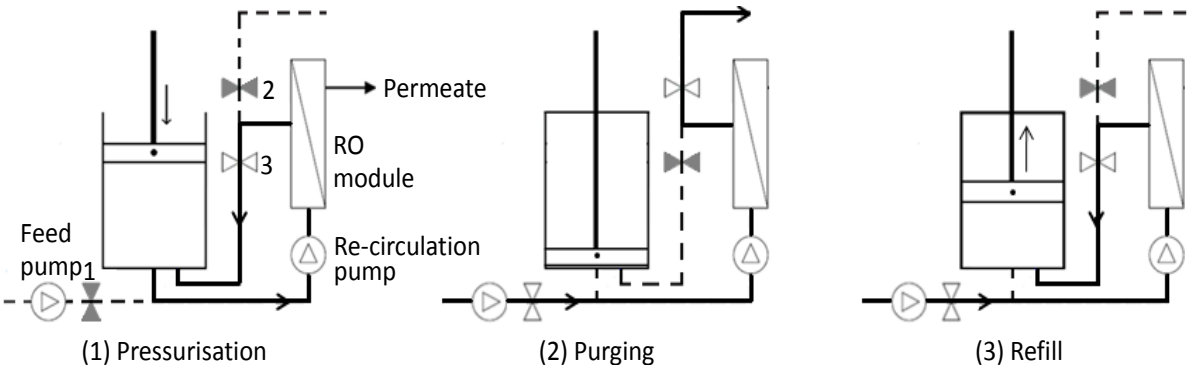

Figure 3.8 Schematic of practical operation process of batch-RO system: initially both the pump cylinder and RO module are filled with saline water, (1) pressurisation stage (with valve 3 open, valves 1 and 2 closed) the piston pressurises the water, causing freshwater to pass through the membrane. The concentration of solution increases gradually. The concentrations at the inlet and the outlet of the module are kept nearly equal with the help of the re-circulation pump. After the pump piston reaches the end of the cylinder, only concentrated brine is left in the module. Thus, it is necessary to purge the module by introducing feed water (with valves 1 and 2 open, valve 3 closed). In the purging stage, the concentration at the outlet decreases towards the value at the inlet. After washing out the left concentrate, the feed pump feeds saline water into the cylinder to move the piston upwards (with valves 1 and 3 open while valve 2 is closed); thus, the whole system is refilled and restored to its ready-to-go state. The water flow paths and no-flow paths of all the pipes are shown by bold and dashed lines respectively.

3.3.2. Closed Circuit mode RO operation

Another BWRO desalination system that uses time-varying conditions, called Closed Circuit Desalination (CCD), has been proposed and developed by Efraty (2012). The concept of CCD is illustrated schematically in *Figure 3.9*. Pressurized feed is supplied by a high pressure pump. A stirring device is imagined inside the water vessel to prevent the concentration polarization effect. This system operated under variable pressure conditions according to the level of concentrate salinity. When it reaches the desired recovery fraction, the process stops, the container is decompressed and brine is replaced by fresh feed. Then

a new cycle of operation is initiated. A practical CCD apparatus is illustrated in *Figure 3.10*. The design includes a feed pump to provide high pressure, a circulation pump to recycle concentrate back into the RO module and valves to enable brine replacement with fresh feed when the desalination reaches a desired recovery level. In order to operate the CCD-RO continuously, a new method has been developed using multiple modules and switching among them (Efraty, Barak et al. 2012). The principle of the new apparatus is the same as the one shown in *Figure 3.10*, to which a side water vessel is added that can be either engaged with or disengaged from the CCD process by means of several actuated valves. Detailed information about continuous CCD can be found elsewhere (Efraty, Barak et al. 2012).

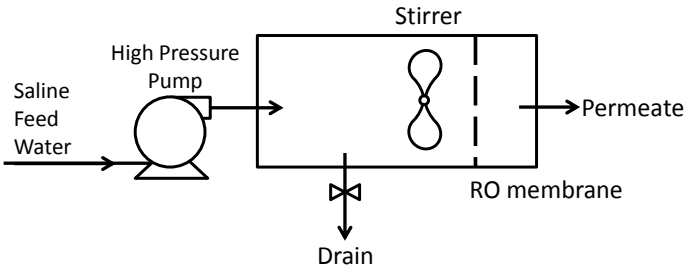

Figure 3.9 The concept of closed circuit RO operation

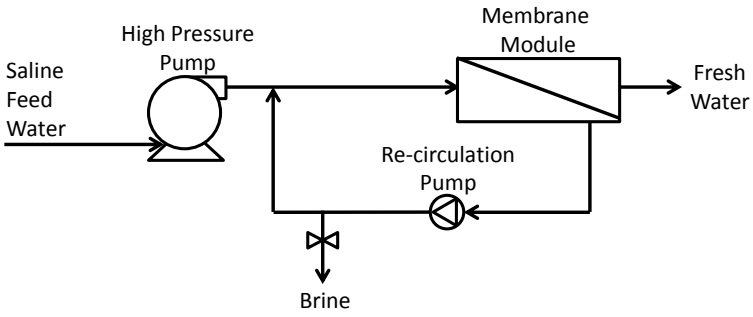

Figure 3.10 A schematic design of an apparatus for CCD-RO desalination

3.4. Comparison of Different Configurations

Both single and multi-stage BWRO systems have a continuous hydrodynamic process performed with a fixed pressure and a pressurized feed flow at every stage. For the batch-RO and CCD-RO systems, the desalination process is performed under variable pressure conditions, because of the increasing concentration of bulk solution. *Table 3.1* summarizes expressions for determining SEC for the different RO system configurations, with the variables defined as follows: $OsmP$ is the osmotic pressure of feed solution, r is the recovery ratio, and s is the number of stages. All the expressions in *Table 3.1* are based on the following assumptions: (1) negligible salinity and osmotic pressure of the permeate, (2) negligible pressure loss in rejected concentrate, (3) linear relationship between osmotic pressure and salt concentration, and (4) 100% efficiency of booster pump and ERD. Furthermore, the effects of CP and fouling are not considered.

Table 3.1 Specific energy consumption (SEC) of different BWRO system configurations

RO system configuration	Without energy recovery	With energy recovery
Single-stage	$OsmP \cdot \frac{1}{\mathrm{r}(1-\mathrm{r})}$	$OsmP \cdot \frac{1}{(1-\mathrm{r})}$
Two-stage	$\frac{OsmP}{\mathrm{r}}\left[\frac{2}{\sqrt[2]{1-\mathrm{r}}}-(2-1)\right]$	$\frac{OsmP}{\mathrm{r}}\left(\frac{2}{\sqrt[2]{1-\mathrm{r}}}-2\right)$
n-stages	$\frac{OsmP}{\mathrm{r}}\left[\frac{\mathrm{n}_s}{\sqrt[\mathrm{n}_s]{1-\mathrm{r}}}-(\mathrm{n}_s-1)\right]$	$\frac{OsmP}{\mathrm{r}}\left(\frac{\mathrm{n}_s}{\sqrt[\mathrm{n}_s]{1-\mathrm{r}}}-\mathrm{n}_s\right)$
Batch-RO	$\frac{OsmP}{\mathrm{r}}\ln\frac{1}{(1-\mathrm{r})}$	
CCD-RO	$OsmP\left[1+\frac{r}{2(1-r)}\right]$	

Figures 3.11 and *3.12* are offered to compare the performance of RO systems with different system configurations, where the normalized SEC is defined as $SEC/\ OsmP$. For multi staged RO systems without an ERD (*Figure 3.11*), the theoretical limit of normalized SEC is 4, 3.6 and 3.4 for the number of stages being 1, 2, and 3, respectively. The optimum

recovery ratio is around 50%–60%. Using more stages, up to 3, not only reduces the normalized SEC, but also improves the fractional recovery of water. However, the normalized SEC shows only minor improvement when the number of stages is more than 3. Clearly, multi-stage RO without an ERD is not very efficient in terms of energy consumption. Conversely, as shown in *Figure 3.12*, the multi-stage RO systems with an ERD have significantly reduced the normalized SEC, with a theoretical limit of 1 (i.e. the specific energy consumption in Table 3.1 is approaching the ideal SEC which represented in Eq. 2.2), as the corresponding recovery ratio approaches zero. It becomes larger when the desired fractional recovery increases. On the basis of the above analysis, it can be concluded that the normalized SEC can be reduced either by increasing the number of stages or using an ERD. It should also be noted that both methods inevitably increase the cost.

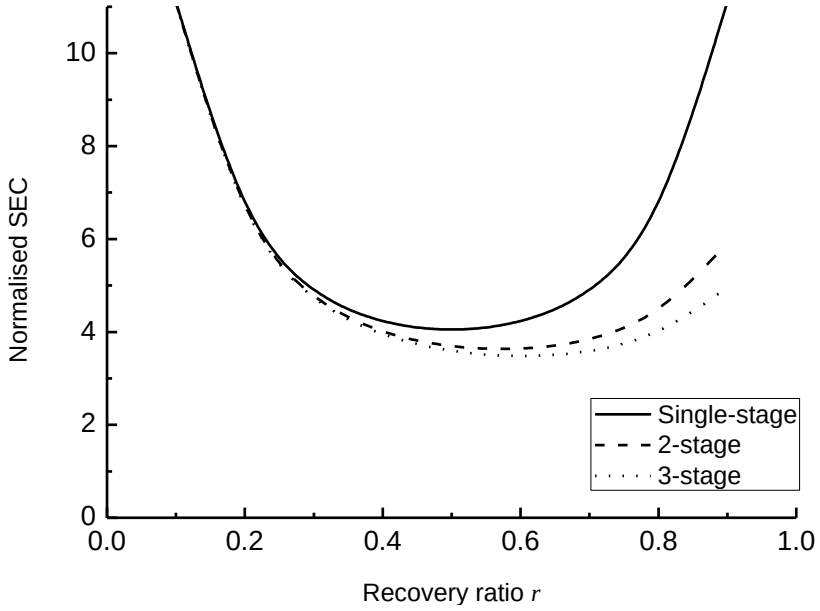

Figure 3.11 Theoretical limit of normalized SEC in staged ROs without ERD

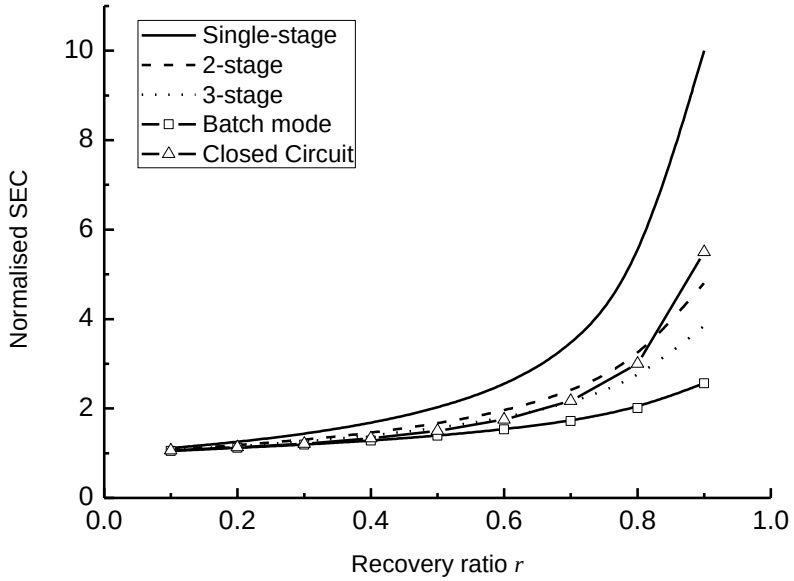

Figure 3.12 Theoretical limit of normalized SEC in batch-mode RO and multi-stage ROs with ERD

The energy consumption of batch-RO and CCD-RO is very competitive with multi-stage systems with ERDs (*Figure 3.12*). The CCD-RO system has a very similar normalised SEC to the 3-stage one, although this advantage becomes less obvious when the required recovery ratio is 80% or above. For practical facilities, it is not recommended to maintain very high recoveries based on the considerations of concentration polarization prevention and membrane fouling prevention. In particular, the batch-RO has the lowest normalized SEC due to the fixed feed water volume. The SEC of the batch-RO can be reduced by 30% compared to a 3-stage system at a recovery ratio of 80%. Thus, batch-RO holds promise for providing high recovery along with low energy demand and cost when compared to conventional systems. However, for batch-RO, a question remains about the membrane stability during the repeated pressurization and de-pressurization of feed solution. Nevertheless, the operation parameters of the batch-RO system do not exceed the membrane specification provided by the manufacturer. The loading with recycled brine and the unloading with fresh feed water may reduce the development of membrane fouling and scaling so it may even be advantageous, according to Efraty (2012).

3.5. DesaLink

Davies (2011) has presented a system —DesaLink—in which batch-RO can be powered by the work generated from steam expansions, which is interesting for incorporation into thermal and solar thermal plant, allowing for a range of end purposes (i.e., co-generation). DesaLink comprises two subsystems, namely a power system and a batch-RO system. The pistons of these two subsystems are coupled by a crank mechanism to provide mechanical advantage during the desalination process. DesaLink works on the principle that the mechanical energy provided by the steam expansion is directly applied to the feed water without any further conversion steps; thus losses will be minimized. The aim is to produce high freshwater output but also reduce brine discharge with low energy consumption (Qiu et al. 2012).

In the DesaLink arrangement (*Figure 3.13*), the power piston drives the pump piston via a crank mechanism in which the crank OP rotates about the fixed point O. The initial and final positions of the system are shown in bold and dashed lines respectively. By using a simple arrangement consisting of a crank (OP) and linkages (LP and MP) to couple the two pistons, an increasing mechanical advantage will be obtained as the pistons move. Hence, the force available from the power piston decreases while the force available to pressurise the pump piston increases.

In the preliminary concept study of Davies (2011), the crank mechanism was analysed in detail and its mechanical efficiency was assessed to be in the range of 55% to 94% depending on operation condition. In order to recover more groundwater without compromising the efficiency, 70% recovery ratio was chosen, thus the volume of the pump cylinder was determined. Based on a work balance between the energy generated by steam expansion and the needed separation energy, the volume of feed steam and the volume of the power cylinder were also obtained. The system parameters and RO module details are provided below (*Table 3.2*).

Figure 3.13 Schematic of DesaLink configuration, from Davies (2011)

Table 3.2 Calculated system parameters (Davies, 2011)

RO module volume	(m^3)	0.001
Membrane Permeability	(m/s·Pa)	1.00E-11
Membrane salt transfer coefficient	m/s	1.80E-07
Membrane area	(m^2)	2.6
Feed channel height	(m)	7.1E-4

By applying simple trigonometry and a work balance, the displacements of the two pistons and the motion of the crank point P can be calculated along the whole operation process. The comparison to the ideal movement relationship between the two pistons is illustrated in *Figure 3.14*. In additional, based on the polytropic expression which describes steam expansion and the van't Hoff equation, the variation of the pressures in the two cylinders is shown in *Figure 3.15*, together with the predicted mechanical advantage, which calculated by force available on pump piston/direct forces at power piston.

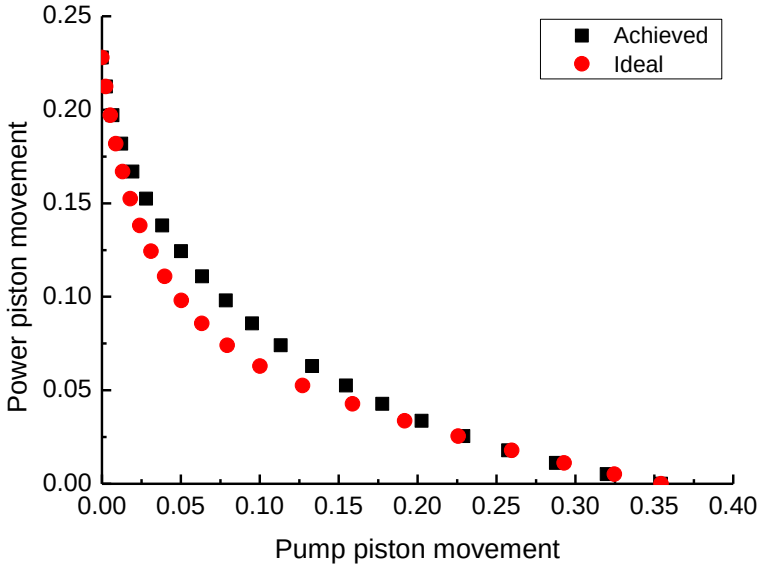

Figure 3.14 Actual vs. ideal motion based on work balance (dimensionless variables used)

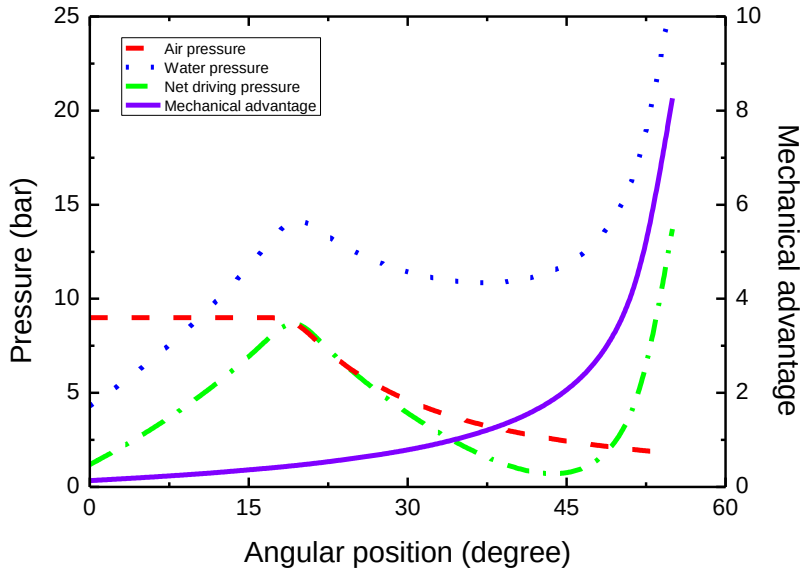

Figure 3.15 The crank mechanical advantage enables a remarkable net driving pressure

3.6. Summary

With the increasing concerns of environmental issues related to brine management in inland areas, a BWRO plant with high recovery ratio is mostly preferred. However, high production always comes hand in hand with high energy consumption. To reduce the energy demand, various designs for BWRO system have been proposed including: (1) use of additional membrane elements to recycle brine; (2) increasing the number of stages with ERD; and (3) operating the RO system in batch mode. While the multi-stage RO system with ERD can largely reduce the energy demand, the overall performance becomes less advantageous given the additional capital costs associated with the membrane elements and booster pumps.

The innovative design of batch-RO systems is considered very promising for further investigation. The reason is twofold. First, the theoretical normalized SEC of batch-RO is less than for a single stage conventional system, and comparable to that of a 3-stage RO system with an ERD. For example, with a TDS concentration of 4000 ppm and a target recovery of 80%, a typical single-stage BWRO system without an ERD requires a theoretical energy input of 0.54 kWh to produce one cube meter freshwater. However, to desalinate the

same amount of water, only 0.17 kWh/m^3 is needed for a batch-RO system. A batch-RO system, therefore, is more technologically attractive thanks to its remarkable improvement over the more conventional counterparts as regards energy consumption. Second, together with its simple components and absence of costly ERD, the batch-RO system has also shown great economic advantages over the conventional systems especially for implementation of small–medium scales.

Chapter 4

EXPERIMENTAL METHOD AND PRELIMINARY RESULTS FOR PILOT DESALINK SYSTEM

A pilot experiment was conducted to examine the batch-RO operation prior to the construction of the DesaLink. This included selection and development of the components, instrumentations, data-acquisition and control systems. Then, a prototype of the DesaLink system was designed and built, in which compressed air was used to simulate the expanding vapour. In this chapter, the characteristics and implementation issues of the system are described. Preliminary experimental results obtained using the prototype are presented and analysed in the light of the expected system behaviour yielded by the performance predictions discussed previously in Chapter 3. Experimental data collected here were also used in the dispersion, concentration polarization studies and the modelling work, which will be discussed in later chapters.

4.1. Batch-RO preliminary experiment

The batch-RO tests were intended to investigate the feasibility of the mechanically driven BWRO desalination system by evaluating the freshwater production against the mechanically provided pressures. Other design factors, including the sealing piston arrangement, sealing of pump piston, re-circulation pump and tube connections were also examined and improved through these tests.

The batch-RO system (depicted in *Figure 3.7*) was set up (*Figure 4.1*). The labelled components are: (1) material testing (Instron® 5500R) machine, (2) pump cylinder (piston diameter 1.05×10^{-2} m (105 mm), piston area of 0.0086 m^2, length of 0.35 m), (3) pressure

gauge; (4) re-circulating pump (Wilo, 3 m³/h maximum flow volume) and (5) RO module (Dow FILMTEC™ type BW30-2540). The experiments were conducted with the use of a materials testing (Instron®) machine, which is able to provide the desired, varying pressurising forces in order to maintain a constant displacement rate. Before the start of each test, both the pump cylinder and the RO module were filled with 3500 ppm sodium chloride (NaCl) solution. In addition, by utilizing the re-circulating pump and vibrating the RO module manually, any trapped air in the whole system cycle was eliminated. Then, the Instron machine was set at a constant displacement rate to compress the pump piston against the solution. Flow pressures and permeate rates were recorded throughout the process. Once the pump piston reached its end, the Instron machine stopped. Subsequently, a chart with force vs. piston displacement was generated. Note that the tests were conducted to evaluate only the pressurisation stage of the batch-mode operation, because of the limitation of the laboratory environment.

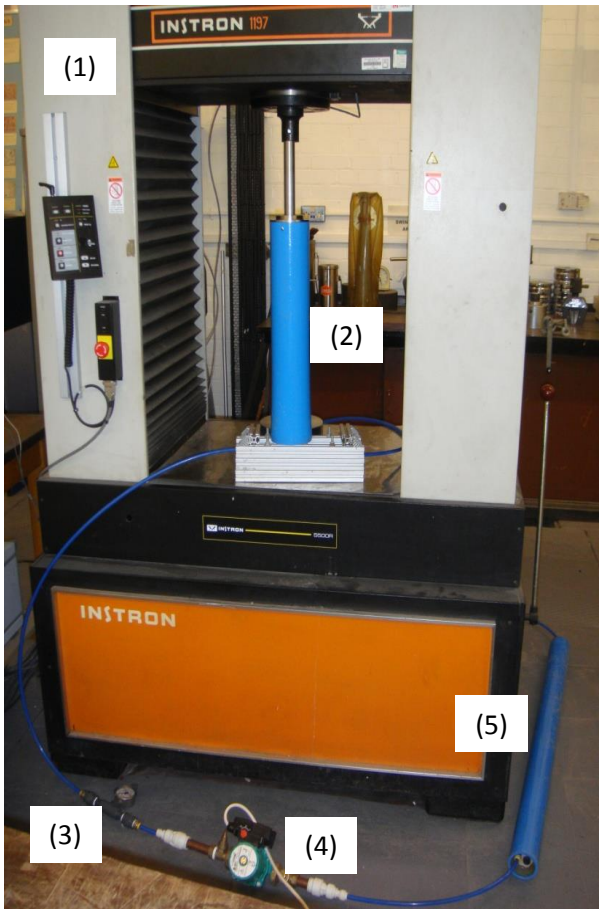

Figure 4.1 Batch mode RO test set-up

4.1.1. Batch-RO experimental result

To simulate the predicted movement of the pump piston in *Section 3.5*, a compressive rate of 8.3×10^{-4} m/s (50 mm/min) was adopted initially. After calibrating the force and the displacement to zero, the Instron machine was started, forcing the piston of the pump cylinder to move downwards. The compressive load increased while the piston displacement moved down, as shown in *Figure 4.2*, and the applied pressure increased correspondingly. At the beginning (O-A), the load increased sharply until around 4.3×10^{3} N (point A). This is due to the build-up of pressure in the solution since below the osmotic pressure no water can pass through the membrane and the volume of the solution remains the same. The displacement therefore corresponds to the mechanical compliance of the set up. At point A, the applied pressure reached 4×10^{5} Pa, which just exceeds the osmotic pressure of 3500 ppm NaCl solution, i.e. 2.8×10^{5} Pa. The freshwater (at around 3 ml/s) was pushed across the membrane by the driving forces provided by the pressure differences. Once water started to permeate the membrane, the pressure increased more gradually (A-B). Permeate rate was raised up to 0.02 l/s due to the magnified net driving pressure. When piston reached its end, the maximum pressurising force amounted to 6.5×10^{3} N, and the corresponding feed pressure was 11×10^{5} Pa. Permeate was continuously driven out as the pressure gradually decreased to around 4×10^{5} Pa, eventually achieving equilibrium with the osmotic pressure. The total collected permeate was 1.8 l, i.e. 66% recovery ratio was achieved, and its salinity was under 500 ppm as expected. Notably, these experimental results are in good agreement with the proposed performance of a batch RO system in *Section 3.5*; thus, we could confidently argue that the mechanically driven batch-RO should be deemed applicable for desalination.

The experiments were also carried out for the following situations: (1) without re-circulating pump and (2) under different compressive displacement rates. Case (1), not surprisingly, underperformed its counterpart with a re-circulating pump and the reasons for this are twofold. Firstly, the trapped air, which could not be eliminated thoroughly, diminished the batch-RO performance due to the amount of work wasted on compressing the air rather

than the solution (prolonged O-A phase). Secondly, because of the imperfect mixing of the solution and the enhanced concentration polarization phenomena arising from the absence of rapid circulation flow, the required compressive load was raised by almost 50% (up to 12.5×10^3 N). Case (2) was carried out to investigate the effect of compressive speed on the system performance, therefore allowing us to identify the optimal operation condition. The experiments demonstrated how susceptible the load and pressure are to the chosen compressive displacement rate. On the one hand, a fast compression, e.g. 2.5×10^{-3} m/s (150 mm/min), would not give adequate time for permeate to cross the membrane and the pressure rose too rapidly, ending up with a huge pressure of 15 bar which could not be provided from the expansion of 9×10^5 Pa compressed air. On the other hand, a slow compressive rate, e.g. 30 mm/min, resulted in a smaller required load (5.74×10^3 N) and pressure (7.5×10^5 Pa); only 1 litre permeate with concentration higher than 500 ppm was obtained which was not desirable.

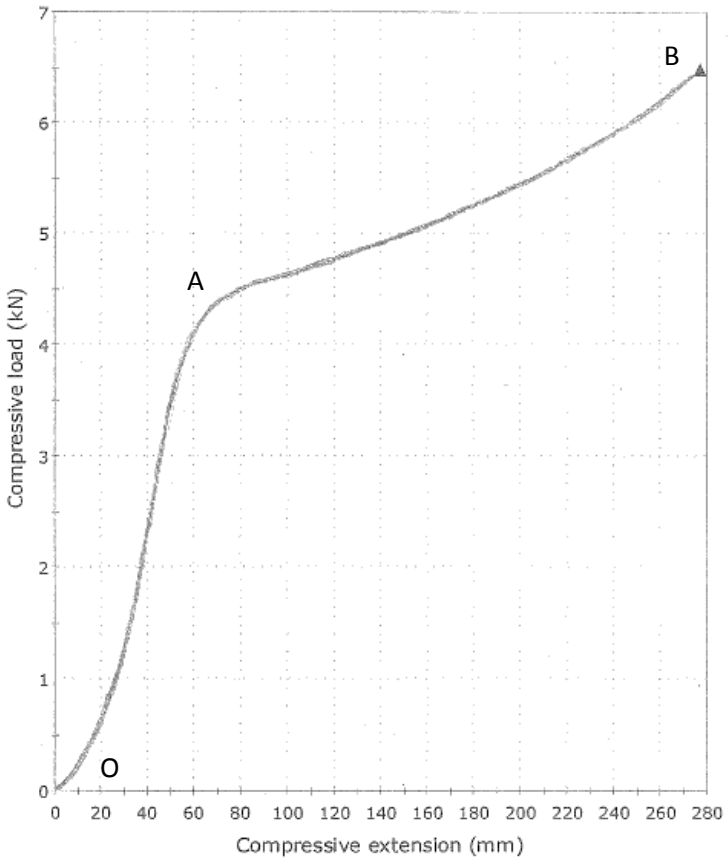

Figure 4.2 Result of experiment with re-circulating pump, test starts point O, permeate starts point A and test finishes point B, i.e. pump piston reaches the end.

4.2. Data acquisition and control system

The successful results from the preliminary experiments of batch-RO meant that the DesaLink rig could be fully developed. For ease of operation, the rig was designed to operate continuously and automatically. Moreover, operation data, both the controlling parameters and instantaneous outputs such as feed power pressure, feed water pressure and concentration, concentrated water (i.e. brine) pressure and concentration, should be recorded and presented on the computer during the process in order to allow real-time supervision and control. Thus, an accurate data acquisition system was implemented as well as a reliable control system (hardware and software). The LabVIEW® software environment from National Instruments was adopted, as it is a well-established and widely used industry standard data-acquisition and control package. The software was utilized to manage data acquisition (by transmission of the output from measurement sensors), data processing (by

internal programming), and to execute the control loop and output the control variables (by means of several magnetic switches and electrical circuits to provide phase-change signals).

The LabVIEW software and hardware (DAQ and modules), together with solenoid valves and sensors of different type, constituted the data acquisition and control system of DesaLink, of which the electronic panel is shown in *Figure 4.3*. All outputs from the sensors were first sent to the signal conditioning modules, which in turn pass on the as-processed information to the data acquisition (DAQ) component housed on a computer providing high-speed multi-channel inputs. Based on the number of samples required, one 4-slot NI DAQ chassis (DAQ9174), three different NI modules (NI9472, NI9421 and NI9203) and a NI USB-6008 were used. The chassis integrates the conditioned signals. The NI9472 module, sourcing digital output, is in charge of power supply for the solenoid valves. The NI9421 module, sinking digital inputs, counts the flow meter digital inputs, which are converted to frequency by the internal programme. The NI9203 module, with current inputs, receives current signals from the conductivity cells and converts them to concentration, while the USB-6008 is responsible for the valve control by receiving the output signals from the magnetic switches.

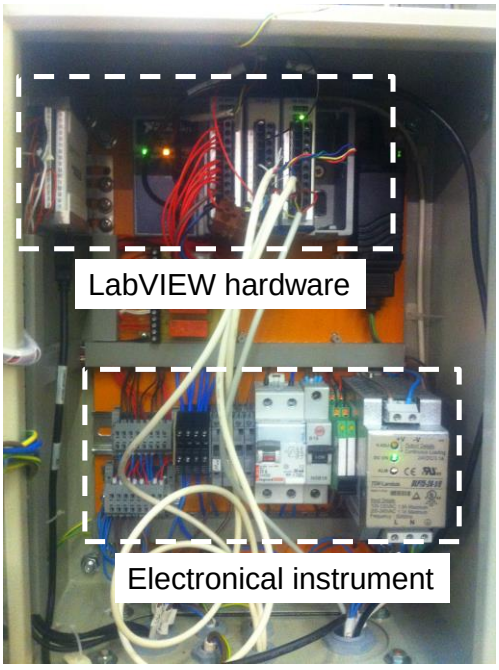

Figure 4.3 DesaLink control panel

The supervisory software code was written using LabVIEW®. It manages the DAQ boards, acquires and processes the data of flows, pressures and concentrations, executes the control loop, and so on. From the virtual control panels, as shown in *Figures 4.4* and *4.5*, one can manage the data acquisition process, monitor the outputs and visualise all the system variables. *Figure 4.4* depicts the structure of DesaLink with major components of the positioned RO module, solenoid valves (labelled as V1-V7), feed pump (M2) and re-circulation pump (M1). The thin lines connecting the valves V1 to V4 indicate the air paths, while the thin lines connecting the two pumps and valves V5 to V7 indicate the water paths. By electronically controlling the pumps and solenoid valves to be on and off, different phases are realised, which can be monitored from the indicators on the top-left corner of the front panel. During the operation, acquired data from all the sensors are depicted in the graphical interfaces (at the bottom of *Figure 4.4*).

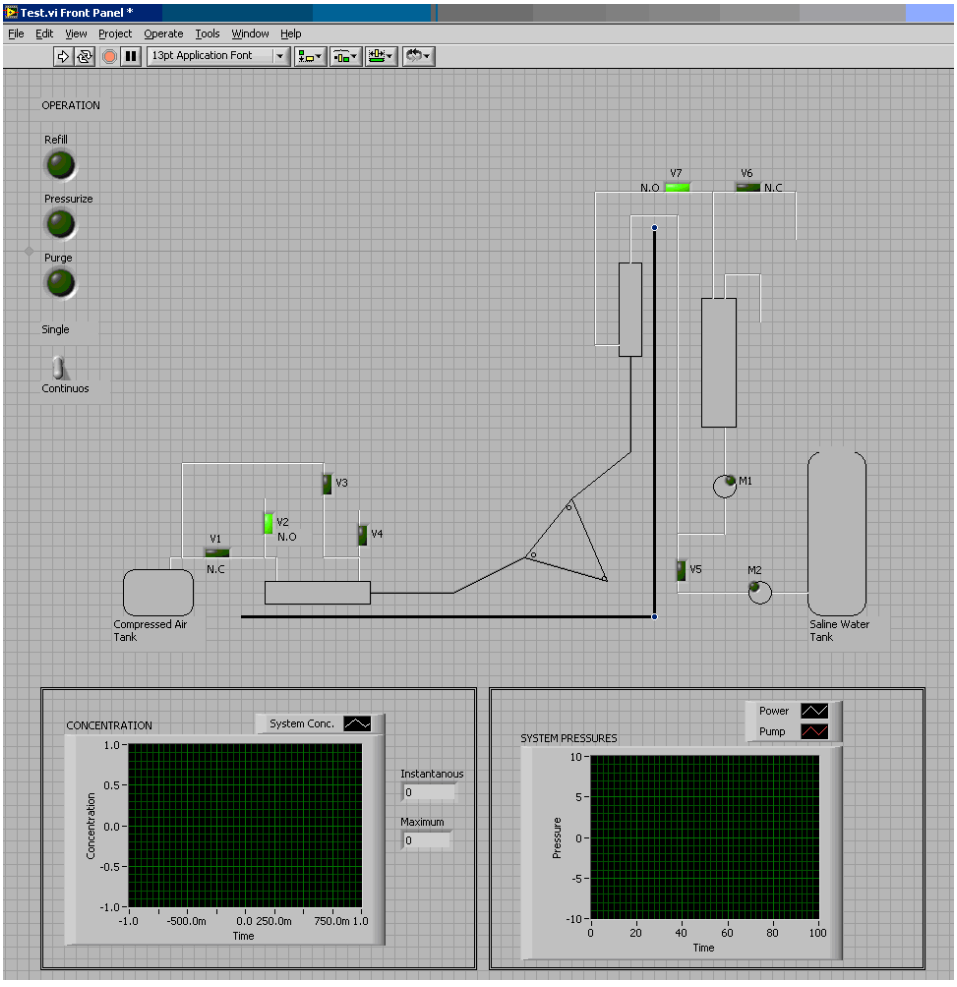

Figure 4.4 LabVIEW® virtual control panel of DesaLink

Take one of the flow sensors as an example, *Figure 4.5* shows both the control panel and the block diagram of the LabVIEW code for the flow censor. From the control panel, one can easily select the data acquisition channel (in accordance with which flow sensor is in use), manage the sample reading type (subject to the type of the flow sensor), and decide the range of frequency input (depending on the sensor output range). Despite the wide variety of data outputs (e.g. current, voltage, and so on), other LabVIEW interfaces for the corresponding other sensors are all similar to this illustrated example. Each variable (pressure, flow and concentration) is sampled at a frequency of 1 kHz. And after every 1 second, all the sampled data (during this interval of 1 second) are averaged and processed for their use in the control loop. The outputs are then logged to disk for further studies.

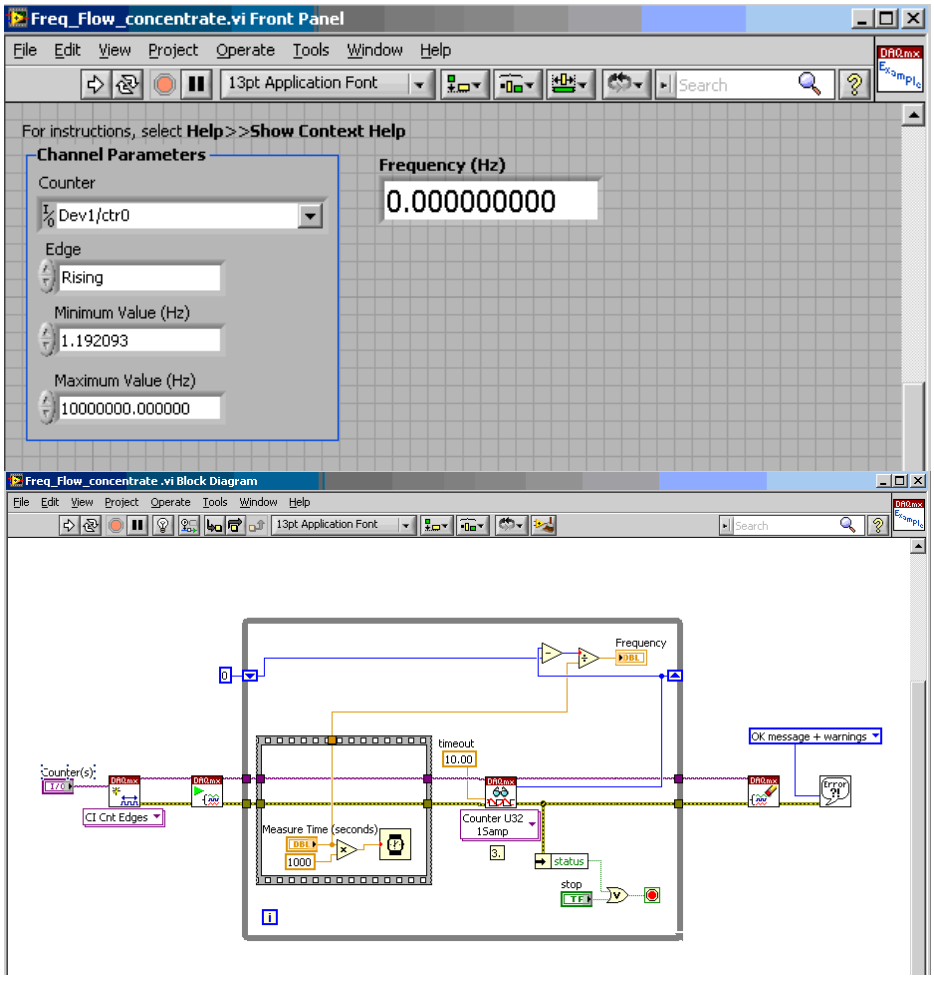

Figure 4.5 LabVIEW® virtual control panel (above) and block diagram (below) of the concentrate flow sensor

4.3. DesaLink system

Based on the understanding of the DesaLink operation process given by the preliminary experiments, the sensors, solenoid valves and pumps that could meet the specific requirements were chosen. Detailed information on the component specifications is summarised and presented in *Appendix C.1*.

The arrangement of the components and sensors on the RO rig frame was carefully planned based on the experience from previous experimental studyies. A galvanised steel frame supporting the power and pump cylinders was designed. All parts of the metal frame had been subjected to a thorough failure modes and effects analysis (FMEA) prior to the actual construction, to help select a suitable metal structure and to ensure the safety and stability of the system meeting industrial standards. Additional bolt holes were included, to allow test with different geometries of the linkage mechanism by, for example, placing the crank at different places (*Figure 4.6*).

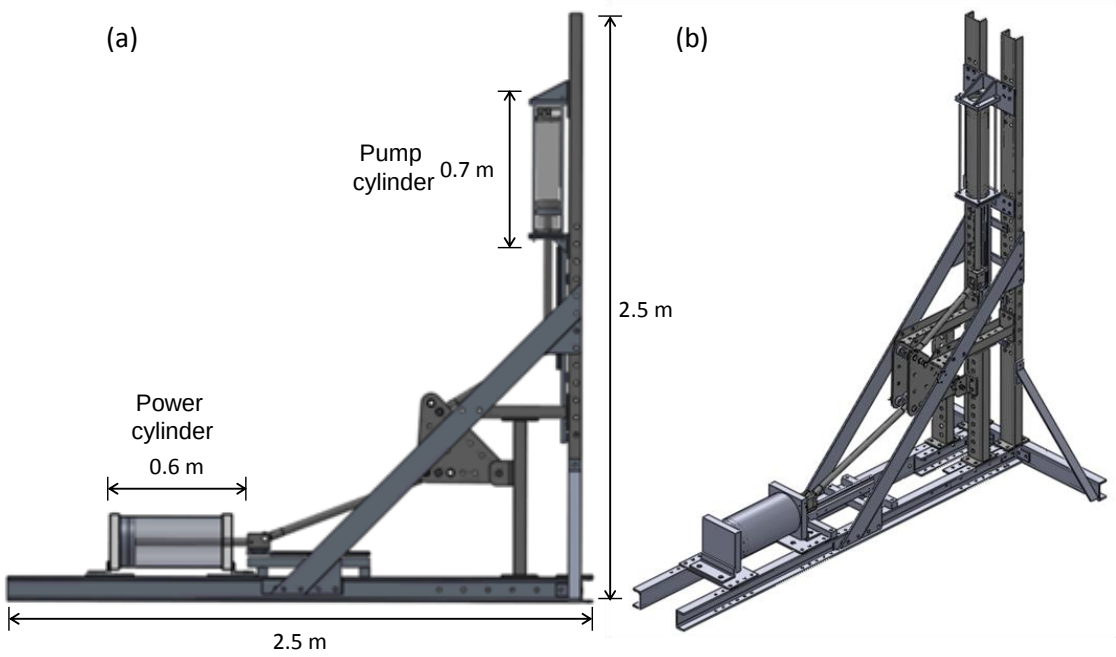

Figure 4.6 Schematic of DesaLink steel frame: (a) a side view; (b) a 45° view

The so-defined principles were followed when building the complete, working prototype of DesaLink, which is as shown in *Figure 4.7*. To save space and shorten the

length of connecting tubes, the RO module was placed vertically on the back of the pump cylinder. Both the water-out path and concentrate-in path were connected to the bottom of the pump cylinder, in order to achieve a good mixing of the feed solution and the high concentration brine which was cycled back to the water cylinder. Pre-testing had been conducted, to ensure the system was totally sealed (i.e. no water leaking or air trapped inside), and more importantly, to calibrate the instrumentation, data acquisition and control system. Practical problems were identified and solved during these pre-tests, such as water leaking, inappropriate data-acquisition sampling and air trapping, after which DesaLink operated throughout.

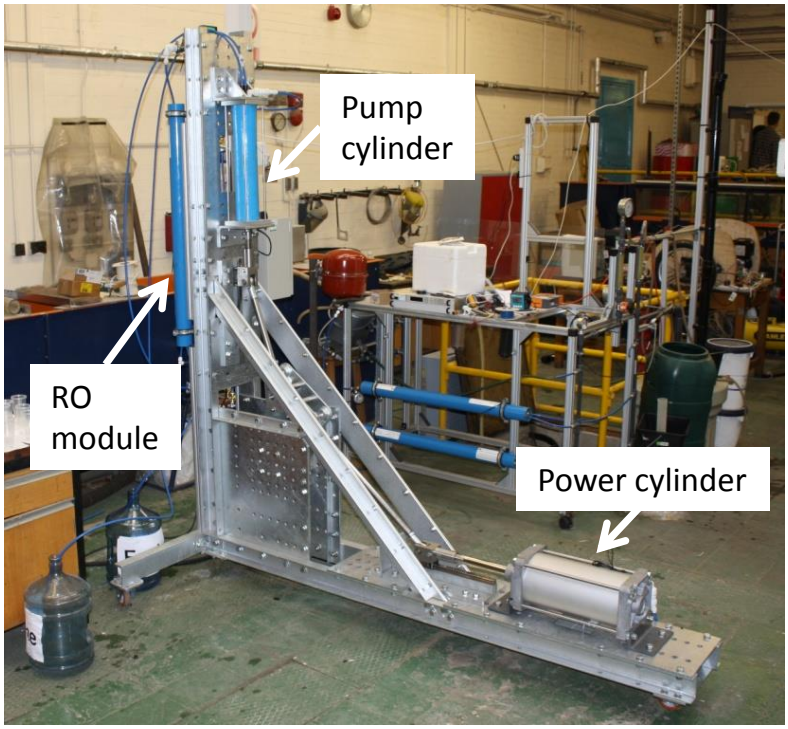

Figure 4.7 DesaLink system

4.4. Experiment procedures

1) Preparing experiment equipment

   a) Prepare salt solution by using the desalinated tap water with an electric conductivity less than 0.1 $\mu S \cdot cm^{-1}$ and a certain amount of analytical grade

sodium chloride (NaCl) salt from Fisher Scientific, prepare the high pressure feed air by using the air compressor.

b) Prepare the computer and Matlab®/LabVIEW® interface.

2) Experiment execution

a) Set the operation mode of the system, e.g. single or continuous and start the experiment.

b) After several times (2–3) of trail tests to smooth the movements between all connections and eliminate any trapped air in DesaLink, then built the data write-in files and record data points.

c) Start experiments.

4.5. Preliminary experimental results

The experimental work with DesaLink provided a step forward beyond the theoretical justification of the batch-RO concept under the ideal conditions, where the system was analysed without taking into account any energy losses.

The key components directly relating to the performance of DesaLink are the power cylinder, pump cylinder and RO module (see *Figure 4.7*). The technical details of the two cylinders and RO membrane module are presented in *Table 3.2*. NaCl solution of 4000 ppm was used as feed water. To simulate steam, compressed air at 9×10^5 Pa was provided to the power cylinder to start the desalination process. After several cycles, measurements were taken and the results are summarized (*Table 4.1)*. From the results, it can be seen that DesaLink yielded a very satisfactory performance in terms of its permeate concentration being lower than 500 ppm (drinking water standard) and a high recovery ratio which is around 70% (purging water was not counted).

Table 4.1 Preliminary results of DesaLink prototype

Preliminary results			
Cycle duration	4 mins 30s	Permeate salinity	320 ppm
Permeate per cycle	2.4 Litres	Brine salinity	11000 ppm
Brine per cycle	1 Litre	Recovery ratio	70%

Details of the process are presented in the following figures. Compared to theoretical predicted values (*Figure 3.14)*, the experimental values of air and water pressures (*Figure 4.8*) follow the similar trends: air pressure decreases after filling point and water pressure increases gradually. And both pressures of air and water experienced four stages, namely air filling, expanding, waiting and purging as labelled in *Figure 4.8*. In the air filling stage, compressed air at 8×10^5 Pa was kept feeding to the power cylinder for a period of time. As a consequence, the water pressure was increased as the pump piston was moved upwards compressing the water with increasing mechanical advantage. The air feeding was cut off after around 1.8 litres air had been fed into the power cylinder. After stopping supplying compressed air to the power cylinder, the sole source of energy to propel the power pistons was the expanding of the high pressure air. During this phase, the air pressure decreased monotonically alongside the operation. Meanwhile, because of the mechanical advantage, water pressure went up after a small drop and reached its maximum when the pump piston arrived at its end, when the pressure of the feed air dropped to around 2×10^5 Pa. At the end of the expanding stage, the water pressure reached the maximum of around 16.5×10^5 Pa which was larger than the osmotic pressure of the bulk solution. Because of the pressure difference, more freshwater was driven to flow through the membrane and a 60-seconds waiting time was set after the expanding stage. During this waiting stage, the water pressure decreased since freshwater continued to come out. The purging process was started when no production of permeate could be detected. Here, fresh feed solution was introduced to the RO module to wash out the brine. After purging, the feed solution refilled the water cylinder, forcing both the power and pump pistons to return to their initial positions, followed by the start of next cycle. In *Figure 4.9*, the feed and permeate flows that correspond to the four

stages are shown. Notably, the feed flow rate varied during the operation because the rising water pressure led to a negative effect on the re-circulation pump.

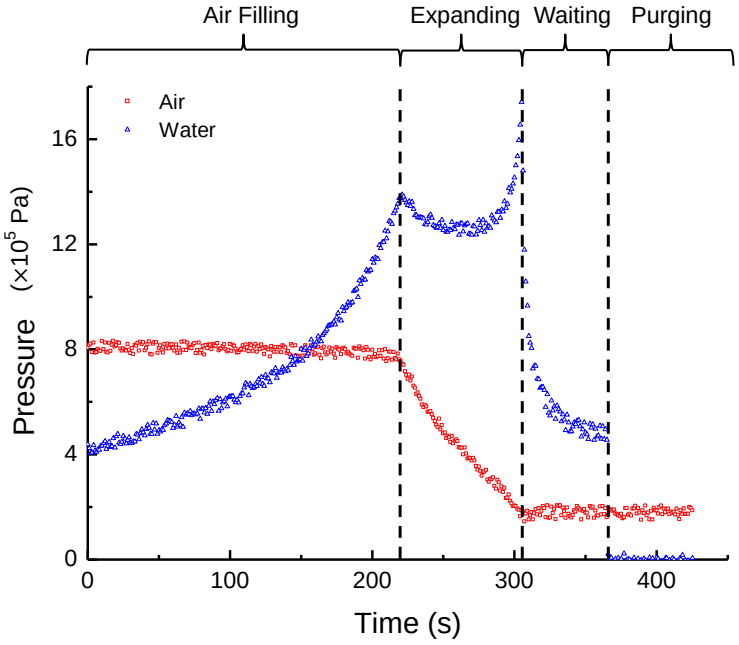

Figure 4.8 Feed air and water pressures. The air filling stage is the initial part of the pressurisation stage, followed by stopping air feeding and allow the compressed air to expand, so call expanding stage. Both of the air filling and expanding stages consist the pressurisation stage stated in Figure 3.9. After air piston reaches the end of the air cylinder, 100 seconds of waiting time was set to allow more fresh water flow through the membrane. After that, purging was conducted as introduced in Figure 3.8.

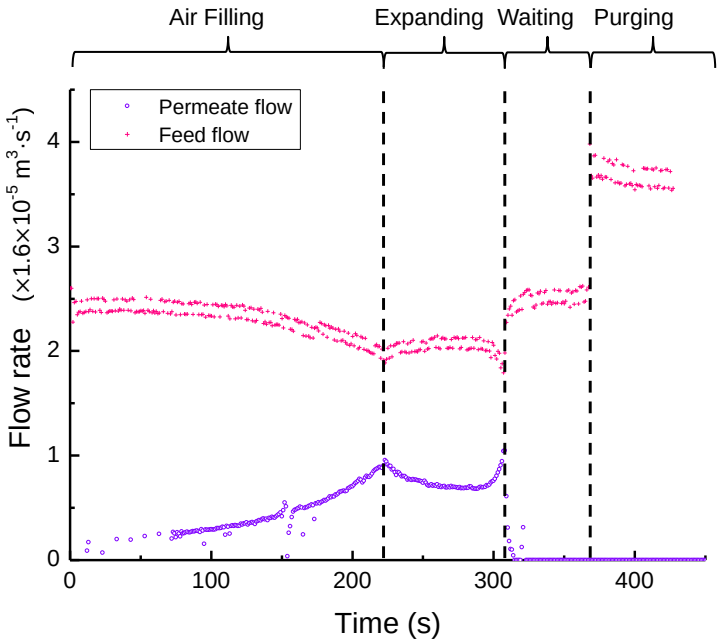

Figure 4.9 Feed and permeate flow rates. The feed flow rate main depends on re-circulation pump. When the water pressure raises, the re-circulation pump is forced to be work lower, so the feed flow rate decreased in the first two stages, after that, the water pressure decreased, so the feed flow rate increase in the last two stages. Permeate flow rate mainly depends on feed water pressure, so it varies with the feed water pressure that represented in Figure 4.8.

4.6. Summary

In this Chapter, the batch-RO process was first introduced, tested and proven by means of a specifically devised test using a materials testing (Instron®) machine. With information obtained from the pre-tests, the prototype DesaLink system was built and fully calibrated to allow smooth operation. The prototype was successfully subjected to preliminary experimental tests under laboratory conditions using compressed air to simulate solar steam. Based on the results obtained, the DesaLink system can be expected to achieve an output of 500 l/day per m^2 of solar collector. This study served as a proof of concept for a batch-RO process for desalination which is capable of achieving high recovery and high efficiency.

One step forward from this Chapter is to look at two major performance-affecting phenomena, namely longitudinal dispersion and concentration polarization. For the purging

phase, ideally, the concentration of the solution at the outlet of the RO module should suddenly drop to the same value as that at the input. However, dispersion causes undesirable mixing of the concentrated brine left in the RO module with the less concentrated feed water. Therefore, the salt concentration and energy usage will increase in the following pressurisation cycle. Beside dispersion, the intrinsic concentration polarization phenomenon which happens during the pressurisation phase also diminishes the performance of DesaLink. Therefore, substantial research on the dispersion and concentration polarization was conducted to minimize their adverse effects on DesaLink, with relevant concepts and detailed examinations being included and discussed in great details in *Chapters 5* and *6*, respectively. Furthermore, once these two negative effects have been examined and comprehensibly understood, the performance of DesaLink can be optimized. With improved experimental results from such a system, accurate analyses will be carried out in *Chapter 7*, to assess DesaLink and, more fundamentally, to provide a basis for building quality simulation models.

Chapter 5

A STUDY OF LONGITUDINAL DISPERSION IN SPIRAL WOUND RO MODULES

To maximise the overall recovery ratio, which is one of the major aims in this research, the amount of purging water used in the purging phase needs to be optimized. In this chapter, the dispersion in different spiral wound RO modules is extensively studied. An analysis that relates the energy efficiency of the batch operation to the amount of dispersion is developed. A theory of dispersion is presented and verified through experiments. Furthermore, the optimised amount of purging water is determined accordingly.

5.1. Introduction

The batch-RO system is expected to give a high recovery ratio with a low SEC, but one factor that could compromise its performance is the longitudinal dispersion in the RO module. As introduced in *Chapter 3*, each cycle of the batch mode process consists of three major phases. *Figure 5.1* shows how the concentration changes at the inlet and outlet of the RO module element during these phases. Ideally, during the purging phase, the concentration of the solution at the outlet of the RO module should suddenly drop to the same value as at the input. However, dispersion causes undesirable mixing of the concentrated brine left in the RO module with less concentrated feed water (*Appendix B.1*), therefore increasing the salt concentration and energy usage in the following pressurisation cycle. An excess of purging water could be applied to bring down the outlet concentration, but this would waste feed water and decrease the recovery ratio of the whole operation.

To maintain a continuous operation and achieve a high recovery and efficiency, the relationship between recovery ratio, energy consumption and dispersion needs to be

established and analysed so that the operation procedure of the batch-RO system can be optimised. Therefore, the objectives of this study are to: (i) develop a theory to represent dispersion in spiral wound membrane modules (SWMs) and its effect on batch-RO operations, (ii) verify the theory and characterise through experiments the dispersion in specific spiral wound RO modules typically used for brackish water desalination, and (iii) as a consequence, quantify the increase in SEC that longitudinal dispersion will cause in practice.

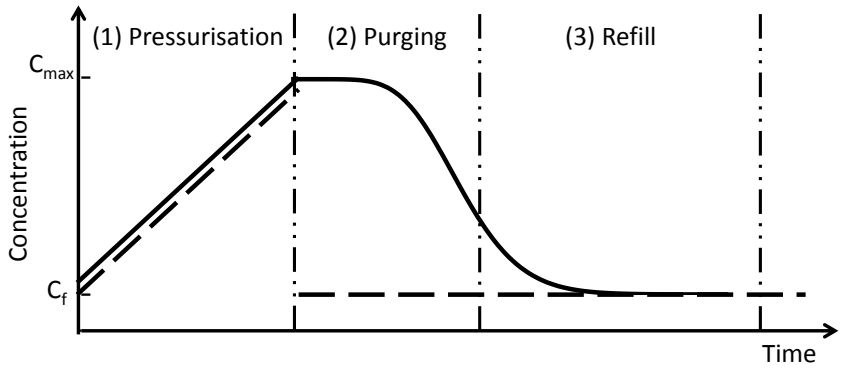

Figure 5.1 Concentration changes at the inlet (dash line) and outlet (solid line) of the RO module during batch mode operation

5.2. Theory

5.2.1. Energy consumption

The analysis assumes that the RO membrane has 100% salt rejection and that, after start up, the system runs steadily, passing through the same conditions from one cycle to the next. It is also assumed that the recirculation flow is sufficient for concentration polarisation effects to become negligible. The recovery ratio r of the system is given as the ratio of the desalinated water produced (during the pressurisation phase) divided by the feed water supplied (during the purging and refill phases):

$$r = \frac{V_{max} - V_0}{(V_{max} - V_0) + V_{pur}} \tag{5.1}$$

where V_{max} is the total maximum volume (m^3) of the system (equals the sum of the the volume of water in pump cylinder and the water volume inside RO module), V_0 is the minimum volume (m^3) of the system, i.e. the volume of the brine left in the RO module, V_{pur} is the volume (m^3) of the purging water used by the time at which purging is cut off. For convenience V_{pur} is defined as $V_{pur} = \beta V_0$ where β is the purge cut–off point.

The fraction of retained salt is defined as $\alpha = m_r/m_{out}$, where m_{out} is the mass (kg) of eluted salt during the purging phase and m_r is the mass (kg) of residual salt left in the RO module (see *Figure 5.5*). Net salt eluted during purging phase:

$$m_{out} = \int_0^{V_{pur}} (C_{out} - C_f)\, dV = (C_{max} - C_f) V_p (1 - \alpha) \tag{5.2}$$

Salt supplied during refill phase:

$$m_{in} = (V_{max} - V_0) C_f \tag{5.3}$$

As each cycle is assumed identical when operating with feed water of same concentration and feed air pressure, and practically no salt passes through the membrane, the net salt eluted during the purge phase is equal to the amount supplied during the refill phase, i.e. $m_{out} = m_{in}$ thus:

$$C_{max} = \left[\frac{r}{(1-r)(1-\alpha)} + 1\right] C_f \tag{5.4}$$

where C_f is the concentration of feed water (kg/m^3) and C_{max} is the concentration at the end of the pressurisation stage (kg/m^3).

The essential work done in the pressurisation phase is:

$$W = -\int_1^2 P \; dV = -\sigma \int_1^2 C \; dV \tag{5.5}$$

where P is pressure (Pa). According to Van't Hoff Law: $\mathrm{C_1V_1 = C_2V_2}$,

$$W = -\sigma V_0 C_{max} \int_1^2 \frac{1}{V} dV = -\sigma V_0 C_{max} \ln \frac{V_{max}}{V_0} \tag{5.6}$$

Then, the SEC for each cycle can be expressed as:

$$SEC = \frac{work\ needed\ per\ cycle}{product\ volume\ per\ cycle} = \frac{\sigma C_{max} V_0\ ln(V_{max}/V_0)}{V_{max} - V_0} \tag{5.7}$$

where σ is the constant for converting the concentration of solution to its corresponding osmotic pressure (assuming the operation temperature kept constant through the experiment).

Substituting *Eq. (5.4)* into *Eq. (5.7)* and simplifying gives:

$$SEC = \sigma C_f \left[\frac{1}{1-\alpha} + \frac{1-r}{r}\right] \frac{1}{\beta} \ln \left[\frac{1 + (\beta - 1)r}{1 - r}\right] \tag{5.8}$$

This compares to the ideal minimum energy consumption (Eq. 2.2) in the case of zero dispersion (i.e. $\alpha = 0$ and $\beta = 1$):

$$SEC_{ideal} = \sigma C_f \frac{1}{r} \ln \left(\frac{1}{1-r}\right) \tag{5.9}$$

To achieve a high recovery and low SEC, the optimum cut–off point β should be applied. *Eq. (5.8)* can be used to determine this optimum, but first the relationship between α

and β needs to be established. This requires an understanding of the dispersion phenomenon.

5.2.2. Dispersion in RO SWMs

The analysis of dispersion in a channel depends on the geometry of the channel. Unfortunately, SWMs have a complex geometry which is not amenable to simple analysis. A useful model, however, is that of Taylor for laminar flow through a cylindrical tube (Taylor 1953). Dispersion in the SWM can be expected to show similar though not identical behaviour to that in the tube. A better approximation should result from adapting Taylor's analysis for the tube to the case of a flat channel. Even compared to the flat channel, however, the SWM differs significantly, due to the presence of the spacer which maintains a certain height between the membranes on their feed side. Here, Taylor's approach is applied to the flat channel and adjustments incorporated to the model based on experimental observations with SWMs. Note that, due to the close spacing of the membranes (<1 mm), only laminar flow occurs in practical situations, and so the case of turbulent flow need not be considered.

Both diffusion and convection contribute to dispersion in flow through a channel. At slow flows, diffusion dominates the dispersion, whereas at fast flow convection takes over. For flow through a tube, as presented in *Figure 5.2*, Probstein (Probstein 1995) maps the different regimes of dispersion against Péclet number $\mathrm{Pe} = \bar{u}a/D$ (where $\bar{u}$ is the mean velocity [m/s], a is the radius or half height of the channel [m] and D is the diffusion coefficient of the salt [m^2/s]) and the tube aspect ratio, which equals L/a, where L is the length of the channel (m).

Figure 5.2 Regions of applicability of various dispersion solutions for a tracer in a capillary tube, from Probstein (1995)

In the range of approximately $1 < \mathrm{Pe} < L/a$, the map suggests that the dispersion coefficient may be predicted according to Taylor's expression:

$$k_{Taylor} = \frac{a^2 {u_0}^2}{192D} \tag{5.10}$$

With considering the convective flow across a rectangular plane which moves at constant velocity of $(\mathrm{u}_0)\, 2/3$, i.e. with the mean velocity of flow,

$$x_1 = x - \bar{u}t = x - \frac{2}{3}u_0 t \tag{5.11}$$

Together with the convection-diffusion equation as follow, where z is the non-dimensional position from the channel midline (the coordinates of x, y and z in the flow channel is shown in Appendix B1, *Figure A.3*),

$$\left(\frac{\partial^2 C}{\partial z^2}\right)_x = \frac{a^2}{D}\left(\frac{\partial C}{\partial t}\right) + \frac{a^2 u_0}{D}(1 - z^2)\frac{\partial C}{\partial x} \tag{5.12}$$

Changing co-ordinates from x to x_1,

$$\left(\frac{\partial C}{\partial t}\right)_x = \frac{\partial C}{\partial x_1}\left(-\frac{2}{3}u_0\right) + \left(\frac{\partial C}{\partial t}\right)_{x_1} \tag{5.13}$$

Substituting *Eq. (5.13)* into *Eq. (5.12)*, and neglecting $\frac{\partial \mathrm{C}}{\partial \mathrm{t}}$,

$$\left(\frac{\partial^2 C}{\partial z^2}\right)_x = \frac{a^2 u_0}{D}\left(\frac{1}{3} - z^2\right)\frac{\partial C}{\partial x_1} \tag{5.14}$$

A solution of *Eq. (5.14)* which satisfies the condition $\partial \mathrm{C}/\partial \mathrm{z} = 0$, at $\mathrm{z} = 1$ is:

$$C = C_{x_1} + B\left(z^2 - \frac{1}{2}z^4\right) \tag{5.15}$$

where B is a constant given by:

$$B = \frac{a^2 u_0}{6D}\frac{\partial C}{\partial x_1} \tag{5.16}$$

The rate of transfer of concentrate across the section at x_1 is:

$$\dot{m} = -2w\int_{y=0}^{y=a}(u - \bar{u})\, C\, dy = -2wa\int_0^1 u_0\left(\frac{1}{3} - z^2\right) C\, dz \tag{5.17}$$

where w is the width of the channel (m). Inserting the value of C and B from *Eq. (5.15)* and *(5.16)*, *Eq. (5.17)* becomes after integration:

$$\dot{m} = 2wa\frac{8}{945}\frac{a^2{u_0}^2}{D}\frac{\partial C}{\partial x_1} \tag{5.18}$$

Thus, the expression of Taylor dispersion is derived for a flat channel and this is applied here to the SWM RO by comparing *Eq. (5.18)* with Fick's law, which expresses the diffusive flux as proportional to the concentration gradient:

$$J_{diff} = -D\frac{\partial C}{\partial x} \tag{5.19}$$

The Taylor dispersion coefficient is:

$$k_{Taylor} = \gamma\frac{8}{945}\frac{a^2{u_0}^2}{D} \tag{5.20}$$

where u_0 is the peak velocity at the centre of the channel (m/s), which is equal to 1.5 times the mean velocity $\bar{u}$. The dimensionless correction coefficient γ is included to allow for the approximations in representing the spiral wound module as a flat channel.

Eq. (5.20) applies to a flat channel of uniform height with the fluid distributed perfectly evenly at its inlet. In practice, there will be non–uniformities due to manufacturing tolerances and some uneven distribution according to the detail design of the inlet and outlet manifolds. An element of fluid entering the module may therefore take a shorter or longer path through the module, resulting in a residence time distribution that is essentially independent of flow rate since this is purely a convective and not a diffusive effect. This heterogeneous path dispersion is characterised by a length L_h (m) such that the corresponding dispersion coefficient is given by:

$$k_{he} = \frac{{L_h}^2}{t_{res}} \tag{5.21}$$

where t_{res} is the mean residence time (s) of the flow.

Thus, the total dispersion coefficient k_{dis} for the RO module is the sum of the contributions from the mentioned two dispersion mechanisms, leading to a quadratic dependence on feed flow rate Q (m^3/s):

$$k_{dis} = \gamma \frac{2}{105} \frac{a^2}{DA^2} Q^2 + \frac{{L_h}^2}{V_0} Q \tag{5.22}$$

where A is the cross–sectional area of the channel perpendicular to the direction of flow (m^2).

Eq. *(5.22)* shows that the dispersion coefficient increases with flow rate. This will result in greater axial mixing of the fluid and a more gradual change in concentration vs. purging volume at the outlet of the RO module. For a tube (or plane channel) initially containing a solution of zero concentration to be displaced by an incoming solution of concentration C_f, Taylor's analysis led to the following formula (which he confirmed by experiment) for concentration C as a function of axial position x from the channel entrance:

$$\frac{C}{C_f} = \frac{1}{2} - \frac{1}{2} erf\left[(4k_{dis}t)^{-\frac{1}{2}} x_1\right] \tag{5.23}$$

where *erf* denotes the error function, t is the time from when the new fluid starts entering the channel, and $x_1 = x - \bar{u}t$, i.e. the position by a particle of fluid moving at the mean speed $\bar{u}$. This experiment is slightly different to that performed by Taylor, in that we measured the concentration at a fixed position $x = L$, corresponding to the length of the RO module, at varying time t. Thus $x_1 = L - L(V/V_0)$, where $V = Qt$ is the volume of purging solution used until time t. This experiment also differs in the sense that the initial concentration in the channel is C_{max} to be replaced (purged) by one of lower concentration C_f. Consequently, *Eq. (5.23)* is re–written to give to the normalised concentration at the RO module outlet as:

$$\frac{C - C_f}{C_{max} - C_f} = \frac{1}{2} - \frac{1}{2} erf\left[(4k_{dis}t)^{-\frac{1}{2}} L\left(1 - \frac{V}{V_0}\right)\right] \quad (5.24)$$

At high Pe numbers $(Pe > 3000)$, the concept of a dispersion coefficient is no longer useful. Because the solute distributions at a time that is large enough that convection is dominant but radial diffusion has not entered the picture. The solute leading edge will be distorted into the parabolic:

$$x = \frac{3}{2}\bar{u}t\left(1 - \frac{y^2}{a^2}\right) \quad (5.25)$$

and,

$$C = 0, \qquad t < L/u_0 \quad (5.26a)$$

$$C = h/2a\,, \qquad t > L/u_0 \quad (5.26b)$$

Let $x = L$, from *Eq. (5.25)*, when $t/t_{res} > 2/3$

$$\frac{C - C_f}{C_{max} - C_f} = 1 - \frac{h}{2a} = 1 - \left[\frac{2}{3(t/t_{res})}\right]^{\frac{1}{2}} \quad (5.27)$$

Thus, convection dominates leading to a graph of concentration vs. purging volume V at the channel outlet that is independent of flow rate. For a simple flat channel, the expression corresponding to *Eq. (5.24)* becomes,

$$\frac{C - C_f}{C_{max} - C_f} = 1 - \left[1 - \frac{2}{3(V/V_0)}\right]^{\frac{1}{2}} \quad (5.28)$$

for V/V_0>2/3, otherwise the right hand side of *Eq. (5.28)* is equal to 1. As in the case of slow flows, the experimental results are expected to vary from this theoretical prediction, again because of the difference in geometry between the SWM and the plane channel on which *Eq. (5.28)* is based. The key point of interest in *Eq. (5.28)* is the absence of any term that is dependent on flow rate Q.

5.3. Experiments

5.3.1. Chemicals preparation

The feed water for all the experiments discussed in this Chapter was prepared using tap water (around 60 ppm) and analytical grade sodium chloride from Fisher Scientific. Feed water of different concentrations was produced in the range of 3000 – 20000 ppm, for the purpose of reproducing the salinity of brackish water (about 1000 – 10000 ppm) and seawater (about 35000 ppm). Only simple binary solutions (water plus salt) were considered in this study. The concentrations of the solutions were calculated from the conductivity measurements using a polynomial derived from DOW's (*Appendix A*).

5.3.2. Instrumentation

The system set up is illustrated in *Figure 5.3*. It mainly consists of the following components:

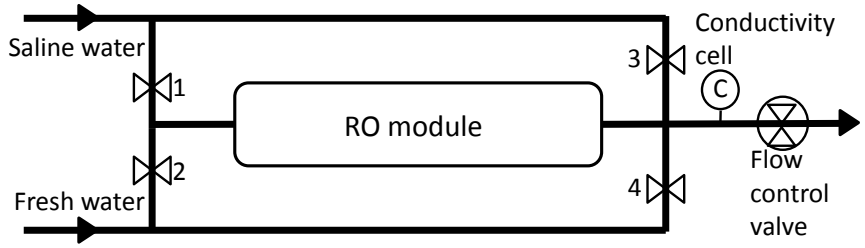

Figure 5.3 Schematic set-up of the experimental system

(1) A saline water reservoir, containing sodium chloride (NaCl) solution.

(2) A fresh (feed) water reservoir, containing tap water with a total dissolved solids (TDS) of about 60 ppm.

(3) A pressure vessel containing a SWM RO module (Dow FILMTEC™ type BW30–2540 or XLE–2540) having active area 2.6 m^2 and nominal channel dimensions of height $2a = 0.71\times10^{-3}$ m, length $L = 1$ m and width 1.3 m giving a nominal volume of $V_0 =$ $0.92x10^{-3}$ m^3. Both the BW30-2540 and XLE-2540 elements are of polyamide thin-film composite membrane, providing a nominal permeate flow of 3.2 m^3/d, and having 99.5% and 99% salt rejection respectively, according to manufacturer specifications.

(4) A flow-through type conductivity cell (Cole–Parmer, SN–19500–58) and transmitter (Cole–Parmer, COND 500) connected to the outlet of the RO module.

(5) A data acquisition system (LabVIEW) to record the conductivity and time.

5.3.3. Procedure

In the experiment, both water reservoirs were placed at least one metre above the horizontal RO module, which enabled the liquid to be driven into the RO module by gravity without using a pump. To represent conditions in the purging phase, the permeate outlet of the module was closed off, and the conductivity cell was connected to the concentrate outlet. All experiments were carried out with the solution at 20±1 ºC. Note that under this range of temperature, the diffusivity of NaCl in water is expected to vary by only ±0.3%. The flow rate was measured with a stopwatch and a graduated cylinder. Excess freshwater was used to flush the RO module thoroughly between experiments, in order to ensure the same starting conditions each time.

Experimental work was carried out at different flow rates to evaluate the above theory and thus to establish the optimum cut–off point for minimum SEC with the help of *Eq. (5.8)*. The standard operation procedure followed in all the experiments was, with reference to *Figure 5.3*: (1) record the conductivities of saline water and freshwater separately by only opening valve 3 or 4 (with valve 1 or 2 respectively closed); (2) wash the RO module with 4×10^{-3} m^3 saline water (of the concentration of interest) by only opening valve 1 (with valve 2, 3, and 4 closed); (3) after the module reaches the steady state, feed in freshwater by only opening valve 2 (with valve 1, 3, and 4 closed).

5.4. Results and discussion

In a series of pilot experiments, the concentration C_{max} of saline water was varied from 3000–20000 ppm. It was found, however, that this variation in concentration had almost no effect on the graph of normalised concentration (i.e. C-C_{fresh}/C_f-C_{fresh}, C_f is the maximum concentration in RO module, C_{fresh} is the concentration of feed fresh tap water.) vs. purging volume, as shown in *Figure 5.4*. In other words, dispersion was independent of C_{max}. The main experiments were therefore carried out with a constant value of $C_{max} = 3000$ ppm, while the flow was varied from 0.8×10^{-6} – 40×10^{-6} m^3/s (0.8 – 40 ml/s). *Figure 5.5* shows an example of the normalised concentration measured at the module outlet shown as a graph against volume of purging liquid discharged. For each experimental run, a curve based on *Eq. (5.24)* was fitted to the corresponding graph by adjustment of the dispersion coefficient k_{dis}. The volume V_0 was also adjusted to fit the results, but only once for the whole series of experiments corresponding to each module type, as this parameter is fixed for a particular RO module.

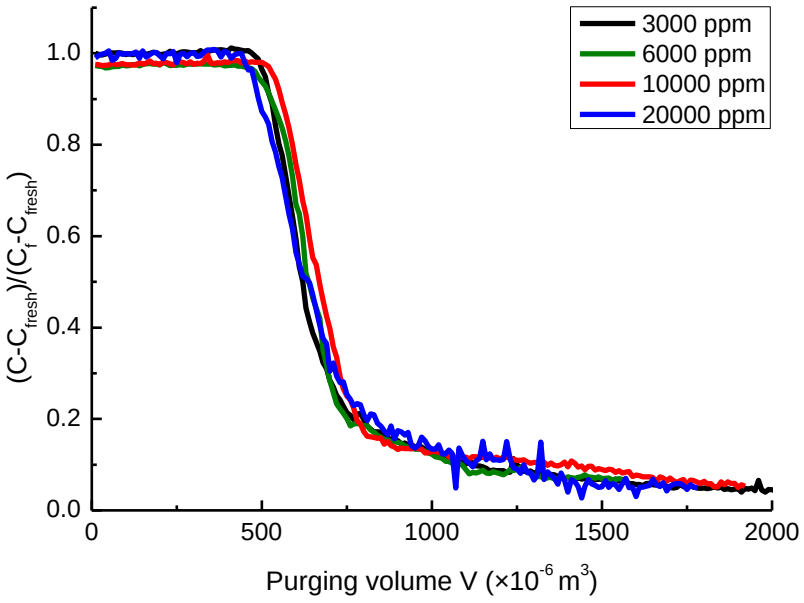

Figure 5.4 Normalised concentration with different concentration solutions under a constant flow rate of about 10×10^{-6} m^3/s (BW30-2540)

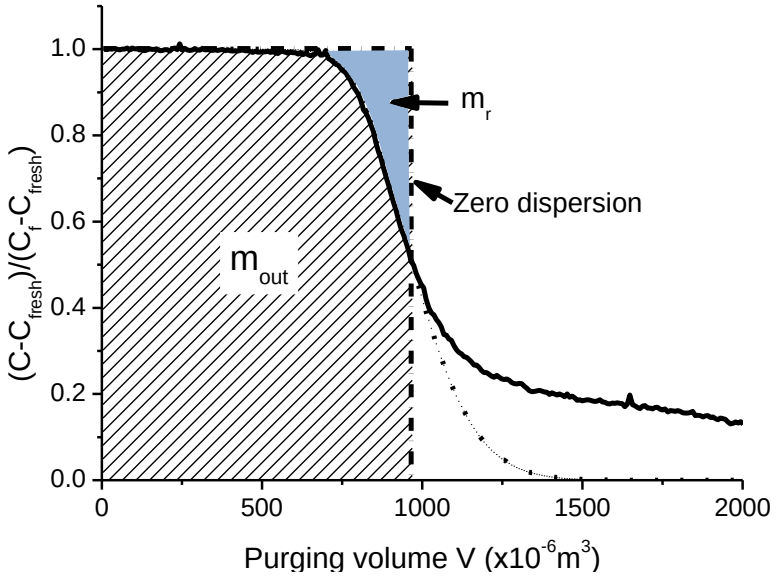

Figure 5.5 Concentration vs. purging volume V at the outlet of the BW30-2540 module at feed flow 20×10^{-6} m^3/s: experimental (solid line), fitting curve (dot line) and ideal zero dispersion curve (dash dot line)

Though *Eq. (5.24)* gave a good representation for the first part of the graph (i.e. when normalised concentration on the vertical axis >0.5), the fit was worse for the tail of the curve corresponding to lower concentrations (see *Figure 5.5*). This may have been due to salt trapping in the membrane leading to slow release of some salt during purging, may also be due to preferential channelling and the bypassing of stagnant zones, so that material lodged here remains trapped for a much longer time. However, the tail of the curve is hardly interesting for the batch-RO operation, because the cut–off will be applied before it is reached. Therefore least-squares fitting was applied to only the first part of the curve in order to determine k_{dis}. *Figure 5.6* shows the values of k_{dis} so obtained, for each membrane type, plotted against flow Q in the range 0.8×10^{-6} – 5×10^{-6} m^3/s (0.8–5 ml/s), the corresponding Pe number range is 320–1200, which fall in the Taylor dispersion region, i.e. $1 < \mathrm{Pe} < (L/a = 2800)$.

A quadratic fitting as hypothesised by *Eq. (5.22)* enables values of γ and L_h to be obtained, as shown in *Table 5.1*. The finding that the value of γ is close to 1 confirms that the treatment of the spiral wound module as a plane channel is reasonable at these lower flow

rates. Further, the values of L_h close to 0.09 m are reasonable in relation to the module lengths of L=1 m, as the characteristic variation L_h in path length should be significantly smaller than the length of the module. From *Table 5.1*, the values of V_0 determined from the experiments differ by as much as 16% from the nominal value of V_0 = 0.92x10^{-3} m^3 based on nominal channel dimensions. This difference may be attributed to manufacturing tolerances and the volumes taken up inside the module by feed spacers and other features.

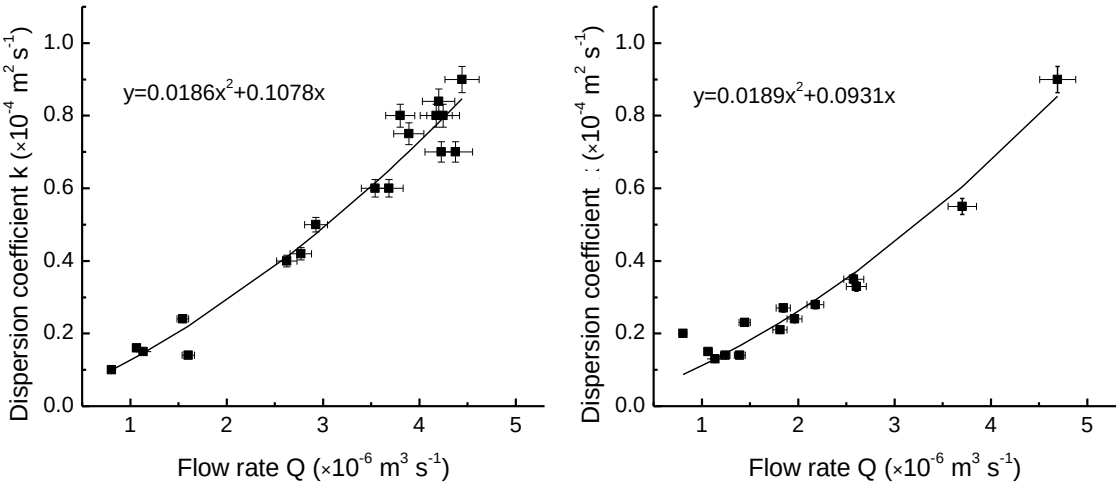

Figure 5.6 Dispersion coefficients under slow flows: for XLE–2540 module (left), for BW30–2540 module (right)

Table 5.1 Experimentally determined parameters for two RO modules

Membrane type	L_h (m)	γ	V_0 (×10^{-3} m^3)
BW30-2540	0.0915	1.01	0.95
XLE-2540	0.0911	0.99	0.77

The experimental results under fast flow rates ranging from 13×10^{-6}–38×10^{-6} m^3/s (13–38 ml/s) for BW membrane element are also represented *(Figure 5.7*). The corresponding Pe numbers vary from 3100 to 10000. As *Eq. (5.28)* predicts, the concentration curves remain almost identical and demonstrate no dependence of the flow rates. Similarly, the concentration curves for the XLE membrane element were independent of flow rate (*Figure 5.8*). It can be concluded that the relationship between α and β has

negligible differences among fast flow rates and the relationships for both BW and XLE RO SWMs are shown in *Figures 5.9* and *5.10* respectively.

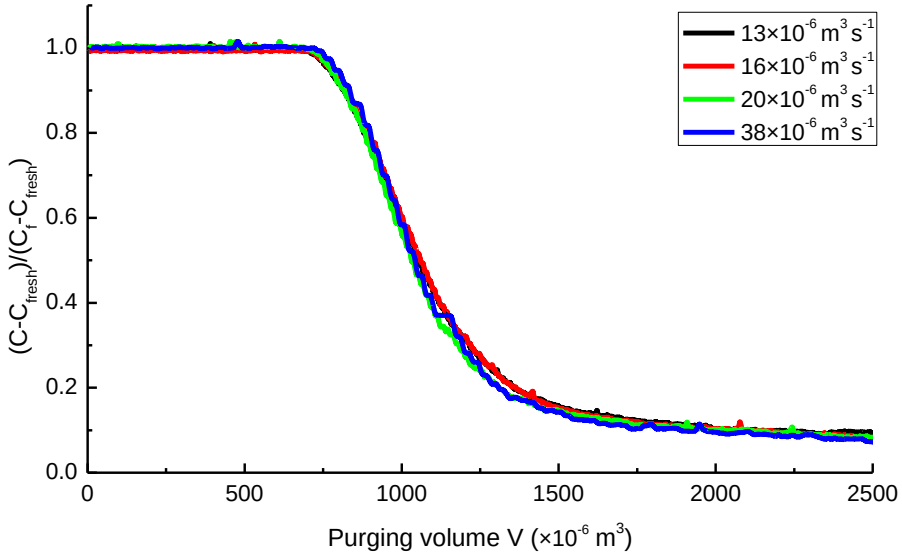

Figure 5.7 Concentration vs. purging volume V under fast flows Q (BW30–2540 module)

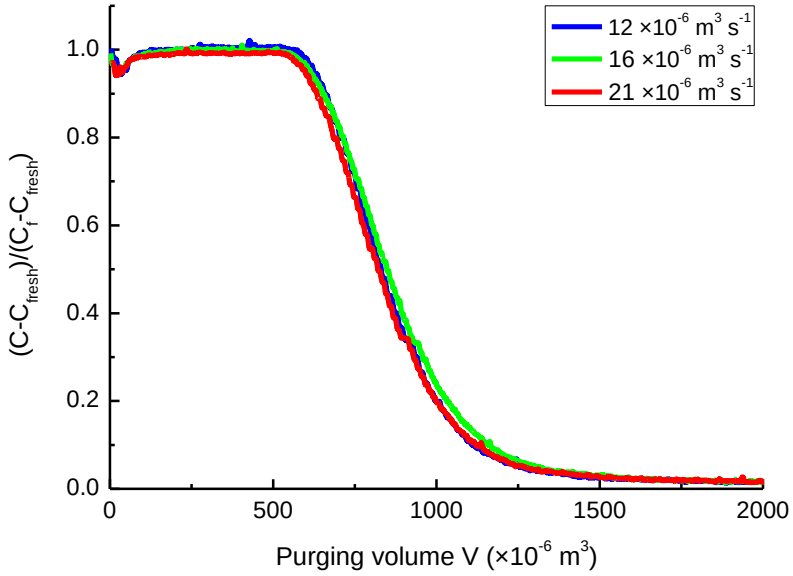

Figure 5.8 Concentration vs. purging volume V under fast flows Q (XLE-2540 module)

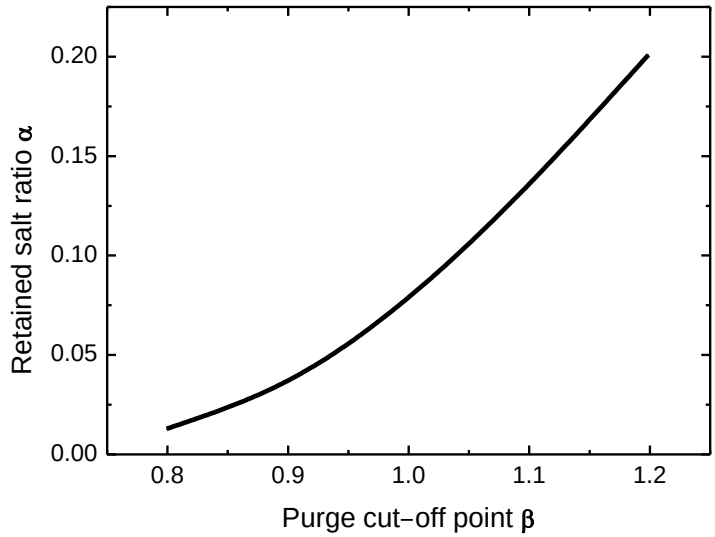

Figure 5.9 Relationship between α and β under fast flows Q (BW30–2540 module)

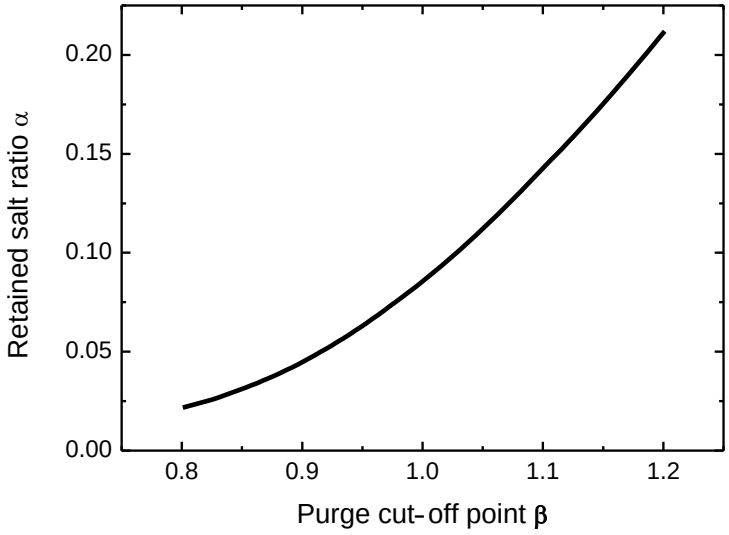

Figure 5.10 Relationship between α and β under fast flows Q (XLE–2540 module)

Based on this observation, *Eq. (5.8)* enables the SEC to be determined as a function of β. SEC is best expressed as a ratio of the ideal case corresponding to zero dispersion, thus the efficiency ratio is defined as $\eta_r = SEC_{ideal}/SEC$. *Figure 5.11* shows, for each membrane type, the relation between η_r and β for fast flow Q and a range of recovery ratios. It shows that the optimum efficiency ratio is consistently achieved when $\beta = 1$.

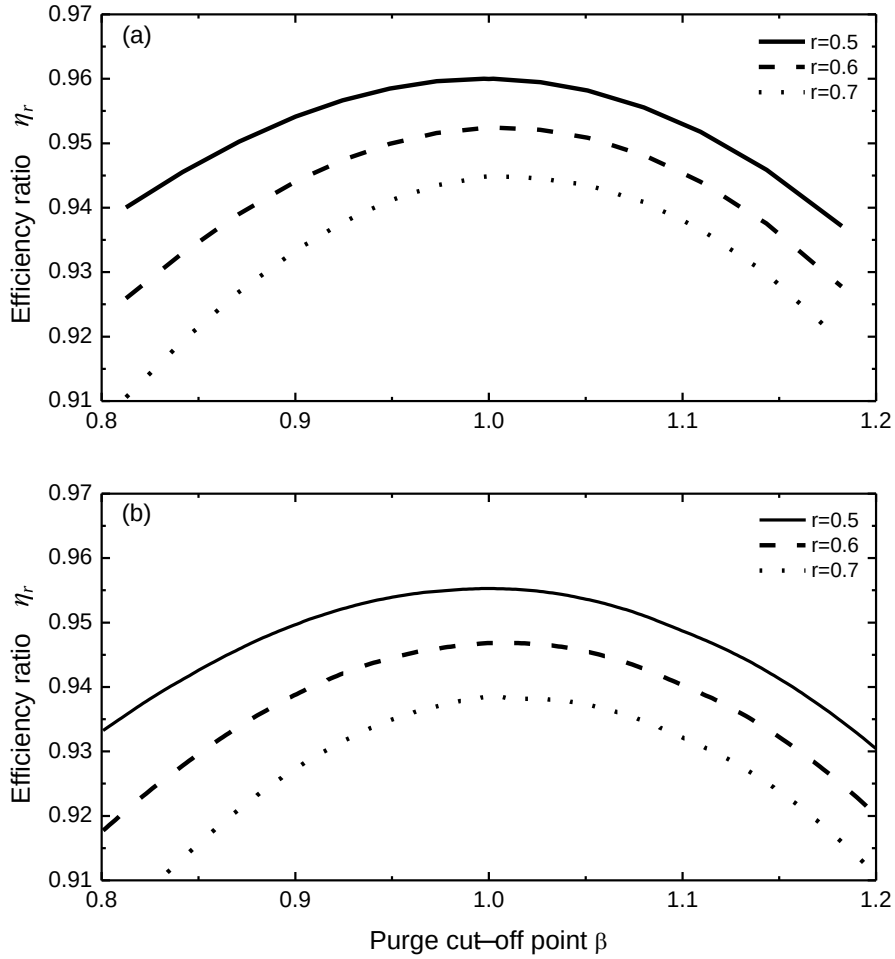

Figure 5.11 Efficiency ratio η_r vs. β for a range of recovery ratios under fast flows Q

5.5. Summary

For the purpose of calculating SEC and recovery ratio in the cyclic batch-RO operation using spiral wound RO modules, longitudinal dispersion phenomena in the RO feed channel were analysed. Various flow rates were investigated and the dispersion behaviour was found to differ between slow and fast flows.

For slow flows, corresponding to $1 < \mathrm{Pe} < L/a$, a model based on the following two mechanisms was adequate: (i) Taylor dispersion, whereby the spiral feed channel is approximated as a planar channel, and dispersion depends on feed flow, channel height and molecular diffusivity of the dissolved salt; (ii) path length heterogeneity, characterised by a dispersion length equal to 9% of the length of the RO module.

For fast flows, corresponding to $Pe > L/a$, dispersion is a purely convective phenomenon and the theory and experiment show that the graph of normalised outlet concentration vs. purging volume becomes independent of flow rate. This graph was established experimentally and the relationship between retained salt fraction α and purge cut–off point β was determined. We found that the optimum cut–off is when the purge volume V_p is equal to the volume V_0 of the solution inside the module i.e. when $\beta = 1$. And at this point, the retained salt is only 8% of the total salt supplied i.e. $\alpha = 0.08$. The experiments showed that $V_0 = 0.95\times10^{-3}$ and 0.77×10^{-3} m^3 for the BW30-2540 and XLE-2540 membrane element respectively.

The main observations and conclusions from the dispersion study are drawn and summarised here: (1) the optimum purge volume is equal to the volume of the solution inside the module, i.e. 0.001 m^3 and (2) to reduce operation time and increase productivity, fast flow rates (20 ml/s to 40 ml/s) are found to be beneficial in practice. In the case of using the optimum purge volume, deterioration in energy efficiency will occur, relative to the ideal case of zero dispersion. This means that to realise a recovery ratio between 0.5 and 0.7, 4.0 and 5.5% more energy will be required for BW30-2540 and XLE-2540 membrane elements, respectively. Thus longitudinal dispersion, though undesirable, causes only a minor penalty in energy efficiency.

Chapter 6
CONCENTRATION POLARIZATION

Besides the aforementioned longitudinal dispersion effect, the concentration polarization (CP) of solute at the membrane surface is another primary cause of the inefficiency. CP is highly undesirable since it depreciates the performance of a batch-RO system as well as that of any other conventional membrane separation system. To predict correctly the osmotic pressure on the membrane surface and the solute rejection by the membrane, it is of paramount importance to quantify the extent of CP in accordance with a given RO module configuration. In this chapter, the characteristics of solute transport are first examined, and then the developments of theories for quantifying the solute mass transfer and CP in both conventional and batch-RO operation processes are proposed and described.

6.1. Introduction

Concentration polarization (*Figure 2.6*) happens in any membrane based separation. The concentration polarization (CP) phenomenon and its negative effects on the separation process have been introduced in *Section 2.3.3*. As a result of CP, the salt concentration near the surface of the membrane exceeds that in the bulk solution by a factor, denoted as CPF hereafter.

To effectively minimise CP, increase the system efficiency and alleviate scaling and fouling problems, the method of varying hydraulic conditions can be adopted. This can be achieved by the introduction of high cross flow velocity or by the incorporation of a feed spacer in the membrane channel. For example, for a commercial standard SWM RO membrane, the contained feed channel spacers increase local shear rates and local

velocities and cause recirculation regions and mixing which increases mass transfer (Li et al. 2002) and reduces CP.

A quantitative understanding of the CP effect and the solute transport characteristics in the RO membrane separation can be achieved by determining the mass transfer coefficient and membrane transport parameters based on various transport models (Sablani et al. 2001; Malaeb and Ayoub 2011). Among these transport models, the film model, and its two variants with either a thermodynamic approach (Spiegler-Kedem model) or a mechanistic approach (Kimura-Sourirajan model) have been most widely used to determine the salt transport characteristics, as they do not require detailed information on the amorphous structure of the RO membrane, which can hardly be described by simple quantitative parameters (Lee et al. 2004). The Kimura-Sourirajan (KS) model is a simplistic model that considers the solute transport solely by diffusion. On the other hand, the Spiegler-Kedem (SK) model describes the solute transport through the membrane as a combination of diffusive flux and convective flux. The weights of the two fluxes are characterized by a parameter termed reflection coefficient.

These models have been carefully examined in several studies presented in the literature to characterise the solute transport in nanofiltration membranes (Gilron et al. 2001; Bhanushali et al. 2002; Chaudry 2002; Ghiu 2003; Lee and Amy et al. 2004) and ultrafiltration membranes (Mochizuki and Zydney 1992; Tandon et al. 1994). The salt transport characteristics through the RO membrane of simple structures, i.e. tubular or flat cell, and the influence of the hydrodynamic conditions were also investigated by others (Brian 1965; Jonsson and Boesen 1977; Sutzkover et al. 2000). The conclusion on the mechanism of solute separation by membranes is still a matter of controversy and more importantly it may be that the mechanism depends on the specific type of RO membrane. For commercial SWM RO elements that are widely used in the RO desalination plants today, a theoretical study of the solute transports in the CP layer is long overdue; therefore, it needs to be thoroughly investigated before making a choice of any existing theoretical models because of the complicated inner structures of SWM RO elements.

The formation of the CP layer depends strongly on the hydrodynamics of the system, and can therefore be varied and even optimized. For the batch-mode RO operation presented in this thesis, a re-circulation pump was adopted to introduce rapid circulation, aiming to effectively minimise energy losses due to the CP and alleviate other CP related negative effects. Since a majority of the previous studies about the CP layer in laminar flow were mainly focused on RO membrane modules with simple structures and could not be considered representative or accurate for the CP in SWM RO elements, the main objectives of this study were to investigate the CP in the SWM RO elements and to quantify reduced energy usage associated with the re-circulation pump.

Firstly, in this chapter, the salt transport characteristics in two different RO elements were studied. Secondly, based on their salt transport characteristics, the appropriate model was selected to correctly describe the mass transport in the RO membrane and quantify the CP value. Emphasis has been placed on establishing separate Sherwood correlations, pertinent to the RO elements in both conventional continuous operation processes and in batch-RO operation process. For both processes, the Sherwood correlations are able to predict correctly the solute rejection in membrane filtration and to estimate the extent of CP. Finally, CP related energy loss in the batch-RO system was quantified accordingly.

6.2. Mass transfer theory

6.2.1. Film model

The film model assumes a one-dimensional flow and a fully developed CP layer. At steady state, as shown in *Figure 6.1*, the solute flux, passing through the membrane J_s (kg·m^{-2}·s^{-1}) is balanced by the convective flux $J_v \cdot C_f$ and the solute diffusive flux from the membrane wall to the bulk solution $D \cdot dC/dx$,

$$J_s = C_p \cdot J_v = J_v \cdot C - D \cdot \frac{dC}{dx} \tag{6.1}$$

where C_f and C_p are the feed and permeate solute concentrations (kg·m^{-3}), respectively, J_v is the permeate flux (m·s^{-1}), and D is the diffusion coefficient (m^2·s^{-1}).

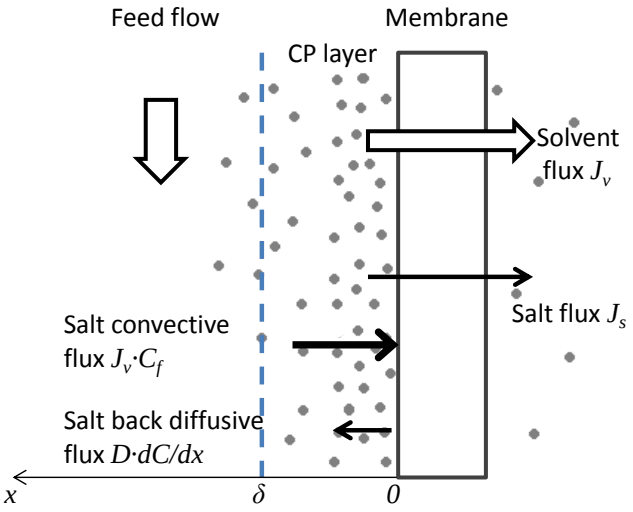

Figure 6.1 Schematic diagram of the solute fluxes across RO membranes

The solution of *Eq. (6.1)* for a boundary layer of thickness δ (cm) gives:

$$CPF = \frac{C_m - C_p}{C_b - C_p} = exp\left(\frac{J_v}{k}\right) \tag{6.2}$$

where C_m and C_b are the solute concentrations (g/cm^3) at the membrane surface and in the bulk solution, respectively. k is the mass transfer coefficient (cm/s) and is defined as:

$$k = \frac{D}{\delta} \tag{6.3}$$

It is worth pointing out here that *Eq. (6.2)* indicates that CPF is strongly dependent on the permeate flux J_v and mass transport coefficient k.

The observed membrane rejection fraction R_o is given by:

$$R_o = \frac{C_b - C_p}{C_b} \tag{6.4}$$

And the real rejection fraction R_{real} is given by:

$$R_{real} = \frac{C_m - C_p}{C_m} \tag{6.5}$$

Writing *Eq. (6.2)* in terms of observed rejection fraction R_o and real rejection fraction R_{real} gives:

$$\frac{1 - R_o}{R_o} = \frac{1 - R_{real}}{R_{real}} \cdot exp\left(\frac{J_v}{k}\right) \tag{6.6}$$

Rearranging *Eq. (6.6)* arrives at:

$$ln\left(\frac{1 - R_o}{R_o}\right) = \frac{J_v}{k} + ln\left(\frac{1 - R_{real}}{R_{real}}\right) \tag{6.7}$$

6.2.2. Kimura-Sourirajan model

The Kimura-Sourirajan (KS) model, also known as the combined solution-diffusion/film model, assumes that the solvent and solute fluxes do not interact with each other (Ho and Sirkar 1992). The solvent is transported through the membrane in a viscous flow (Ghiu 2003) whereas the solute is transported solely by diffusion.

In the KS model, the solvent flux J_v through the membrane is given by:

$$J_v = L_p \cdot (\Delta P - \Delta OsmP) \tag{6.8}$$

The solute flux J_s, according to KS model, is expressed as:

$$J_s = P_s \cdot (C_m - C_p) \quad (6.9)$$

where L_p is the intrinsic membrane permeability ($m^3 \cdot m^{-2} \cdot s^{-1} \cdot Pa^{-1}$), i.e., pure water permeability, ΔP is the operating pressure (Pa), and $\Delta OsmP$ is the difference in the osmotic pressure across the membrane (Pa), which equals to $(OsmP_{mem} - OsmP_p)$. P_s is the salt permeability coefficient ($m \cdot s^{-1}$), which characterizes solute transport through the membrane.

Combining *Eqs. (6.5)*, *(6.6)* and *(6.9)* to eliminate the unknown parameters C_m and R gives:

$$\frac{J_v}{k} = ln\left(\frac{1 - R_o}{R_o}\right) - ln\left(\frac{P_s}{J_v}\right) \quad (6.10)$$

6.2.3. Spiegler-Kedem model

In the Spiegler-Kedem (SK) model, the mass transport through the membrane is characterized not only by solute and solvent permeabilities but also by reflection coefficients σ_1 and σ_2. In contrast to the KS model, the transport of solute is a combination of diffusive flux ($P_s \cdot \Delta OsmP$) and convective flux ($J_v \cdot C_{avg}$), which is indicated by the summation of these two terms in *Eq. (6.12)*.

The following equations of the SK model describe the fluxes through the membrane:

$$J_v = L_p(\Delta P - \sigma_1 \cdot \Delta OsmP) \quad (6.11)$$

$$J_s = P_s \cdot \Delta OsmP + (1 - \sigma_2) \cdot J_v \cdot C_{avg} \quad (6.12)$$

where σ_1 is the reflection coefficient, σ_2 is the coefficient of coupling between salt and water, and C_{avg} is the average salt concentration across the membrane (g/cm^3).

The reflection coefficients σ_1 and σ_2 express the degree of solute-membrane interaction, and their values are in the range of $0 \leq \sigma \leq 1$. A reflection coefficient σ_1 being

unity corresponds to the ideal 100% salt rejection of the membrane, while zero points to entirely unselective membranes. The coefficient σ_2 is zero for the perfect coupling, meaning that solute transport is dominated by convection. Whereas, it reaches unity when there is no solute-solvent coupling, in other words, solute transport is solely governed by diffusion (Spiegler and Kedem 1966; Ghiu 2003). It should be noted that the SK model coincides with the KS model in the limiting case of $\sigma_1 = \sigma_2 = 1$.

Given that the KS and SK models are conceptually different, the appropriate model describing the solute transport characteristics through the membranes used in this research was determined first. Following that, a more dedicated investigation of mass transfer coefficient k was conducted.

6.3. Sherwood correlation

Most of the mass transfer models adopted in the characterization of RO or ultrafiltration membranes make use of the Sherwood correlation (Gekas and Hallström 1987; Sablani and Goosen et al. 2001; Ghiu 2003) in order to quantify the concentration at the membrane wall. The Sherwood correlation indicates to what extent mass transfer rate is affected by Reynolds number, i.e., flow region, and hydraulic conditions.

For fully developed turbulent and laminar flows, the generalized correlations of mass transfer coefficient have the following empirical forms, respectively (Bird et al. 1960; Gekas and Hallström 1987; Xuesong 1987; Cussler 1997):

$$Sh = \frac{k \cdot d_h}{D} = a_{Sh} \cdot Re^{\alpha_{Sh}} \cdot Sc^{\beta_{Sh}} = a_{Sh} \cdot \left(\frac{u \cdot d_h}{v}\right)^{\alpha_{Sh}} \cdot \left(\frac{v}{D}\right)^{\beta_{Sh}} \tag{6.13}$$

$$Sh = \frac{k \cdot d_h}{D} = z \cdot Re^{\alpha_R} \cdot Sc^{\beta_S} \cdot \left(\frac{d_h}{L}\right)^{\gamma} = a_{Sh} \cdot \left(\frac{u \cdot d_h}{v}\right)^{\alpha_{Sh}} \cdot \left(\frac{v}{D}\right)^{\beta_{Sh}} \cdot \left(\frac{d_h}{L}\right)^{\gamma_{Sh}} \quad (6.14)$$

where a_{Sh}, α_{Sh}, β_{Sh} and γ_{Sh} are constants that vary for different diffusion physical situations, and they can be determined experimentally. Sh is the Sherwood number, Re is the Reynolds number, Sc is the Schmidt number, u is the crossflow velocity ($m \cdot s^{-1}$), v is the kinematic viscosity ($m^2 \cdot s^{-1}$), L is the channel length (m) and d_h is the hydraulic diameter (m).

The correlations, i.e. *Eqs. (6.13)* and *(6.14)*, indicate the Sherwood number varies with Reynolds number and Schmidt number, which latter is a characteristic of diffusion. In other words, the mass transfer coefficient k is in essence a function of the crossflow velocity u, diffusion coefficient D, fluid properties, and the membrane module configurations.

Most of the mass transport models for membrane separation use some specifically tuned Sherwood correlation to quantify the concentration at the membrane wall C_m. For a fully developed turbulent flow, one widely used Sherwood correlation is (Gekas and Hallström, 1987):

$$Sh = 0.023 \cdot Re^{0.8} \cdot Sc^{0.33} \quad (6.15)$$

For a fully developed laminar flow, it has the form (Bird and Stewart et al. 1960):

$$Sh = 1.86 \cdot \left(Re \cdot Sc \cdot \frac{d_h}{L}\right)^{1/3} \quad (6.16)$$

In practical SWM RO elements, the spiral geometry can be adequately approximated by an unwound flat rectangular membrane channel. Because the feed channel is too narrow and the mean crossflow velocity is usually less than 0.8 $m \cdot s^{-1}$, turbulent flow is unlikely to be fully developed, and laminar flow may be assumed. However, the occurrence of recirculation

regions, resulting from the increased local shear rates and velocities due to the feed channel spacers (Schwinge et al. 2004), suggests that laminar flow cannot be fully developed. Thus, most existing Sherwood correlations reported in the literature for fully developed turbulent or laminar flow may not be suitable for the determination of mass transfer coefficient in the RO SWM elements, since their flow geometries, hydrodynamic entrance effects, and feed channel spacers are different from one another's.

6.4. Methodologies

For the continuous process, the operation parameters, such as feed flow rate, feed pressure and feed concentration, are all kept constant, which is a primary difference with the batch mode operation. Thus, different methodologies were applied to the determination of mass transfer in continuous operation and batch mode operation. For the two operation modes, the mass transfer coefficients are firstly determined, and the specific Sherwood correlations are thereafter estimated.

6.4.1. Continuous operation

In conventional continuous operation, because of the constant feed concentration, a straight forward experimental procedure was used:

For pure water, based on *Eq. (6.8)* or *(6.11)*:

$$(J_v)_{water} = L_p \cdot \Delta P \tag{6.17}$$

Using a linear parameter estimation method, with the data for J_v obtained at different operation pressures while maintaining a constant feed flow rate for each experiment with pure water, the intrinsic membrane permeability L_p was estimated. Then, a series of experiments were performed for different feed flow rates with a constant feed concentration and operation pressure. With measured permeate flux J_v and permeate concentration π_p, the concentration at the membrane surface π_m was calculated based on *Eq. (6.8)* or *(6.11)*. The values of CPF and mass transfer coefficient k were subsequently obtained using *Eq. (6.2).*

6.4.2. Batch mode operation

For the batch-RO operation, a graphical method is adopted. From *Eq. (6.13)* or *(6.14)*, the relationship between the feed velocity u and mass transfer coefficient k is of the form:

$$k = \frac{u^{\alpha_{Sh}}}{b} \tag{6.18}$$

Combining *Eqs. (6.18)* and *(6.10)* gives:

$$ln\left(J_v \cdot \frac{C_p}{C_b - C_p}\right) = ln\, P_s + b \cdot \frac{J_v}{u^{\alpha_{Sh}}} \tag{6.19}$$

Eq. (6.19) provides a linear relationship between $ln\left(J_v \cdot C_p / C_b - C_p\right)$ and $J_v / u^{\alpha_{Sh}}$. On the basis of experimental results for the batch mode, which are collected at various flow velocities and various feed pressures, the value of C_b is calculated based on mass balance of the desalination process, after which the value of the velocity exponent α_{Sh} is determined from the best linear fit of the measurements. And both the salt permeation parameter P_s and the coefficient b can be obtained. The Sherwood relationship can then be easily worked out with the known parameters α_{Sh} and b.

6.5. Experimental set-up and procedure

6.5.1. Continuous operation

Two commercially available polyamide thin-film-composite membrane elements were used in this study, namely BW30-2540 (brackish water membrane) and XLE-2540 (low energy membrane). Both of them were from Dow® FilmTec® and in the spiral wound element form. Given the diameter of the element and the total membrane area being provided by the manufacturer, the feed flow channel height and width were determined accordingly. The two membrane elements were of the same size, i.e. 0.06 m in diameter and 1 m in length. The

average flow channel height was 7.1×10^{-4} m, with the channel length and width being 1 and 1.3 m, respectively. Both of the elements have 2.6 m^2 active membrane area, but with different salt rejection ratios being 99.5% for BW membrane and 99% for XLE membrane. According to the data provided by the manufacturer, the pure water permeabilities of the two membrane elements are different, one being 9.14×10^{-12} $m\cdot s^{-1}\cdot Pa^{-1}$ for the BW membrane element and the other being 2.03×10^{-11} $m\cdot s^{-1}\cdot Pa^{-1}$ for the XLE membrane element.

A schematic diagram of the experimental unit is illustrated in *Figure 6.2*. The unit consists of the membrane element, feed pump, water reservoir and pulsation dampener. The COMAP pulsation dampener was installed between the feed pump and the membrane element to smooth the feed flow from the pump. The *Wilo* re-circulation pump was installed before the membrane element. Concentrate and permeate flows were mixed in a bucket prior to entering the feed tank. Feed solution was prepared using the desalinated tap water with an electrical conductivity less than 0.1 $\mu S\cdot cm^{-1}$ and a certain amount of analytical grade sodium chloride (NaCl) salt from Fisher Scientific. The operation pressure and feed flow rate were simultaneously controlled by adjusting the power supply and the throttle valve located at the brine stream. Both concentration and temperature of the permeate flux were monitored by a *EUTECH COND 500* conductivity transmitter which was embedded with a temperature-measuring function. The conductivity of the feed solution in the water tank was measured using a *Hanna HI 8733* conductivity meter. The concentrations of solution were calculated from the conductivity measurements using specific conductance for NaCl at specific temperatures. Both the concentrate flow rate and permeate flow rate were measured with a stop watch and measuring cylinders. The concentration of concentrate flow was calculated based on the conservation of mass.

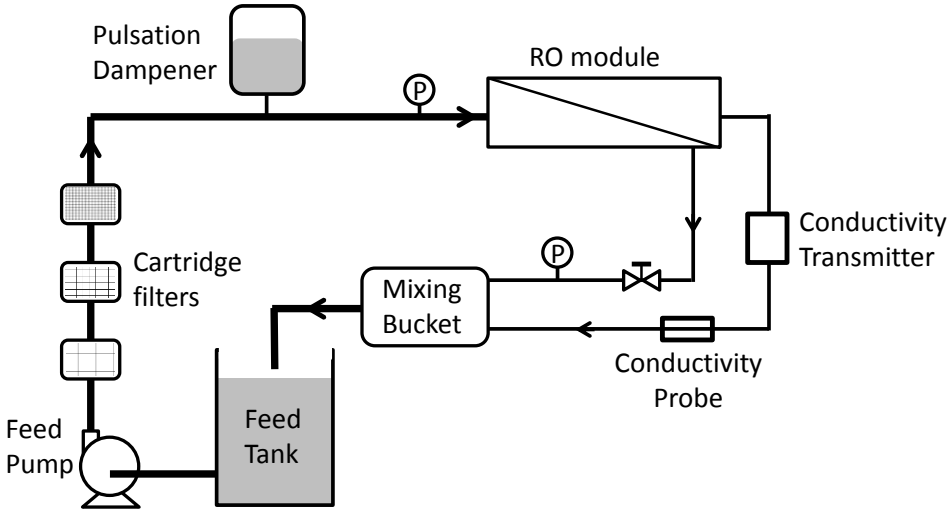

Figure 6.2. Experimental set-up for the mass transport experiments

Prior to the experiments, two brand new membrane elements (one for each type) were conditioned by feeding 3 $kg \cdot m^{-3}$ (3000 ppm) NaCl solution for 12 hours at 9×10^5 Pa (9 bar). The mass transport experiments were carried out with 800 ppm NaCl solution at the fixed operation pressure of 2.76×10^5 Pa (40 psi). The feed flow rates were varied by adjusting supply pump power. In all cases, the membrane processes were stabilized for 1 hour before taking the measurements, carefully ensuring the permeate concentration and flow rate remained almost constant, i.e. the system reached a steady state. The bulk solution coming out of the membrane element as well as the permeate were sampled simultaneously. All the experiments were performed in the temperature range of 298.15±0.5 K (23±0.5 ºC).

6.5.2. Batch mode operation

For the batch mode operation (operation method refers to *Section 4.4*), the DesaLink system was used to generate experimental results. Different re-circulating flow rates were tested to reveal the relationship between CP and unstable hydraulic conditions. For all the experimental sets, the feed concentrations and feed air pressures were kept the same as 2.5 $kg \cdot m^{-3}$ (2500 ppm) and 8×10^5 Pa (8 bar), respectively. The average feed flow rates were 0.04, 0.03 and 0.026 $\times 10^{-3}$ $m^3 \cdot s^{-1}$ (2.4, 2.0 and 1.6 l/min) separately. Repetition of experiments was conducted to exclude possible systematic errors.

6.6. Results and discussion

6.6.1. Salt transport characteristics

As introduced in *Section 6.2*, the SK and KS models give conceptually different explanations of solute transport mechanisms. In this study, we first selected an appropriate model between the SK and KS models to describe salt transport in the membrane elements studied here. With the chosen model, we then calculated mass transfer coefficients k for both membrane elements, followed by a thorough investigation of the salt transport characteristics in the CP layer and through the semi-porous structure of the membrane elements.

For continuous mode operation, the salt transport characteristics in different membrane elements were elucidated and illustrated in *Figure 6.3*, where the variation of observed salt rejection fraction R_o with permeate flux J_v and different feed concentrations for the two membrane elements were presented.

From *Figure 6.3*, for both membrane elements the observed salt rejection fraction R_o is slightly lower for the feed solution of a higher concentration. For the BW membrane element only around 1% difference in R_o was observed for all the concentrations of feed solution ranging from 0.06 kg·m^{-3} (60 ppm tap water) to 5 kg·m^{-3} (5000 ppm), while approximately 2% difference in R_o was found for the XLE membrane element in the same concentration range. It thus can be argued that the salt rejection property of membranes is trivially affected by the concentration of feed solutions, at least for the range of interest in our work. Both of the elements displayed high salt rejection fractions, the average values of R_o for the BW and XLE membrane elements were 95% and 90%, respectively. As shown in *Figure 6.3(b)*, for the BW membrane element, the observed salt rejection R_o remained almost constant with increasing solvent flux J_v. As the permeate flux increased to about 2.3×10^{-6} m·s^{-1} permeate flux and above, the R_o reached 92% and levelled off thereafter. In contrast, for the XLE membrane element as shown in *Figure 6.3(a)*, the R_o was less than 60% at low J_v (approximately 1.0×10^{-6} m·s^{-1}), but it rapidly increased and reached almost 90% when J_v was

2.3×10^{-6} m·s^{-1}. Unlike the plateau at higher J_v of the BW membrane element, the observed solute rejection fraction R_o dropped off beyond the value of 6.9×10^{-6} m·s^{-1}.

Based on *Eq. (6.7)* which characterizes the film model, it should be noted that the true salt rejection R is independent of permeate flux J_v, and the observed solute removal R_o is decided by J_v directly, which is supported by the results shown in *Figure 6.3*. According to *Eq. (6.1)*, if the solute passing through the membrane increases (with accordingly decreased observed solute removal fraction R_o) with increasing solvent flux J_v, then it can be established that the solute transport through the membrane is dominated by convection (convective flux $J_v \cdot C_f$). The salt transport characteristic of the XLE membrane element, as illustrated in *Figure 6.3(a)*, is in line with this description, i.e., R_o decreases at high solvent flux J_v. On the other hand, when the solute transport is dominated by diffusion, the R_o monotonically increases until its levelling off with increasing J_v, which is again demonstrated by the BW membrane element results in *Figure 6.3(b)*. On the basis of these observations, the KS model, which describes the solute transport through the membrane solely by diffusion, was adopted to characterize the transport mechanism in the BW membrane element.

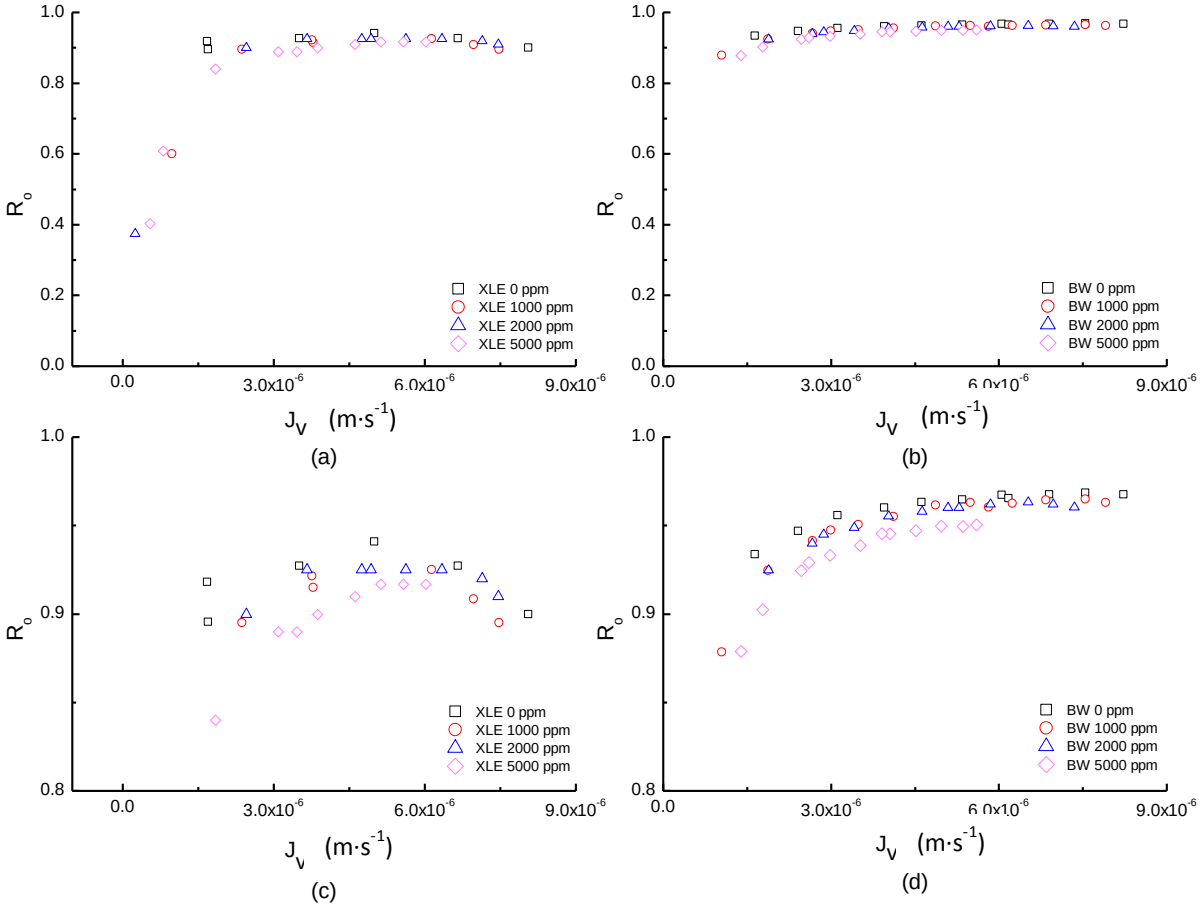

Figure 6.3 Observed solute removal (R_o) by membrane elements with respect to permeate flux (J_v): (a) XLE-2540 membrane element (with the zoom-in figure shown in (c)), (b) BW30-2540 membrane element (with the zoom-in figure shown in (d)), in steady operation

Beside the experimental results of the steady operation (continuous mode) that demonstrate the different mass transfer mechanisms in RO membranes, the experimental results of the un-steady operation (batch mode) have also indicated a similar manner (*Figure 6.4)*. For a BW membrane *(Figure 6.4 a*), the average concentration C_{p_ave} of permeate is decreased with increasing operation pressure. This indicates the observed solute removal R_o is increased with increasing J_v. For the XLE membrane (*Figure 6.4(b)*), the reversed trends are observed, the C_{p_ave} is decreased, with increasing operation pressure, which means the R_o is decreased with increasing J_v. Notably, for feed water of 4 kg·m^{-3} (4000) ppm solute, the product permeate from DesaLink in conjunction with the XLE element had an average

concentration above 0.5 kg·m^{-3} (500 ppm, drinking water limit), thus the XLE element was not used in DesaLink operation thereafter.

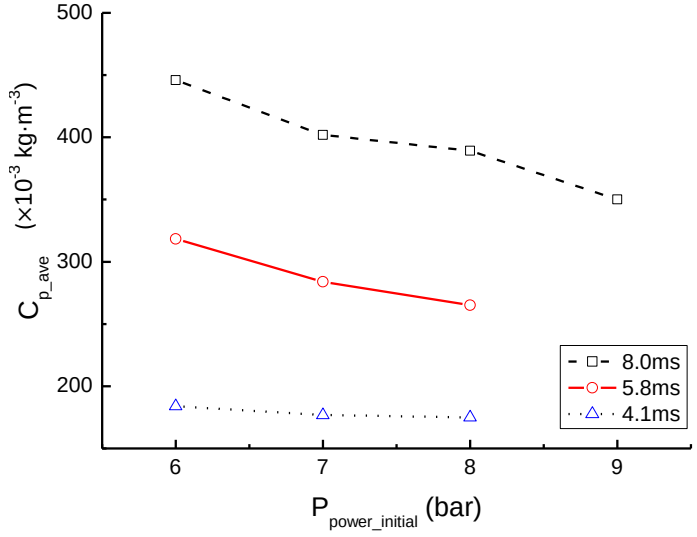

(a)

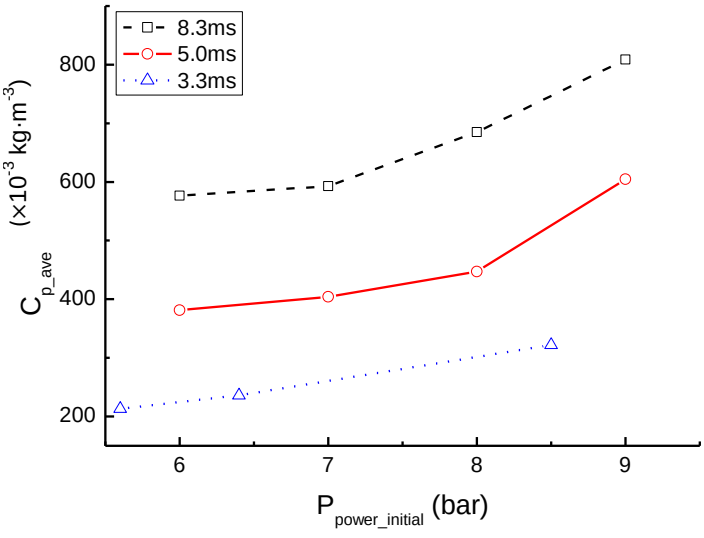

(b)

Figure 6.4 The average concentration of permeate (C_{p_ave}) with respect to initial feed pressure ($P_{power\_initial}$)and different feed concentration: (a) BW30-2540 membrane element, (b) XLE-2540 membrane element, in un-steady operation

The clear experimental evidence suggests that for either a steady or un-steady desalination process, the combined film/KS model, which suggests the solute is transported solely by diffusion, is applicable to BW membrane. On the other hand, the SK model which

combines both solute diffusion and convection is more suitable to describe salt transport in the XLE membrane element, especially at low solvent flux J_v. The weights of the diffusive and convective fluxes are mainly dependent on the hydraulic conditions, such as feed concentration, feed flow rate and operation pressure. However, for practical DesaLink applications, the concentration of feed solution is in the range of 3–10 kg·m^{-3} (3000–10000 ppm) during the pressurisation cycle, and the average permeate flux J_v is in the range of 2.3×10^{-6}–4.6×10^{-6} m·s^{-1} accordingly. From *Figure 6.3(a)*, it is seen that the observed salt rejection R_o within this J_v range is above 90% and remains almost constant, indicating the salt transport due to convective flux is very small and what follows is its diffusion-only characteristic. Moreover, small deviations in R_o caused by the different feed concentrations can be neglected. This simplification is plausibly supported by the work of Ghiu (Ghiu 2003), where it was found that the KS and SK models could be considered equivalent (the reflection coefficients σ_1 and σ_2 are unity) for membranes when the solute rejection ratio R_o was higher than 86%. Taking into account this argument as well as our experimental results, the combined film/KS model was considered as having minimal deficiencies and was therefore applied to describe the transport mechanism and determine the mass transfer coefficient for the XLE membrane element.

6.6.2. Mass transfer in continuous operation

According to the procedure described above, for the systems consisting of two different membrane elements, the vales of CP were calculated using *Eqs. (6.17), (6.8)* and *(6.2)* and presented in *Figure 6.5*. It clearly shows the CP value is reduced with a higher crossflow velocity u, which is in line with the theory. For the BW membrane, the CP value is lowered by 25 % from 1.6 to 1.3 in the crossflow rate range of 1.8×10^{-2} –11.5×10^{-2} m·s^{-1}. For the XLE membrane element, similar trends of CP values were found. The slightly larger CP values compared to the BW system can be explained by the larger permeate flux obtained with the XLE membrane element.

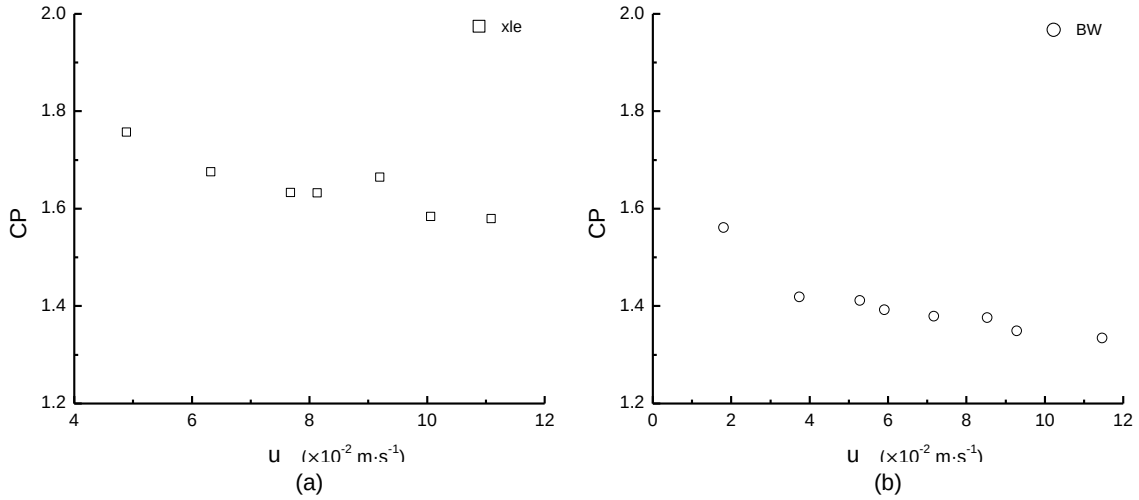

Figure 6.5 Calculated CP vales as a function of crossflow velocity (u): (a) BW30-2540 membrane element, (b) XLE-2540 membrane element.

Based on the obtained CP values and *Eq. (6.2)*, the corresponding mass transfer coefficients k were calculated. As summarized in *Figure 6.6*, in the crossflow velocity range investigated, there is a significant enhancement in the mass transfer coefficient k with increasing crossflow velocity u. The decreased CP values can be attributed to the increase of back-diffusive transport of the salt away from the membrane surface. From *Figure 6.6(a)*, it is clear that the mass transfer coefficients for the BW membrane element system were doubled, i.e. from 3.8×10^{-6} to 7.3×10^{-6} m·s^{-1}, in the crossflow velocity range of 2×10^{-2} – 12×10^{-2} m·s^{-1}. For the XLE membrane element system, which was operated in the crossflow velocity range of 5×10^{-2} – 12×10^{-2} m·s^{-1}, *Figure 6.6(b)* shows the mass transfer coefficients were increased by 40%, i.e. from 6.4×10^{-6} to 9×10^{-6} m·s^{-1}. In comparison to the BW membrane element system at the similar crossflow velocities, the slightly higher mass transfer coefficients for the XLE membrane element may be explained by the overestimation of the diffusive flux in the solute transport mechanism.

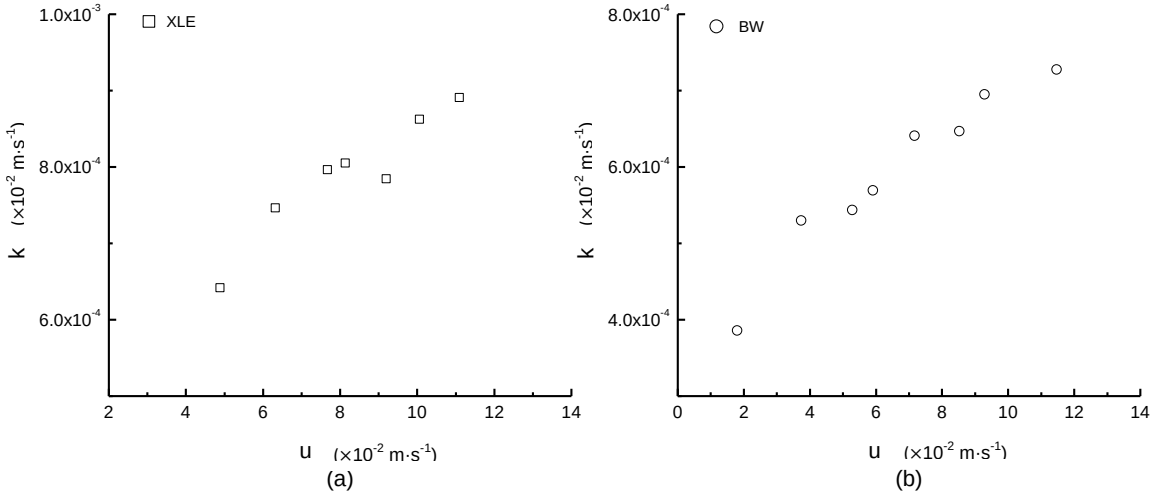

Figure 6.6 Effect of crossflow velocity (u) on mass transfer coefficient (k): (a) BW30-2540 membrane element, (b) XLE-2540 membrane element

Since the corresponding Reynolds numbers Re are less than 200, it can be assumed that the flow condition in both membrane elements is in principle a laminar flow. With the calculated Sherwood number Sh, Reynolds number Re and Schmidt number Sc, the relevant constants in *Eq. (6.14)*, namely a_{Sh}, α_{Sh} and β_{Sh}, were determined. Thus, the specific Sherwood correlations for both of the studied BW and XLE membrane elements were established. It needs to be noted that the feed flow channel of the two membrane elements were the same, in other words, the third term $(d_h/L)^{\gamma}$ in *Eq. (6.14)* was fixed. However, the channel geometry constraints were still included in the determination of the Sherwood correlations in order to generalize the correlation for other commercially available SWMs with different feed channel heights and lengths.

To fit the constants a_{Sh}, $\alpha_{Sh,}$ β_{Sh} and γ_{Sh} in *Eq. (6.14)* to the experimental data, a genetic algorithm (GA) (available in *Matlab*® toolbox) was used (programme code is shown in *Appendix B.2*) due to the non-linear feature of *Eq. (6.14)*. In brief, genetic algorithms, as differing from most classical, derivative-based optimization strategies, are heuristic search techniques inspired from the biological process of evolution by means of natural selection. GAs are efficient for function minimization in a complex search landscape with possibly strongly correlated adjustable parameters (Goldberg 1989). For the objective functions,

ordinary least-squares (OLS) estimation was first used to fit the data. Moreover, to guarantee the goodness of fit and diminish possible chance correlations between the fitted parameters, another approach, termed robust regression (RR), was also employed. This is because OLS can behave badly when the error distribution is not normal and the number of adjustable parameters is somewhat large relative to the number of data points to be modelled, whereas, RR is less vulnerable to unusual data points and can normally circumvent such problems. All fittings using either OLS or RR plausibly arrived at almost identical sets of parameters, which display a clear indication of the fitness of the resulting Sherwood correlations.

The experimentally determined relationship between the dimensionless numbers Sh and Re is shown in *Figure 6.7*, along with the corresponding prediction from the fitted correlation. With the constants optimised following the procedure described above, the Sherwood correlations can be rewritten as follows:

for BW30-2540 membrane element:

$$Sh_{BW} = 0.93 \cdot Re^{0.33} \cdot Sc^{0.34} \cdot \left(\frac{d_h}{L}\right)^{0.33} \tag{6.20}$$

for XLE-2540 membrane element:

$$Sh_{XLE} = 1.1 \cdot Re^{0.34} \cdot Sc^{0.34} \cdot \left(\frac{d_h}{L}\right)^{0.33} \tag{6.21}$$

A satisfactory reproduction of the experimental data was found using the fitted correlations, given as *Eqs. (6.20)* and *(6.21)*. This is clearly observable from: (1) the good agreement between the experimental and predicted data in terms of both the shape of the curve and the overlap of data points (*Figure 6.7)* and (2) the regression coefficients (R^2), as indication of the goodness of fit (*Figure 6.8)*.

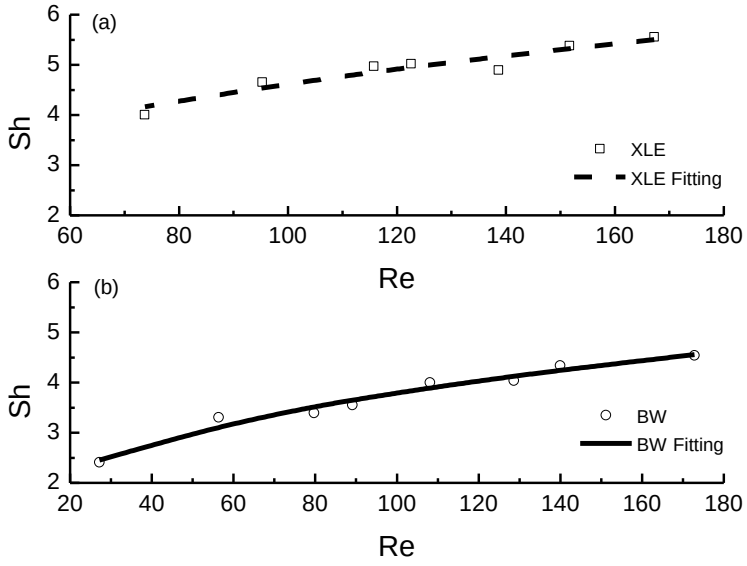

Figure 6.7 Experimental and fitted Sherwood numbers (Sh) with respect to Reynolds number (Re) at various crossflow velocities: (a) BW30-2540 membrane element, (b) XLE-2540 membrane element.

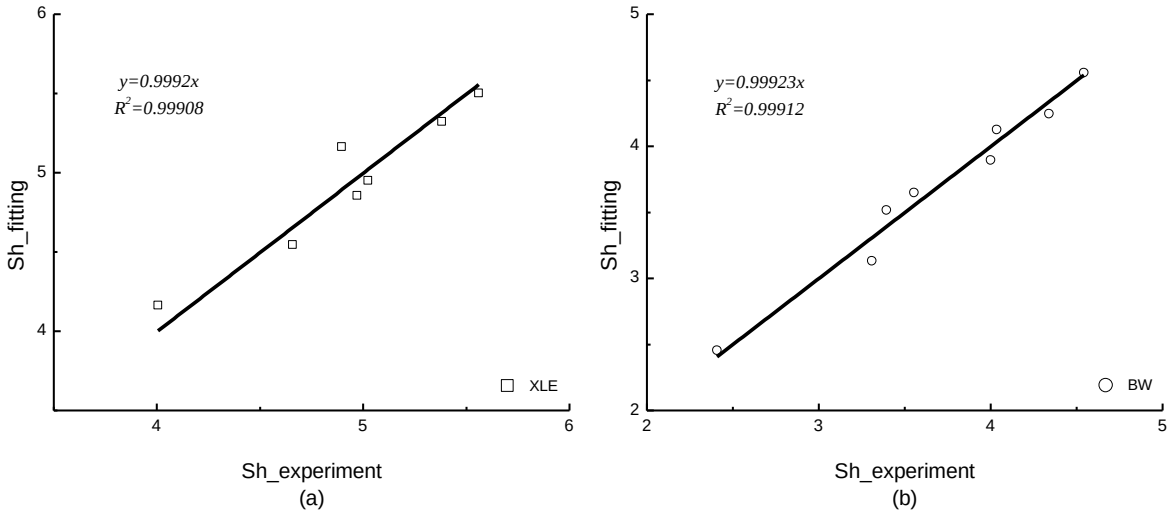

Figure 6.8 Comparison of fitted and experimental Sherwood numbers: (a) BW30-2540 membrane element, (b) XLE-2540 membrane element

Comparing *Eqs. (6.20)* and *(6.21)* for the BW and XLE membrane element system respectively, it should be noted that the constant (β_{sh}) relating to the Schmidt numbers (Sc) and the constant (γ_{sh}) relating to the channel geometry term (d_h/L) are the same in both equations. The Re related constants (α_{sh}) are very similar. There is a noticeable difference in

the constant a, suggesting that the difference between the two correlations is mainly due to the difference of the inlet zone of the membrane elements, as the hydrodynamic conditions used in all experiments, including the characteristics of feed solutions and channel geometries of each membrane element, were identical.

We can now proceed to assess the herein proposed Sherwood correlations by cross-examining them with four other models proposed in the literature (Bird and Stewart et al. 1960; Xuesong 1987; Hickey and Gooding 1994; Hickey and Gooding 1995), and further demonstrate their applicability as well as their improvements in describing the transport characteristics for the current systems.

The CP values were calculated using *Eq. (6.2)*, with the corresponding mass transfer coefficients k estimated from either our newly established Sherwood correlations *Eq. (6.18)* or the ones obtained by the literature models. We compared these calculated CP values with the experiments conducted in this work and the results are summarized in *Figure 6.9*, presented as a function of the crossflow velocity. While our model systematically demonstrates good reproduction of the experimental data, only qualitative agreement between the literature theoretical models and the experiments can be observed from *Figure 6.9*, i.e., a generally decreasing trend was predicted with the increasing crossflow velocity u. Interestingly, none of the three literature correlations was able to correctly capture the transport mechanisms in the systems. Despite being one of the most widely adopted models in membrane separation studies, the Bird correlation actually gave the worst prediction. The model proposed by Hickey and Gooding, which was developed based on the mass transport results from the various types of feed spacers for the SWM elements, also failed to show any significant improvement from Bird's model, with a 15% deviation from the experiments on average. Among them, the correlation from Wang (Xuesong 1987) gave a close match with the experimental CPF values; however, it is still noticeably less accurate than our model.

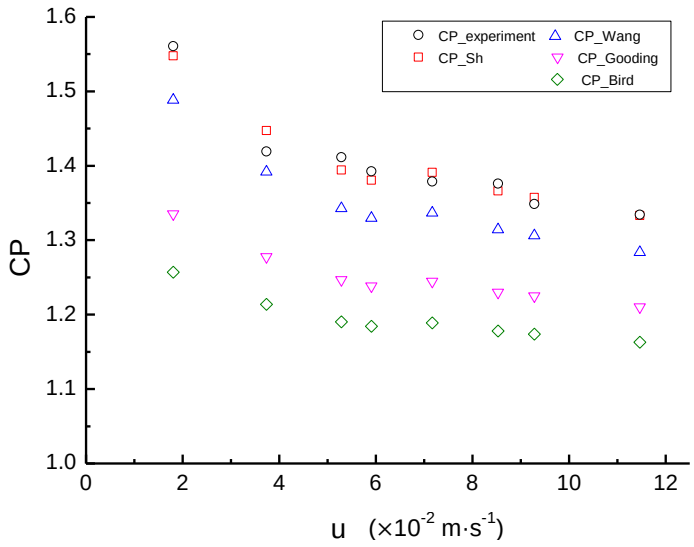

Figure 6.9 Comparison with CP values obtained from popular Sherwood correlations (XLE module only).

From the results presented in *Figure 6.9*, it needs to be emphasized that care must be taken when selecting the correlation models for specific RO systems. We find some of the commonly used correlations for fully developed laminar flows may not be used for the SWM RO elements investigated in this study, which is evidenced by their failure in correctly predicting the CP values. In contrast, our newly established Sherwood correlations showed semi-quantitative to quantitative agreement with the experiments over a wide range of crossflow velocities; thus, the accuracy and applicability of the Sherwood correlation were confirmed. It can be concluded that the Sherwood correlations established in this work for the BW30-2540 and XLE-2540 SWM elements can be used to determine the mass transfer coefficients for salt solutions in continuous operation processes with a satisfactory accuracy.

6.6.3. Mass transfer in batch mode operation

To acquire a comprehensive understanding of the mass transfer mechanisms in both steady and un-steady processes, DesaLink system was used to obtain mass transfer coefficients for the un-steady hydraulic states.

The feed flow rate is constantly varying during the DesaLink desalination operation. Thus, the experimental data from one pressurization process can instantly reveal the

relationship between the different feed flow and mass transfer coefficients. However, in order to build the relationship between the average feed and permeate flows (which was used in the modelling process), three different initial feed flow rates were tested (*Figure 6.10*). They were realized by adjusting the re-circulation pump rate with the feed concentration and initial feed power pressure being kept the same. It can be seen from the variation of the feed flow rate (*Figure 6.10*) that for each experimental set there were two obvious stages of power feeding (i.e. first on and then off, switched at the turning point of the curve).

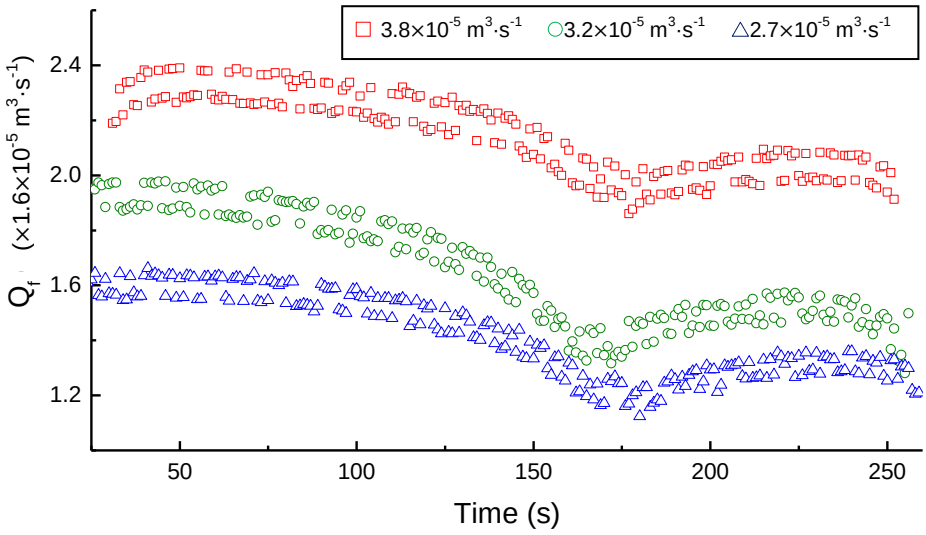

Figure 6.10 Instantaneous feed flow rates measured during the operations of DesaLink under different initial feed flow rate that corresponding to different re-circulation pump settings

The obtained permeate flows for the corresponding different feed flow rates are shown in *Figure 6.11*. Note that only the large and small feed flow rates are presented in *Figure 6.11* due to the small differences between the medium and small feed flow rates. Similar to the above observed changing of feed flow, all the permeate flows display a two-stage feature. As expected, the permeate flow was directly affected by the average feed flow rate.

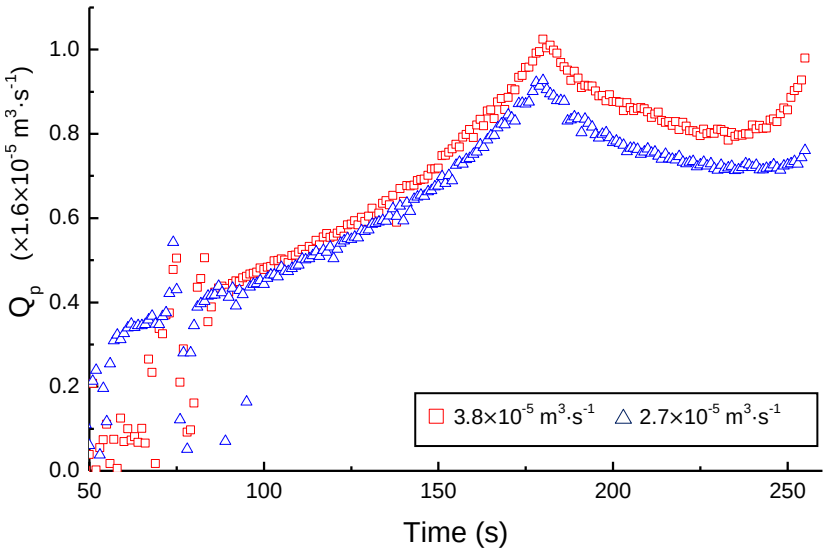

Figure 6.11 Permeate flow rate profiles for the two different feed flow rates (they are coloured according to Figure 6.10)

On the other hand, the permeate concentrations were almost the same for the different feed flow rates. This can be explained by the good salt rejection quality of the membrane elements used and their consistent performance for salt rejection under the varying feed pressure investigated here. Nevertheless, not only were the achieved amounts of permeate flow different, but the total salt passages were also variant under the various feed flow conditions, as shown in *Figure 6.12*.

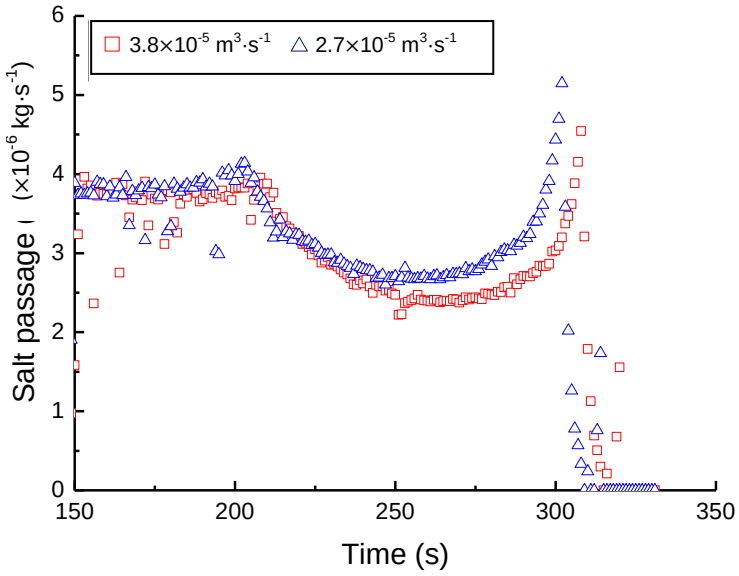

Figure 6.12 Concentration profiles for the permeate flows obtained at the different feed flow rates with respect to the operation time

Both *Figures 6.11* and *6.12* point to the fact that the permeate quality is dependent on the average feed flow rate. It is clear that the permeate flow rate is higher (meaning a larger volume of permeate) and the salt passage is reduced (meaning a lower concentration of permeate) when a larger flow rate is used. This is because large flow rates enhance the mass transfer coefficient and therefore reduce the CP. It thus emphasizes the need to construct suitable theoretical models which describe the relationship between flow rates and mass transfer coefficients in the un-steady hydraulic conditions. This would, in turn, allow for the quantification of the observed proportional change in permeate qualities, i.e. volume and concentration, against various average feed flow rate.

From previously introduced *Eq. (6.19)*, the relationship between $ln\left[J_v \cdot C_p/(C_b - C_p)\right]$ and $J_v/u^{\alpha_{Sh}}$ only becomes linear when parameter b is a constant, in other words, a constant feed flow concentration and the same hydraulic conditions are required. In all cases studied here, the bulk concentration kept increasing as can be seen from *Figure 6.13*, leading to a rising kinematic viscosity ν and a decreasing diffusion coefficient *D*. What follows is that the parameter b was no longer a constant, and therefore the graphical prediction was not suited in determining the mass transfer in RO-batch (un-steady) process.

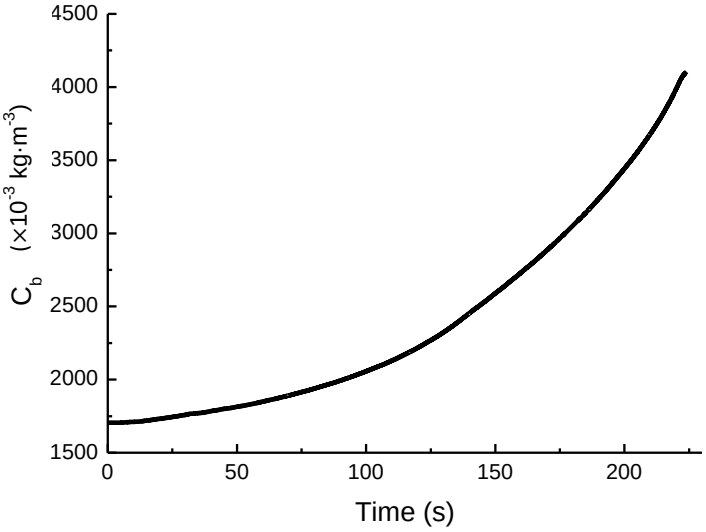

Figure 6.13 Representative increasing concentration of bulk solution

6.6.3.1. Linear fitting method

To overcome the problem that the graphical fitting method is not feasible because the parameter b is not kept constant during the batch-RO process, a linear graphical method was used at first. This method uses only a small part of the experimental data to realise the linear graphical fitting. For a small portion of the experimental data, the kinematic viscosity v and diffusion coefficient D of the feed solution can in principle be assumed constant, because their changes (0.2% in diffusion coefficient D for the concentration range of 200 – 3000×10^{-3} kg·m^{-3} and 0.15% in kinematic viscosity v) can be neglected when the change in concentration is small (from 200 to 3000 ppm). After selecting the range of experimental data (from 2000 ppm bulk solution to 3000 ppm bulk solution), *Figure 6.14* was produced to show the results from the linear fitting with the measured J_v, C_p, C_b, u, and the known value for α_{Sh} (which equals 0.33, as suggested by the previous theory).

From the fitting equation displayed on the figure, the intercept ($ln\, P_s$) of the straight line to the Y axis is 15.95, which gives the corresponding P_s as 1.18×10^{-7} m·s^{-1}. This P_s value exceeds by a factor of 2 the value provided by the manufacturer, which is 0.6×10^{-7} m·s^{-1}, reflecting a much larger than expected passage of salt through the membrane. It indicates

probably more salt passed through the membrane in the un-steady operation mode because of the instantly increasing feed pressures and feed concentrations.

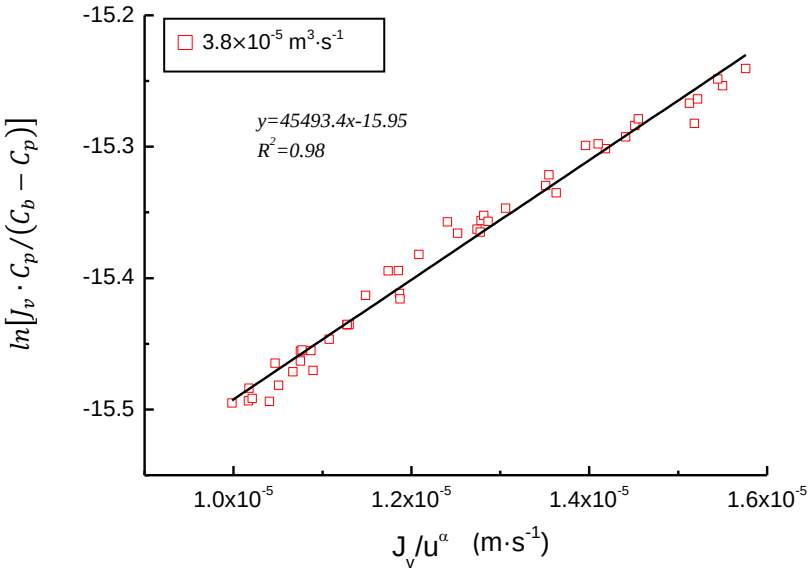

Figure 6.14 Data fitting for different feed flow rate

The values of parameters a_{sh} and β_{sh} were estimated based on the Sherwood correlation (*Eq. 6.14*). The Sherwood correlation is given as:

$$Sh = \frac{k \cdot d_h}{D} = 1.58 \cdot Re^{0.33} \cdot Sc^{0.34} \cdot \left(\frac{d_h}{L}\right)^{0.33} \qquad (6.22)$$

6.6.3.2. Non-linear method

The linear graphical method presented in the previous section has its limitation, i.e. the parameter α_{Sh} was pre-set to a value of 0.33, as suggested by the conventional correlation for a fully developed laminar flow. As described in *Section 6.1*, the feed channel spaces in the RO module create small turbulence regions where laminar flows cannot be fully developed in the feed channel. Therefore, taking 0.33 as the value for parameter α_{Sh} only can be a first approximation and the fitting procedure certainly needs to be refined. So, a non-linear GA method was adopted to estimate the Sherwood correlation. For the GA method, unlike the linear method, the varying parameter b in *Eq. (6.19)* is no longer a

limitation, allowing the correlation to be determined for the whole range of the experimental data.

The principles of the GA method have been introduced in *Section 6.5.1*. All the unknown parameters, namely a_{Sh}, α_{Sh}, β_{Sh} and γ_{Sh}, in *Eq. (6.19)* were estimated simultaneously by the GA implementation, yielding a very satisfactory regression coefficient R^2 (as shown in *Figure 6.15*). The thus obtained Sherwood correlation is given as:

$$Sh = \frac{k \cdot d_h}{D} = 2.09 \cdot Re^{0.26} \cdot Sc^{0.38} \cdot \left(\frac{d_h}{L}\right)^{0.33} \tag{6.23}$$

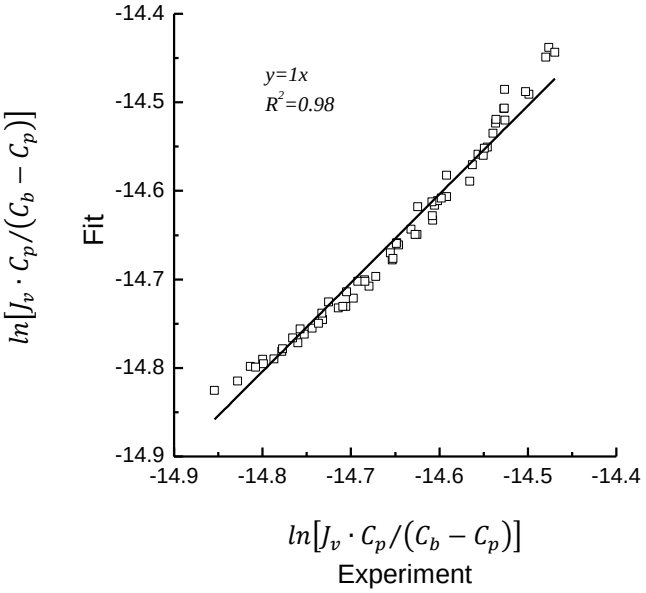

Figure 6.15 Comparison of the experimental with the predicted values based on the Sherwood correlation fitted by the GA method

Comparing *Eq. (6.23)* with *Eq. (6.22)*, the same value was, as expected, retained for parameter γ, since the same RO module used should give the same parameter for the (dh/L) term. However, it is found that the parameters α_{Sh}, β_{Sh}, and a_{Sh} in *Eq. (6.23)* are all different from those in *Eq. (6.22)*, most significantly being the values of parameter α_{Sh}. One should bear in mind that the value of 0.33 was suggested for parameter α_{Sh} in the literature primarily for a fully developed laminar flow. Evidenced from the good fitting to the experimental data

by *Eq. (6.23)* (where α_{Sh} is 0.26), it is conclusive that for an un-fully developed laminar flow in the SWM RO module, a new model (like *Eq. 6.23*) rather than the empirical Sherwood correlation (*Eq. (6.22)*) is needed to correctly characterise the system. So, the herein developed Sherwood correlation obtained by the GA fitting was chosen as the more appropriate and accurate correlation for an un-fully developed laminar flow in RO module.

Based on *Eq. (6.23)*, the mass transfer coefficients k were calculated and are shown in *Figure 6.16*. The obtained mass transfer coefficients k were plotted against the corresponding feed flow velocities, demonstrating a clear increase of the mass transfer coefficients k with increasing feed flow velocity u.

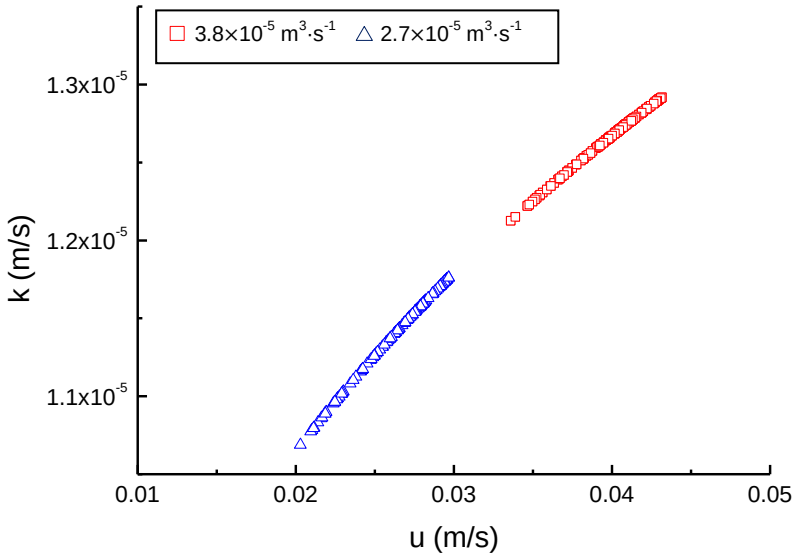

Figure 6.16 Variation of the mass transfer coefficient as a function of the feed flow velocity for the two cases of large and small feed flow rates

With the mass transfer coefficients k determined, the $CPFs$ were obtained based on *Eq. (6.2)*. The increasing CPF against time (*Figure 6.17*), was due to the increase of permeate flow rate and the decrease of feed flow rate along the time. At any given time point, the CPF was larger for the operation with the small feed flow rate, affirming again the large flow rates help to reduce the CP. This is also in line with the expectation from the Sherwood correlation (*Eq. (6.23)*).

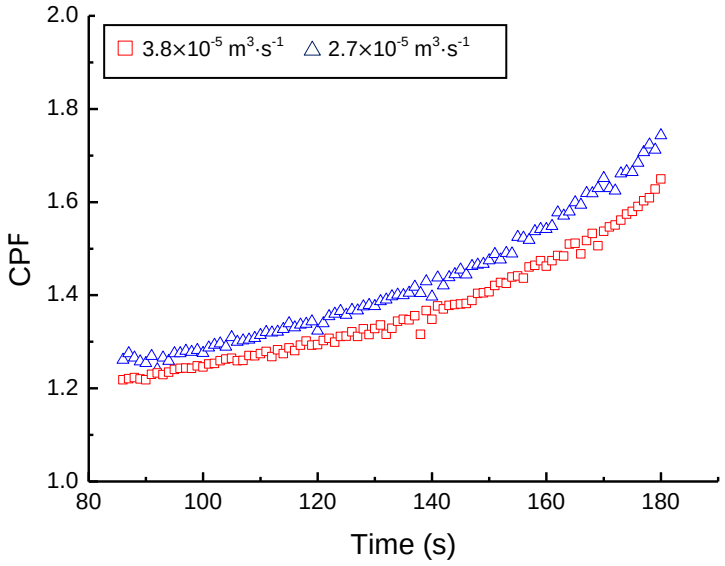

Figure 6.17 CP values obtained at the different feed flow rates with respect to the operation time

6.6.4. Related energy losses in DesaLink

As show in *Eq. (6.24)*, the ideal specific energy consumption (SEC_{ideal}), i.e. no CP related energy losses, of a batch-RO desalination process is related to the osmotic pressure of the feed solution $OsmP$ and the recovery ratio r:

$$SEC_{ideal} = \frac{OsmP}{r} \cdot ln\frac{1}{(1-r)} \qquad (6.24)$$

For a practical system, where CP is inevitable, the SEC increases proportionally to the CP factor, or CPF, because the $OsmP$ is enlarged proportionally by the CP. Furthermore, extra energy consumption occurs because of the use of the re-circulation pump. The amount of energy consumed by the re-circulation is related to the feed flow rate and operation time. Thus, the specific energy consumption SEC of the practical batch-RO desalination process is expressed as the sum of two terms:

$$\boldsymbol{SEC = CPF \cdot SEC_{ideal} + SEC_{pump}} \quad (6.25)$$

where CPF is the concentration polarization factor, SEC_{ideal} is the specific energy consumption without concentration polarization, and SEC_{pump} is the specific energy consumption of the re-circulation pump. The CPF can be quantified based on *Eq. (6.2)* and the newly established Sherwood correlation, *Eq. (6.23)*. SEC_{ideal} is calculated based on *Eq. (6.24)*. The energy consumption of the pump is assumed to increase linearly with the feed flow rate. With the known volume of permeate, which equals the volume of the water cylinder, and permeate flux, the SEC_{pump} is given as follows:

$$\boldsymbol{SEC_{pump} = \frac{f(u) \cdot t}{V_p} = \frac{f(u) \cdot \frac{V_{water}}{Q_p}}{V_{water}} = \frac{f(u)}{Q_p}} \quad (6.26)$$

where V_p is the volume of permeate water (L), which equals the volume of the water cylinder V_{water} (L), and t is the operation time (s), which equals the volume of water cylinder divided by the rate of permeate flow Q_p.

The parameters of Q_p and feed concentration C_f were selected according to the DesaLink operation range. In light of the DesaLink test results, the values for Q_p and C_f were chosen to be 0.6 l/min and 8000 ppm, respectively. And the energy needed by the re-circulation pump, which is a function of the feed flow rate, was decided according to the pump test results. In *Eq. (6.25)*, the first term, $CPF \cdot SEC_{ideal}$, decreases with the feed flow rate u exponentially. The second term, SEC_{pump}, increases with u lineally. Therefore, there exists an optimum point at which the minimum SEC is achieved. *Figure 6.18* thus illustrates the changes of the $CPF \cdot SEC_{ideal}$, SEC_{pump} and their sum respectively, and a value of 2 l/min for feed flow rate can be identified graphically to yield the optimum SEC.

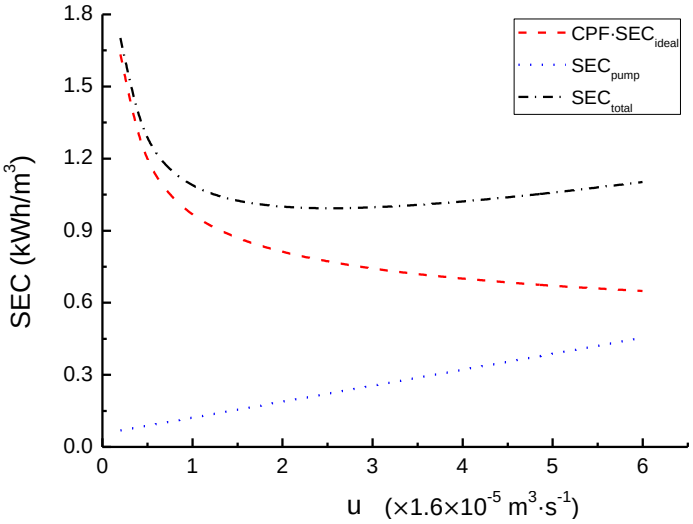

Figure 6.18 Energy consumptions against different feed flow rates

6.7. Summary

A thorough examination of CP, a central phenomenon in membrane based separation, was carried out. To control this deleterious phenomenon, it is necessary to estimate the effect of hydrodynamic parameters on the mass transfer coefficient characterizing a specific RO configuration. With the understanding of the mass transfer in different membrane types, the specific Sherwood correlations (for both steady and un-steady operations) were obtained according to the appropriate mass transport theories. The herein proposed Sherwood correlation was fully validated by the experimental observations, indicating possible applications to SWM ROs with different geometrical properties. The optimum re-circulation rate for DesaLink operation was investigated based on the specific mass transport characterization in the SWM RO module. One cannot rule out the possibility that the optimum feed flow rate determined here may lead to a lesser performance for other steady RO operations, thus limiting its wider applicability. It was, nevertheless, satisfactory in the scope of this work. Furthermore, with the established Sherwood correlation, we were able to evaluate the $CPFs$ under the different feed flow rates and to quantify the total volume and concentration of the permeate, which could be easily implemented in the system model eventually.

Chapter 7

EXPERIMENTAL RESULTS AND MODELLING OF WHOLE SYSTEM

This chapter presents a description for each of the subsystems of DesaLink and proposes mathematical models for characterizing their performances. A description of the modelling methodology and procedure adopted is given. The subsystem models are then integrated into a complete DesaLink model. With the aim of modelling the performance of DesaLink with a high accuracy, the complete model is refined by reference to the laboratory tests. Validation of the final proposed model is performed using further experimental results. The modelling architecture of the whole DesaLink system is described and performance predictions are discussed.

7.1. Introduction

To assess DesaLink in the scope of practical application, various site-specific operation conditions, e.g. feed water concentration, were considered. Given a large number of operation variables and an even larger number of possible combinations among them, experiments were used together with theory to arrive at a general model which could be used to predict performance for a range of designs and operating conditions.

To complete an empirical model of DesaLink that predicts its performance reliably and accurately, the preliminary models of the critical subsystems (linkage and RO subsystems) were constructed based on established physical theories. Then these models were verified by experimental data from DesaLink tests. The dependence between the variables observed in the physical models was used as a guideline to the development of the model functions. The models were modified by using the Matlab/Simulink environment, which

allowed great flexibility in the programming due to its inherent modularity. Thus, individual models could be improved, replaced or moved within the system model. The modelling procedure (for model development) is introduced in the following section.

The DesaLink tests were specifically designed to obtain the characteristic of the subsystems, especially the RO subsystem, for non steady-state input (e.g. varying feed concentration, feed pressure) and output (e.g. varying permeate concentrations and flow rates). All conditions (mainly concerning different concentrations of the feed water and different feed power pressures) under which DesaLink was expected to operate were considered in the model development. The results from the experiment conducted with 4500 ppm salt solution and 9 barg initial feed air were initially used to determine model parameters. Experimental results obtained with a wider range of feed concentration and air pressures were used later to exam the robustness and reliability of the DesaLink model.

7.2. Modelling method

As mentioned, the experimental results obtained from the DesaLink characterisation work were used to create empirical models by fitting the data to polynomial functions. The fitting procedure is realised by using 'Linear in the parameters Multiple Regression' method in Mathworks®, Matlab®. It method fits the data points to a predefined non-linear relationship, through least-squares error minimization. The coefficients in the non-linear fitting equations were calculated by using Matlab's backslash operator. For instance, to establish the relationship between an output variable y, which depended on two input variables, x_1 and x_2, the following non-linear model is defined:

$$\mathrm{y}(\mathrm{x}_1, \mathrm{x}_2) = K_1 + K_2 \cdot \mathrm{x}_1 + K_3 \cdot \mathrm{x}_2 + K_4 \cdot \mathrm{x}_1 \cdot \mathrm{x}_2 \qquad (7.1)$$

Note that in *Eq. (7.1)* a new variable $x_1 \cdot x_2$ (denoted as x_3 hereafter) was generated to effectively represent the desirable non-linear term. Thus the target model matrix $x=[1, x_1, x_2, x_3]$ is produced. The coefficients vector $K=[K_1, K_2, K_3, K_4]$, which leads to the minimized error

between both sides of *Eq. (7.1)*, is calculated with the backslash arithmetic operator in Matlab, i.e., $K=x\backslash y$. As *Eq. (7.1)* shows, by using this modelling procedure, we can consider the effects of more than one variable on any other variable.

Having discussed the fitting method used, we now turn to another important aspect to a good data fitting, which is selecting appropriate basis functions for constructing the mathematical expression. Instead of using the more conventional polynomial functions, i.e. *Eq. (7.1)*, the Hermite polynomials, *Eq. (7.2)*, were adopted. The Hermite polynomials are a classical orthogonal polynomial sequence and consist of $He_0(x)$, $He_1(x)$, $He_2(x)$, etc, as shown below:

$$\mathrm{y}(\mathrm{x}_1,\mathrm{x}_2) = \mathrm{He}_0(x_1) + \mathrm{He}_0 \cdot (\mathrm{x}_2) + \mathrm{He}_1(\mathrm{x}_1) + \mathrm{He}_1(\mathrm{x}_2) + \cdots + \mathrm{He}_\mathrm{n}(\mathrm{x}_1) + \mathrm{He}_\mathrm{n}(\mathrm{x}_2) \tag{7.2}$$

The representation of $He_0(x)$, $He_1(x)$, etc are shown in *Appendix D.1*. To elaborate on the use of this particular polynomial, we shall consider that having once assumed the interpolating behaviour of the discrete, tabular entries (experimental data) can be represented by a polynomial (i.e., not a physical model), the problem is reduced to choosing an appropriate functional form and determining the corresponding coefficients. More often than not, the polynomial is taken to be something similar to *Eq. (7.2)* and any difficulties in fitting the data are offset by means of increasing the order of the polynomial. Apart from possible failures of even using very high orders in reproducing the data, this 'dangerous' procedure very often can lead to ambiguous results. It is recommended instead to use some interpolative function that allows the fitting to be achieved with lower order terms, thereby producing a more reasonable result. To this end, orthogonal polynomials, such as the Hermite polynomials, are better suited.

In general, it is desirable to correlate the experimental observables with the independent variables using a physically intuitive model. However, the aforementioned cure-fitting procedure adopted a different approach where different pre-defined non-linear

relationships were subjected to data fitting and suitability check. Therefore, the so-generated models based on the prediction of the actual physical relationships can be an accurate mathematical expression that correctly reproduces the experimental observables from the inputs, which is of more importance to build the whole model.

7.3. Linkage subsystem

The linkage system of DesaLink plays a key role in the batch-RO desalination process. Its specific design allows pressure and power to be transferred to feed water in an energetically efficient manner, which was explained in detail in *Chapter 3*. Here, on the basis of the known linkage system geometry (*Figure 7.1* and *Table 7.1*), calculation of the theoretical transferred force and pressure of the power and pump cylinders are discussed.

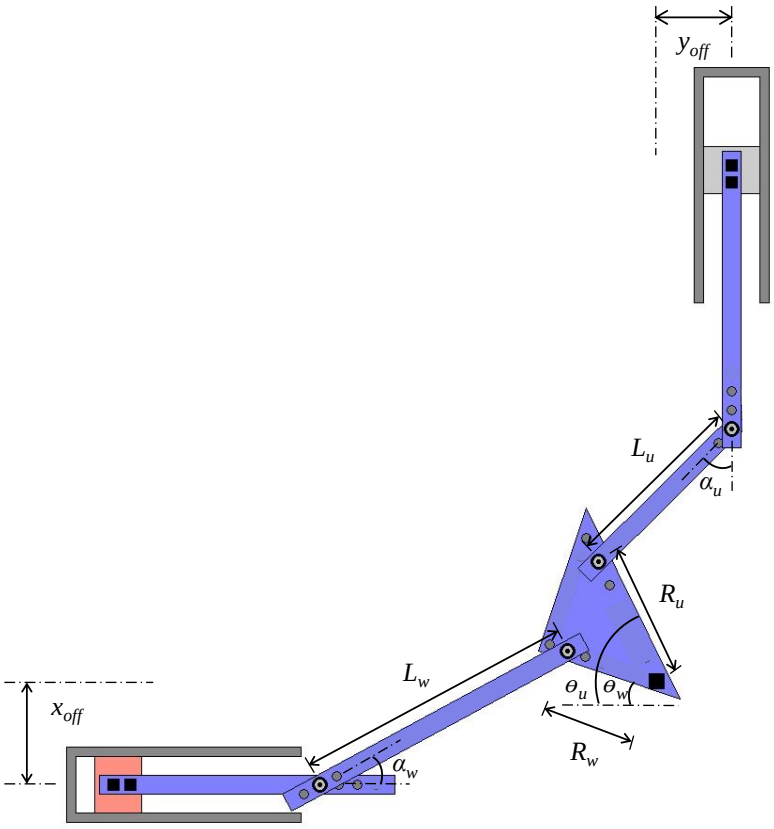

Figure 7.1 The schematic of DesaLink linkage subsystem

Table 7.1 The geometric details of the constructed DesaLink

Power cylinder	L_w (m)	$\alpha_{w\_min} - \alpha_{w\_max}$ (º)	R_w (m)	$\Theta_{w\_min} - \Theta_{w\_max}$ (º)	x_{off} (m)	A_{air} (m^2)	L_{air} (m)
	0.76	22 – 40	0.25	0 – 55	0.28	0.035	0.23
Pump cylinder	L_u (m)	$\alpha_{u\_min} - \alpha_{u\_max}$ (º)	R_u (m)	$\Theta_{u\_min} - \Theta_{u\_max}$ (º)	y_{off} (m)	A_{water} (m^2)	L_{water} (m)
	0.5	64 – 16	0.35	45 – 100	0.2	0.0087	0.35

7.3.1. Power pressure

With the input variables as listed in *Table 7.1* known (the volume of air compressor V_{comp} is 0.051 m^3), the power pressure through the filling and expansion processes were determined based on *Eqs. (7.3)* and *(7.4)*, respectively. A value of 0.994 for the polytropic index n was found to yield the best fitting to the measured power pressure values (*Figure 7.2)*.

$$\mathbf{P_{air\_1} V_{air\_1}}^{\boldsymbol{n}} = \mathbf{P_{air\_2} V_{air\_2}}^{\boldsymbol{n}} \quad (7.3)$$

$$\mathbf{P_{air} V_{air}}^{\mathbf{n}} = \mathbf{c} \quad (7.4)$$

where P is the pressure, V is the volume, n is the polytropic index, and c is a constant.

The model-predicted feed power pressure is in good agreement with the experimental observables (*Figure 7.2*). It is worth pointing out that the time variable shown as the horizontal axis in *Figure 7.2* is an intermediate variable, and was not used as an input for modelling. It is intended to depict the variation of the specific variable during the process, and its use in the following figures in the Chapter bears the same purpose hereafter.

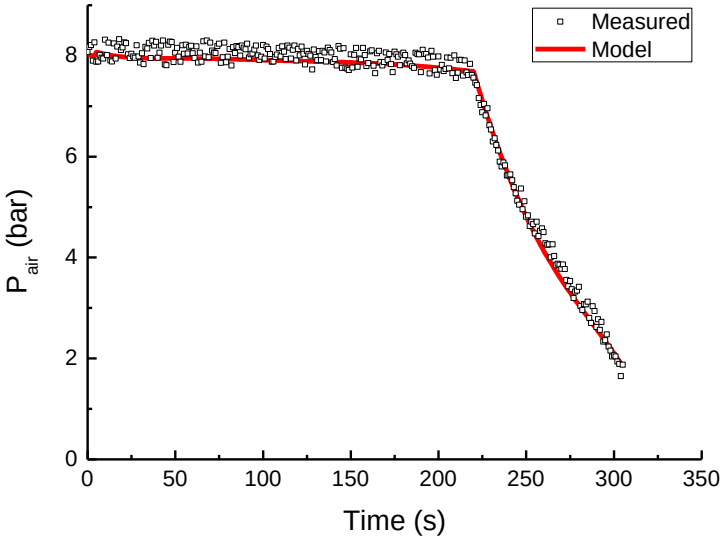

Figure 7.2 Measured and model (Eqs.7.3 and 7.4) predicted feed power pressures

7.3.2. Pump piston displacement

The water piston displacement can be straightforwardly and accurately calculated from the power piston displacement, based on simple trigonometry of the linkage mechanism, which is explained in *Eqs. (7.5)–(7.9)*. The calculated water piston displacements in comparison to the corresponding experimental values are displayed in *Figure 7.3*. The mathematical model was specially designed to issue predictions of pump piston displacement starting from a relatively steady state of the DesaLink operation — experimental data generated in the initial air feed-in operation were not considered in model development. The reason is that at the beginning of feeding air to DesaLink, spontaneous movements of the power and pump pistons cannot be satisfactorily described by the physical theory, which is evident in *Figure 7.3*. That is, whereas the fitted model yields very good agreement with all experimental data points beyond a power piston displacement of 2.5×10^{-2} m, the first measurement taken at the start of the operation clearly deviates from the model-predicted changing trend. A good prediction of these initial spontaneous movements caused by stiack in the joints of DesaLink is, however, of little importance in characterizing the system performance and hence can be excluded from consideration when constructing the model.

$$\theta_{u\_step} = \theta_{w\_step} + \mathbf{45} \tag{7.5}$$

$$\boldsymbol{\alpha}_{w\_step} = \mathbf{sin}^{-1}\left(\boldsymbol{R}_w \cdot \mathbf{sin}\,\theta_{w\_step} + \boldsymbol{x}_{off}\right)/\boldsymbol{L}_w \tag{7.6}$$

$$\boldsymbol{\alpha}_{u\_step} = \mathbf{sin}^{-1}\left(\boldsymbol{R}_u \cdot \mathbf{cos}\,\theta_{u\_step} + \boldsymbol{y}_{off}\right)/\boldsymbol{L}_u \tag{7.7}$$

$$\boldsymbol{d}_{power\_pistion} = (\boldsymbol{R}_w \cdot \mathbf{cos}\,\theta_{w\_min} + \boldsymbol{L}_w \cdot \mathbf{cos}\,\boldsymbol{\alpha}_{w\_min}) - (\boldsymbol{R}_w \cdot \mathbf{cos}\,\theta_{w\_step} + \boldsymbol{L}_w \cdot \mathbf{cos}\,\boldsymbol{\alpha}_{w\_step}) \tag{7.8}$$

$$\boldsymbol{d}_{water\_piston} = (\boldsymbol{R}_u \cdot \mathbf{sin}\,\theta_{u\_max} + \boldsymbol{L}_u \cdot \mathbf{cos}\,\boldsymbol{\alpha}_{u\_min}) - (\boldsymbol{R}_u \cdot \mathbf{sin}\,\theta_{u\_step} + \boldsymbol{L}_u \cdot \mathbf{cos}\,\boldsymbol{\alpha}_{u\_step}) \tag{7.9}$$

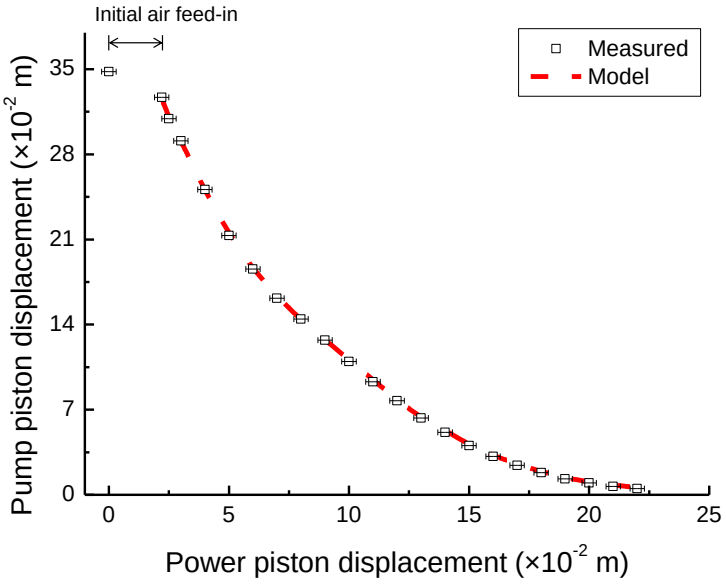

Figure 7.3 Measured and model predicted water piston displacement

7.3.3. Water pressure

The water pressure (P_{water}) can be predicted on the basis of the following trigonometric equations:

$$\mathbf{F_{power}} = \mathbf{P_{power}} \cdot \mathbf{A_{power}} \tag{7.10}$$

$$\mathbf{T_w} = \mathbf{F_{power}} \cdot (\mathbf{R_w} \cdot \mathbf{sin}\,\theta_w) + (\mathbf{F_{power}} \cdot \mathbf{tan}\,\alpha_w) \cdot (\mathbf{R_w} \cdot \mathbf{cos}\,\theta_w) \tag{7.11}$$

$$\mathbf{T_w = T_u = F_{water} \cdot (R_u \cdot \cos\theta_u) + (F_{water} \cdot \tan\alpha_u) \cdot (R_u \cdot \sin\theta_u)} \quad (7.12)$$

$$\mathbf{F_{water} = T_w/(R_u \cdot \cos\theta_u + R_u \cdot \sin\theta_u \cdot \tan\alpha_u)} \quad (7.13)$$

$$\mathbf{P_{water} = F_{water}/A_{water}} \quad (7.14)$$

Compared to the measured values of P_{water} (*Figure 7.4)*, it first can be confirmed that the water pressure rose with the water piston moving towards its end during the operation and the theoretical model correctly predicted the overall profile of such changes. However, it is also obvious that the experimental observations are systematically below the model prediction. This discrepancy is not surprising, and can be explained by the energy losses due to the sliding frictions of both pistons and the linkage bearing frictions, which were not taken into account in the theoretical model, i.e. *Eqs. (7.10)–(7.14)*.

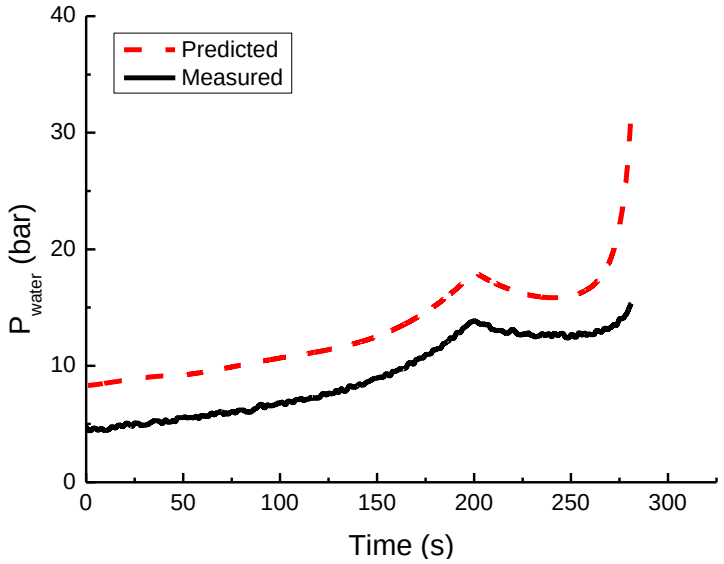

Figure 7.4 Theory (Eqs. 7.10–7.14) predicted and measured water pressure

A close inspection on *Figure 7.4* further reveals that the experimentally-measured P_{water}-*Time* curve may be quantitatively reproduced by applying a scaling factor to the original model predictions. Both simulated and experimental curves have similar shapes, indicating the chosen theory is able to capture the underlying mechanism at work. The over estimation from the model may be partly attributed to the experimental operation being non-ideal,

providing an argument for adopting a scaling factor which in effect represents the efficiency of the system. Given the complexity of DesaLink, it is difficult to quantify the associated energy losses by a single physical theory or by a combination of several ones. Not only is scaling factor (i.e. efficiency factor η) an effective means to augment the applicability of the theory to modelling DesaLink, but it also can be considered to be physically motivated. Such means ensure that the well-established theoretical model remains unaltered, while achieving an adequate description of the specific system of interest. Moreover, the efficiency factor can be either a constant or an expression. The latter can facilitate a better reproduction of a 'difficult' curve compared to the former; therefore the energy efficiency factor (η) was chosen to be a polynomial expression, which was then determined by matching the original predicted curve to the experimental one (*Figure 7.4*). The mathematical model (*Eq. 7.15*) was formulated by considering the following variables: theoretically predicted water pressure (P_{water_theory}) and the efficiency factor (η). The efficiency factor has an expression as *Eq. (7.16)*. Note that *Eq. (7.16)* involves only two experimental observables: the angle of the air cylinder crank (Θ_w) and the angle of the air cylinder connecting rod (α_w), and they can be determined unambiguously based on the system geometry during the operation. The efficiency factor (η) is expressed by a third-degree polynomial and takes the form of a function of dimensionless variable (Θ_w/α_w), with the coefficients fitted by reference to the experimental data. The new model (*Eqs. 7.15* and *7.16*) simulates water pressure in good agreement with the experiment for the whole course of the operation (*Figure 7.5*). The multiple regression method introduced in *Section 7.2* was again used to obtain the coefficients involved in *Eq. (7.16)*.

$$\boldsymbol{P_{water} = P_{water\_theory} \cdot \eta} \tag{7.15}$$

$$\boldsymbol{\eta = 10.95 - 22.5 \cdot (\Theta_w/\alpha_w) + 9.8 \cdot (\Theta_w/\alpha_w)^2 - 5.96 \cdot (\Theta_w/\alpha_w)^3} \tag{7.16}$$

The use of a dimensionless variable (Θ_w/α_w) in *Eq. (7.16)* allows for prediction and hence comparison of the energy losses of different system configurations without introducing

biases from the beginning. To demonstrate this, *Eqs. (7.15)* and *(7.16)* were used to estimate the water pressure for the DesaLink with a new configuration (increasing crank radius R_w and R_u by 0.05 m), and the result is satisfied (*Figures 7.6* and *7.7*).

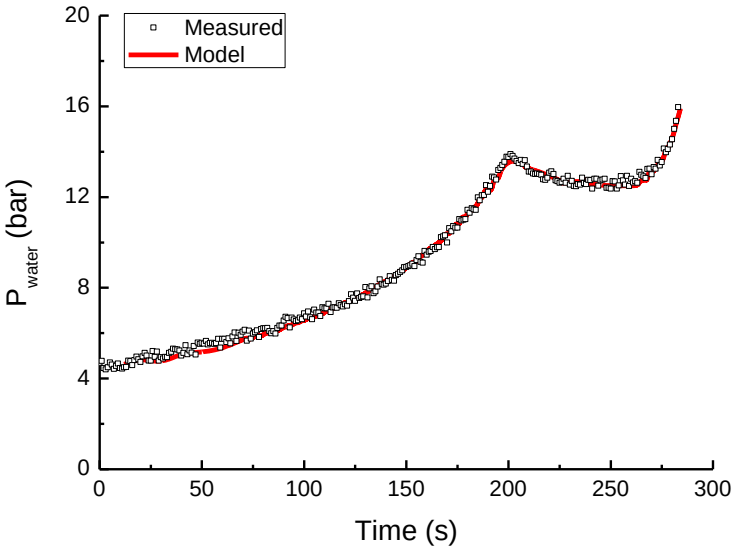

Figure 7.5 Measured and model estimated water pressure

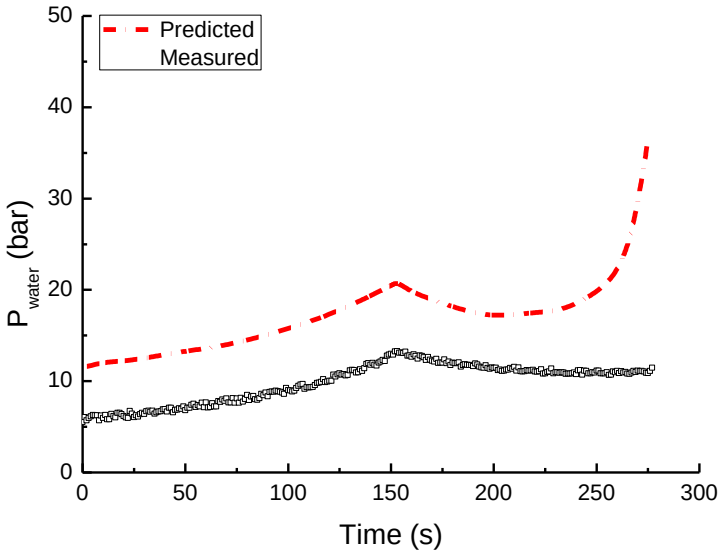

Figure 7.6 Theory (Eqs. 7.10–7.14) predicted and measured water pressure for system with new configuration

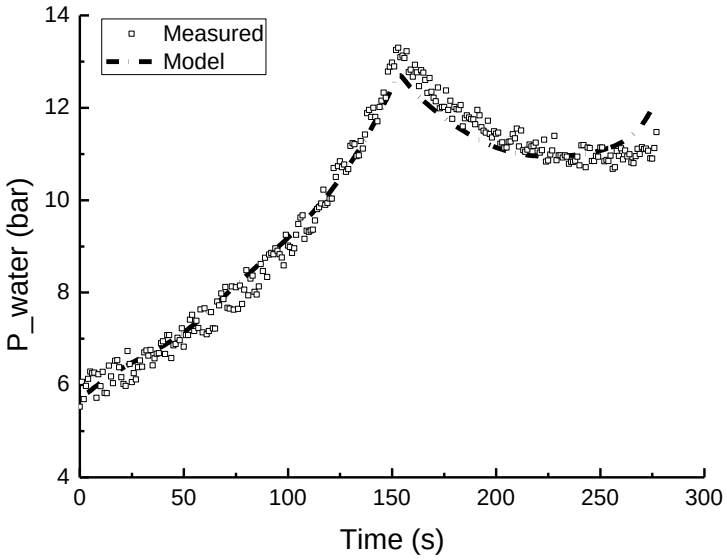

Figure 7.7 Measured and model estimated water pressure for system with new configuration

7.4. RO subsystem

This section focuses on the development of a theoretical model to be used in the prediction of the performance of the batch-RO subsystem. The detailed information about the RO module was introduced in *Section 3.5*.

7.4.1. Theoretical model

Individual RO element performances, e.g. flow rate and concentration of the permeate, can be determined according to the formulations introduced in *Section 6.2.2*.

The permeate flow rate is defined by:

$$\mathrm{Q_p} = \mathrm{J_v} \cdot \mathrm{A_{mem}} = \mathrm{L_p} \cdot (\Delta P - \Delta OsmP) \cdot \mathrm{A_{mem}} \qquad (7.17)$$

where A_{mem} is the membrane area (m^2); L_p is the intrinsic membrane permeability ($m^3/m^2 \cdot s \cdot Pa$), i.e., pure water permeability; ΔP is the operating pressure (Pa); and $\Delta OsmP$ is the difference in the osmotic pressure across the membrane (Pa), which equals to $OsmP_{water} - OsmP_p$.

Eq. (7.18) defines calculation of the concentration of the solute in the product stream:

$$\mathrm{C_p} = \mathrm{P_s} \cdot (\mathrm{CPF} \cdot \mathrm{C_f} - \mathrm{C_p}) \cdot \frac{\mathrm{A_{mem}}}{\mathrm{Q_p}} \quad (7.18)$$

where P_s is the salt permeability coefficient (m/s), which characterizes solute transport through the membrane; C_f and C_p are the feed solution concentration and the permeate flow concentration, respectively; and CPF is the polarization factor. As discussed in *Chapter 6*, the expression of CPF obtained in the batch-mode RO (*Eqs. 6.2* and *6.23*) was adopted to estimate the CPF in order to ensure an accurate and specific prediction for the un-steady batch-RO process.

During the initial modelling stage, the standard theory stated above (i.e. *Eqs. 7.17 and 7.18*) was considered, since it has been widely used for RO system design (commercial RO modelling packages, such as ROSA) and evaluation. However, we have found the theory, i.e. *Eqs. (7.17)* and *(7.18)* cannot be utilized to predict the performance of DesaLink (*Appendix D.2*). This is because the feed water pressure and concentration are constantly changing during the batch-mode process; furthermore, within the DesaLink design, the permeate flow rate and concentration (system outputs) have marked effects on the operation pressure and feed flow (system inputs), making the whole system too complex to be modelled by any simple linear regression to the steady mode relationships (*Eqs. 7.17–7.18*). Thus, new models were established as discussed below.

7.4.2. Product flow rate model

The theoretical osmotic pressure of the feed water ($OsmP_{water}$) along the process can be calculated (as shown in *Figure 7.8*) based on salt mass balance with the input variables: concentration of the initial feed water $C_{f\_initial}$ and displacement of water piston d_{water}.

$$\boldsymbol{OsmP_{water\_ini} = MR_{gas}T/V_{water\_ini}} \quad (7.19)$$

$$\boldsymbol{V_{water\_step} = d_{water} \cdot A_{water}} \quad (7.20)$$

$$\boldsymbol{OsmP_{water} = OsmP_{water\_ini} \cdot V_{water\_ini}/V_{water\_step}} \quad (7.21)$$

where $OsmP_{water}$ is the osmotic pressure of feed water during the process (bar); M is the molarity of the solute (mol); R_{gas} is the gas constant, equal to 8.314 $m^3 \cdot Pa \cdot mol^{-1} \cdot K^{-1}$; T is the absolute temperature (K); V_{water_ini} is the initial volume of feed water (m^3); and d_{water} is the displacement of water piston (m).

The net driving pressure P_{net} i.e. ($\Delta P - \Delta OsmP$) is then calculated by subtracting the osmotic pressure $OsmP_{water}$ of the feed water from the water pressure P_{water} (of which calculation details are given in *Section 7.3.2*). The achieved P_{net} is depicted in *Figure 7.9*. With the net driving pressure known, the permeate flow rates Q_p were calculated based on *Eq. (7.17)*. The predicted Q_p curve (*Figure 7.10*) has an almost identical shape to that of the predicted net driving pressure (*Figure 7.9*), a direct result of *Eq. (7.17)* as used in the calculations being a linear relationship. However, comparing the experimental and predicted Q_p profiles in *Figure 7.10*, it can thus be re-affirmed that the batch-RO operation of DesaLink cannot be adequately described by simple linear relationships and needs a more sophisticated model.

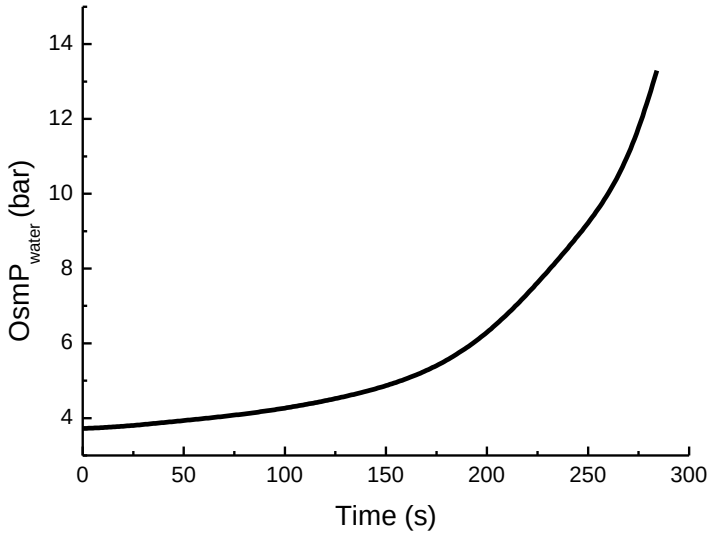

Figure 7.8 Predicted osmotic pressure of feed solution

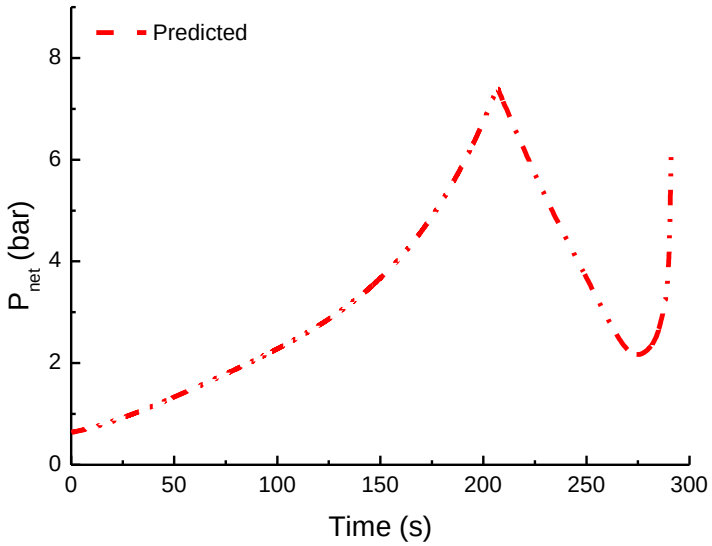

Figure 7.9 Predicted net driving pressure

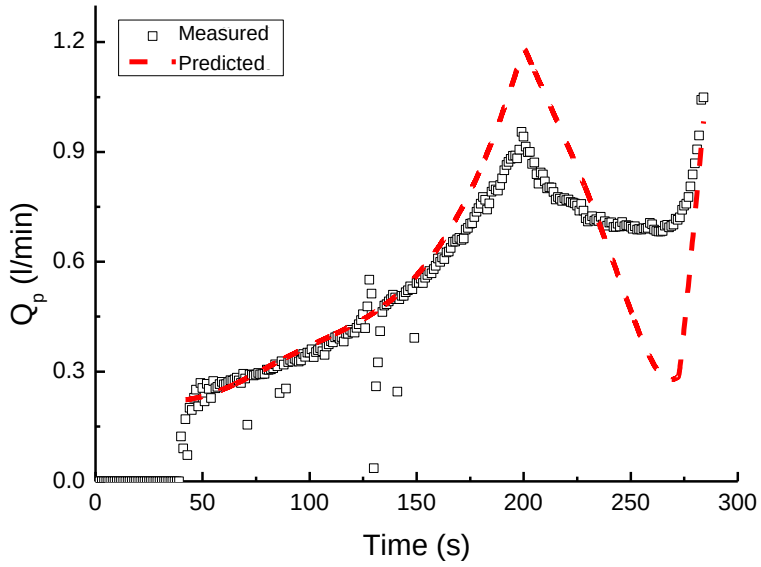

Figure 7.10 Measured and predicted permeate flow rates

To build the new model, a polynomial expression was used to correlate the output Q_p using the input variables which related to the output. These arguments were chosen based on physical insights. That is, the permeate flow rate Q_p depends on the net driving pressure P_{net}, which is related to the feed flow rate Q_f, feed water pressure P_{water} and osmotic pressure of feed water $OsmP_{water}$ which depends on feed concentration C_f. The resulting model is given by *Eq. (7.22)*. It is noteworthy that the fitted coefficients for the input variables are of the same magnitude, suggesting these physical attributes are important in determining the

output Q_p. This in turn points to the fact that modelling product flow rate under instantly-changing batch-mode operation conditions is not a simple task and relationships between variables are far from obvious. In particular, when an extensive operating range needs to be described by a unified model, a complex, physically motivated mathematical expression, such as *Eq. (7.22)*, may be better suited for the task than some more generic models.

$$\begin{aligned} Q_p &= f(Q_{p\_theory}) + f(P_{water}) \\ &= 4.8 - 10.6 \cdot Q_{p\_theory} + 8.2 \cdot {Q_{p\_theory}}^2 - 2.8 \\ &\cdot {Q_{p\_theory}}^3 + 22.3 \cdot P_{water} - 10.3 \cdot {P_{water}}^2 \\ &+ 5.5 \cdot {P_{water}}^3 \end{aligned} \tag{7.22}$$

where the Q_{p_theory} is the permeate flow rate given by *Eq. 7.17*, as show in *Figure 7.10 (red dash line)*. From *Figure 7.11*, it can be confirmed that the developed model (*Eq. 7.22*) is able to yield a good prediction of the permeate flow rate over the whole operation.

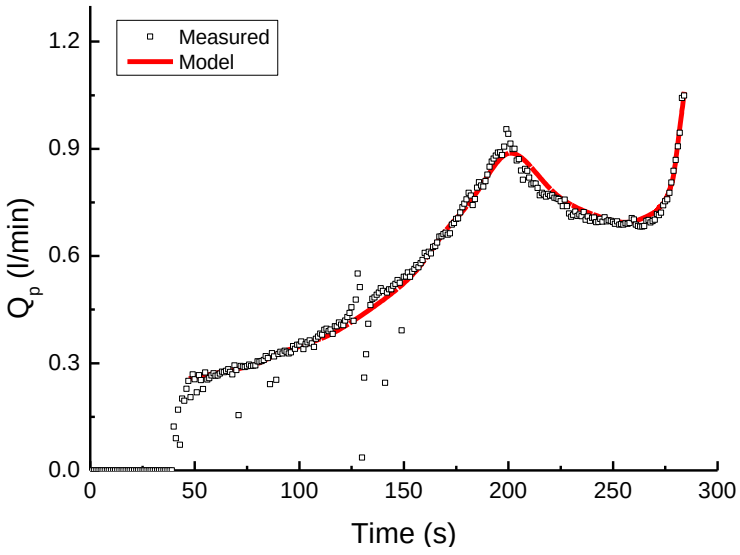

Figure 7.11 Measured product flow vs. model estimated product flow

7.4.3. Product concentration model

Another important factor to evaluate the RO process is the permeate concentration. To illustrate the need of a new model for the unsteady batch-RO operation of DesaLink,

Figure 7.12 was plotted for the permeate concentration C_p obtained from both experiments and calculations based on *Eq. (7.18)*. Not surprisingly, the discrepancies between the experimental and predicted values are very large and, more importantly, the shape of the experimental curve cannot be captured by *Eq. (7.18)*.

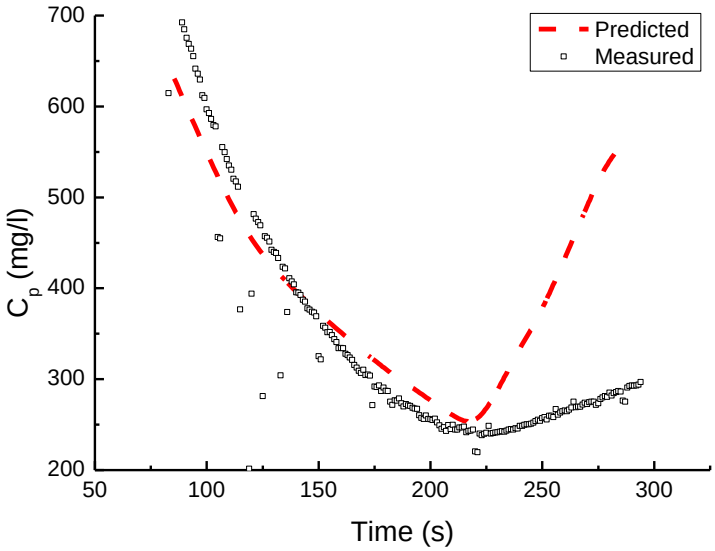

Figure 7.12 Theory predicted and measured permeate concentration

The mass transfer theory discussed in *Chapter 6*, which describes the salt concentration in the permeate stream, suggests that the salt passage is related to the feed flow concentration (C_f) and to the permeate flow rate (Q_p). This was used to guide the building of a new C_p model:

$$\begin{aligned} C_p &= f\left(C_{p\_theory}\right) + f\left(C_f, Q_p\right) \\ &= 10^3 \times (-0.16 + 0.68 \cdot C_{p\_theory} + 0.43 \cdot {C_{p\_theory}}^2 + 0.2 \\ &\cdot {C_{p\_theory}}^3 - 3 \cdot Q_P + 1.5 \cdot {Q_P}^2 - 0.7 \cdot {Q_P}^3 + 3.4 \cdot C_f - 2.2 \\ &\cdot {C_f}^2 + 0.73 \cdot {C_f}^3 \end{aligned} \tag{7.23}$$

where C_f is the concentration of feed flow (m^3/s); and C_{p_theory} is the theoretically (*Eq. 7.18*) predicted permeate concentration, as shown in *Figure 7.12 (red dash line)*.

The mass flow-rate of passes salt, which equals permeate concentration (C_p) × permeate flow rate (Q_p), was chosen as the indicator of interest in this case. Comparison between the measured and model-determined salt passage is depicted in *Figure 7.13*. On the whole, the agreement between the measured and estimated values is satisfactory. Notably, a number of experimental data points are outliers to the curve given by the model (*Eq. 7.23*). It should be emphasized that the primary aim of the model is not to 'match' every experimental point but to predict correctly the general trend of the amount of passed salt evolution against time.

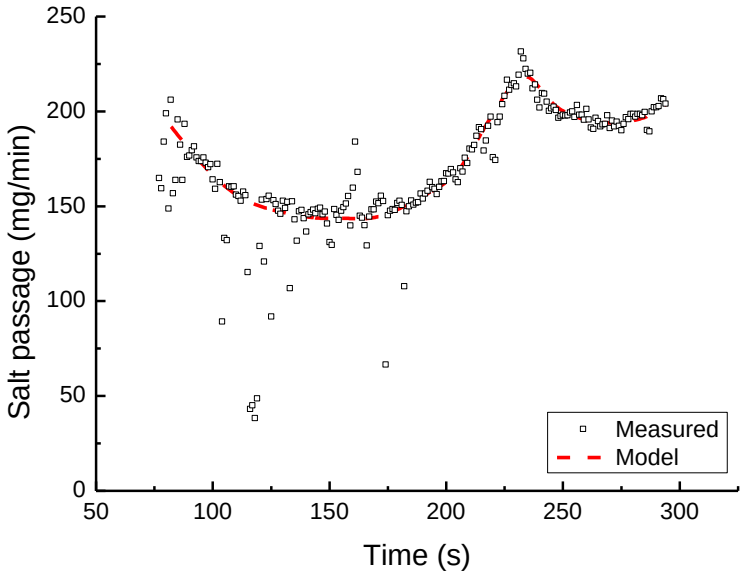

Figure 7.13 Measured and model estimated salt passage

7.5. DesaLink model

A complete DesaLink model was built in the Matlab/Simulink environment by integrating the individual models describing the corresponding subsystems. The approach adopted to interconnect the inputs and outputs of the DesaLink model is shown in *Figure 7.14*. Input attributes to the DesaLink model are the initial pressure of the feed air and concentration of the feed solution. The known linkage geometry (linkage lengths and connecting angles), membrane characteristics (e.g. membrane area and water permeability) together with the operation time were used as the intermediate variables. Note that the use

of operation time as an intermediate variable is in accordance with the implemented 'time' function in Simulink and, more importantly, was intended to better illustrate system performance during the whole operation. Finally, the permeate volume (V_p) and concentration (C_p) were obtained directly from the simulation, while the recovery ratio (*r*) and efficiency (*η*) of DesaLink, which are of primary interest, were calculated subsequently from the simulation results.

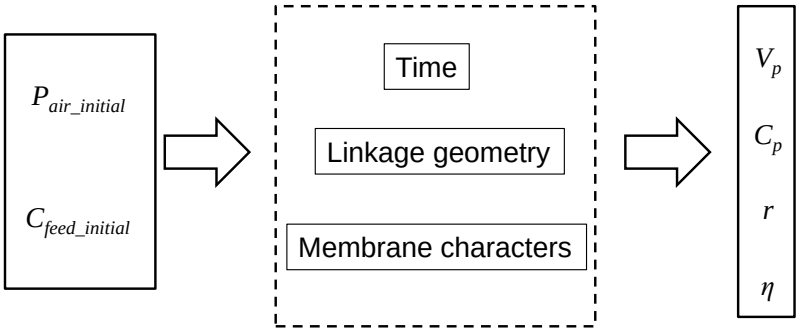

Figure 7.14 Inputs and outputs of DesaLink

The top layer of the complete DesaLink model hierarchy is shown in *Figure 7.15*. The established subsystem models described in previous sections were implemented as appropriate blocks in the complete model. Starting from the top-left of *Figure 7.15*, the information concerning the initial pressure of feed air and air piston displacement is supplied to the Feed Air Pressure block to derive the instantaneous air pressure. Meanwhile, the displacement of air power piston is fed to the Water pump Piston Displacement block and Water Pressure block, where calculation of the displacement of water piston and water pressure is done, respectively. These signals are used in the Theoretical Water Pressure block to calculate the theoretical water pressure at every step. Corresponding water pressure efficiency at every step is modelled in the Water Pressure Efficiency block which is based on *Eq. (7.16)*. The true water pressure in response to the feed air pressure is then determined by multiplying the pressure loss efficiency and the theoretical water pressure, as described in *Eq. (7.15)*. Finally, the water pressure and the membrane characteristics are used in the RO

block to calculate the product flow (Q_p) and its concentration (C_p). The Performance block calculates the overall recovery ratio (r) and system efficiency (η) accordingly.

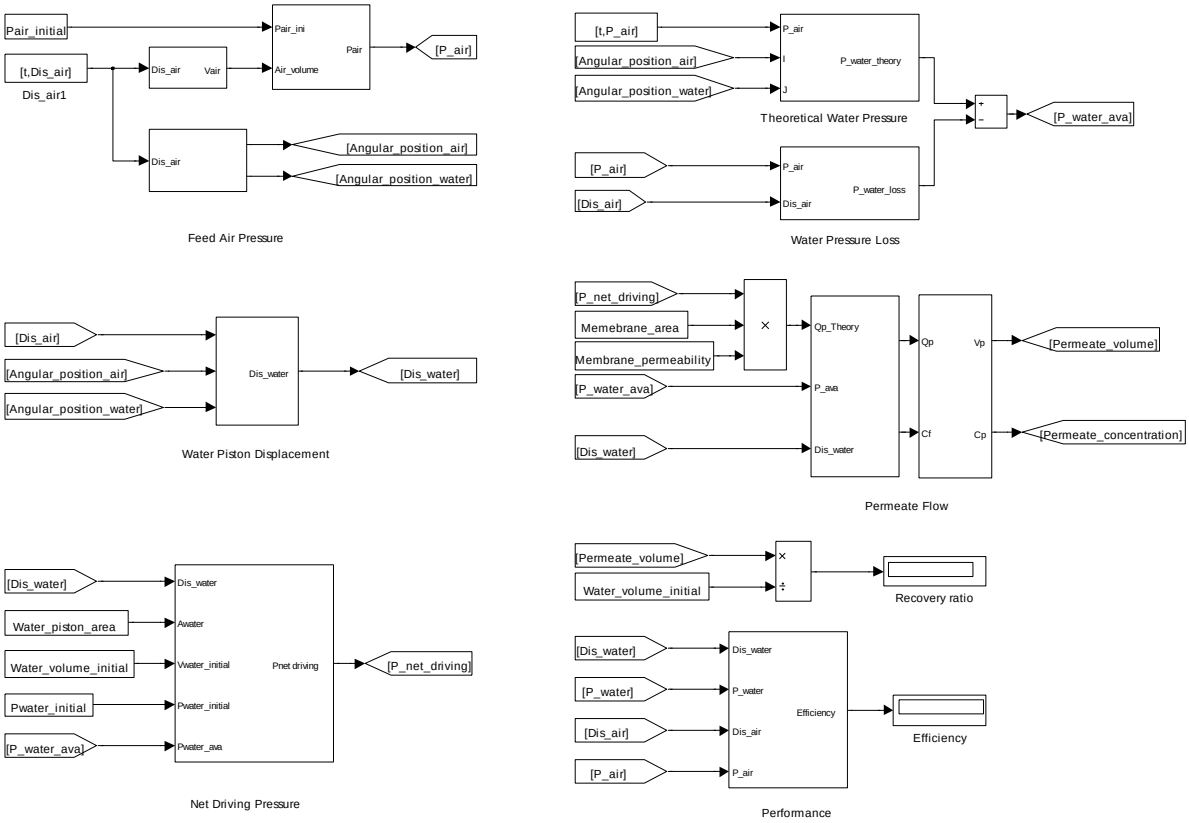

Figure 7.15 Top layer of the hierarchical Simulink model of DesaLink

7.6. Model refinement

Feed water of different concentration and feed air of different pressure were considered when refining the DesaLink model. Simulations examining the various operating conditions were conducted by using compressed air in the range of 6.5–9 barg and salt solutions in the range of 2000–4000 ppm.

7.6.1. RO feed water pressure

Experiments using about 3000 ppm feed water and 7 barg feed air were conducted using the procedure described in *Section 4.4*. After that, the simulation run was devised in a way that the simulated power piston movement followed the same displacement pattern against time as the experiment. The experimental (Measured) and simulated (Model) feed air

pressure along the process are compared in *Figure 7.16*. The agreement between the experimental and simulated values is good, demonstrating the effectiveness of the model in predicting the compressed air expansion along the whole operation. Experiments using feed air of 6.5 and 8 barg (and the same 3000 ppm feed water) were carried out to further verify the model. Again, the good agreement between the experiments and model predictions can be observed in *Figure 7.16*, clearly confirming the accuracy of the model. In DesaLink, the air pressure is decided by the displacement of the air piston which is in turn affected by how fast the permeate flows out of the RO subsystem. That is, a higher initial feed air pressure drives a faster permeate flow, leading to a faster air expansion process as can be seen from the associated earlier initiation of significant pressure drop in *Figure 7.16*. Based on these experimental results, the air expansion processes (during the operation) for the feed air of different pressure are predicted by adding a time function based on the initial feed air pressure to the previously derived air expansion model. Moreover, the similar shape of the expansion curves for compressed air of different pressure (*Figure 7.16*) indicates a consistent expansion of the compressed and dry air.

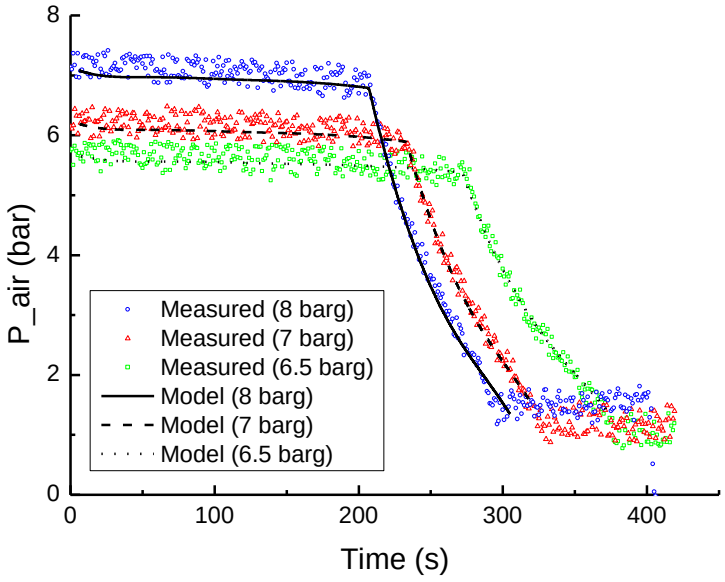

Figure 7.16 Feed air pressure using feed water of 3000 ppm

Combining the above model, which gives the air pressure during expansion for a given initial feed air pressure, with the corrected water pressure model accounting for pressure loss, the achieved water pressures can be determined and are compared with the corresponding experimental values in *Figure 7.17*. It is shown that the simulations yielded good prediction of the water pressure at all the three initial feed air pressures.

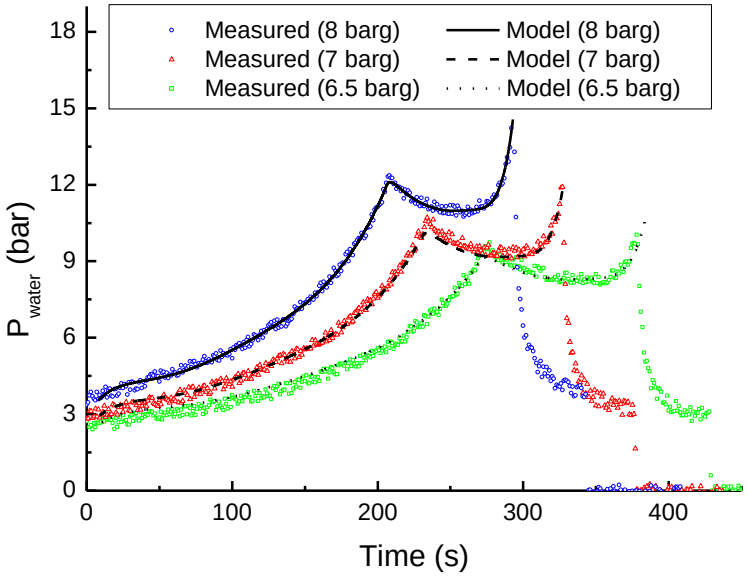

Figure 7.17 Feed water pressures using feed water of 3000 ppm

7.6.2. Permeate flow rate

The permeate flow rates were also accurately (within an average accuracy of more than 90%) predicted by the simulations for the three initial feed air pressures (*Figure 7.18*). From *Figures 7.17* and *7.18*, It can be seen that the permeate flow rates (Q_p) has a similar profile to that of the corresponding feed water pressure (P_{water}). Moreover, the permeate flow rate responds immediately to the change of feed water pressure, i.e. the permeate flow rate rises with the increasing feed water pressure, and reaches the maximum value when the feed water pressure achieves the maximum. Therefore, there is no necessity to set a response function for permeate flow rate in the model, because the permeate flow rate can be determined directly from the corresponding feed water pressure at the same time point.

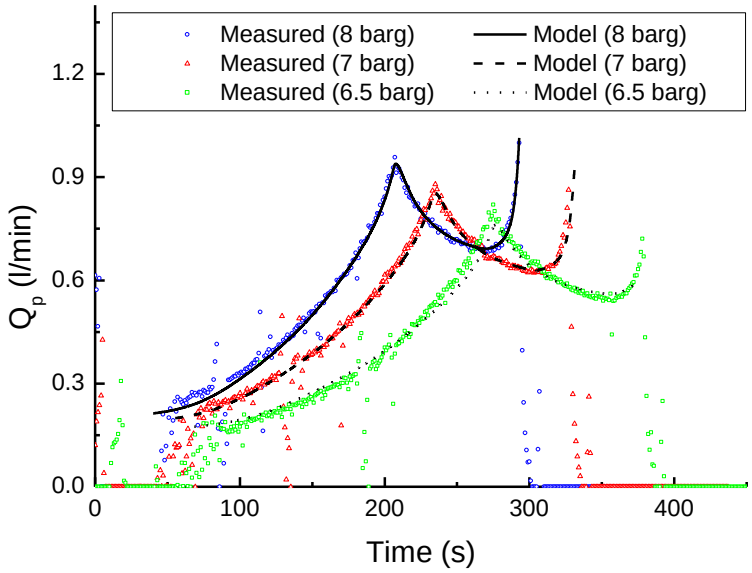

Figure 7.18 Permeate flow rates using feed water of 3000 ppm

Moreover, as shown in *Figure 7.18*, the produced permeate flow during the initial period of operation (t < 60s) was too small to be detected by the permeate flow rate sensor. As the water pressure rises progressively, more permeate passed through the membrane, accumulating a measurable amount of flow. Therefore, a threshold value of 0.2 l/min was set for permeate flow rate in the DesaLink model. This means that calculation of the total amount of permeate was done for all instantaneous permeate flow exceeding 0.2 l/min.

7.6.3. Permeate concentration

Permeate concentrations were recorded during the experiments with the three initial feed air pressures (feed water of 3000 ppm was used) and compared with model predictions in *Figure 7.19*. It is clear that the experimentally observed evolution of permeate concentration was correctly captured by the model for all three cases. However, the difference between the measured and modelled permeate concentrations is noticeably larger than that of the other outputs, e.g. permeate flow rate. It is difficult to attribute these discrepancies to any single reason. Nevertheless, a closer inspection provided a conceivable explanation and further suggested limitations of and possible future improvements for the current model. Permeate concentration is modelled based on the knowledge of feed flow rate, operation pressure and feed concentration. The situation is complicated by the fact that

these three inputs are mutually influenced by the output permeate, which in turn is dependent on the membrane characteristics. It should be noted that the model adopted for the RO block here was originally developed on the basis of the experiments when the membranes were brand-new. According to the manufacturer, variations of ±15% in membrane performance can be expected between individual modules and the performance of one particular membrane can deteriorate considerably with use. Such big variations in RO membrane characteristics were thus considered the most likely source of errors. Furthermore, other variables that are not considered explicitly in the model (such as feed water temperature) could also have a role to play, albeit to a significantly lesser extent. Although inclusion of more variables may improve the prediction, the current model can nevertheless yield accurate enough predictions of the permeate concentration.

It is worth mentioning that the measurements of permeate flow concentration at the start and finish of the process are of very small values, i.e. around 50 ppm. That is because the permeate flow is too small to fill the 7 mm connection tube to reach the concentration sensor, resulting in the sensor measuring air-mixed flows and, therefore, inaccurate readings.

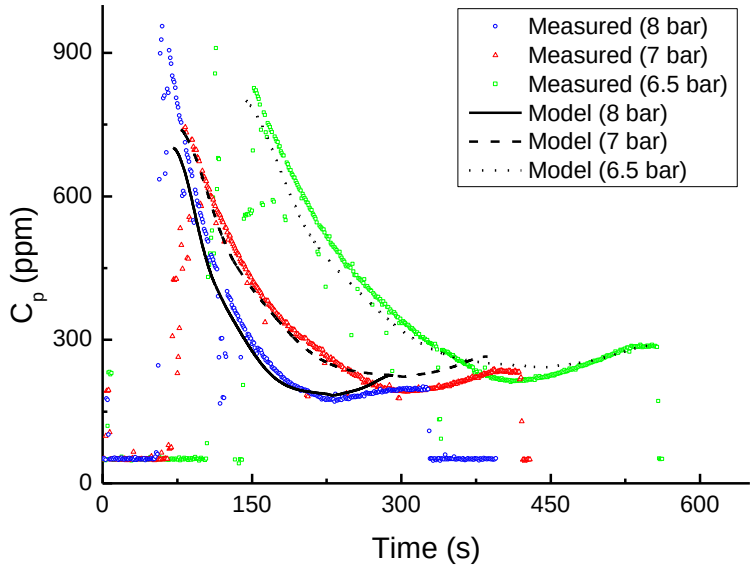

Figure 7.19 Permeate concentrations using feed water of 3000 ppm.

7.7. Model validation

In order to validate the developed model, additional experiments (that were not included in the above model development) using feed water of about 4500 ppm were carried out with initial feed pressures of 7 and 8 barg. Simulations were accordingly performed under the same conditions and the results were compared with the experimental measurements (collected using DesaLink) for feed air pressure, feed water pressure, and permeate flow rate and concentration. A particular focus was put on the feed water with a concentration of around 4500 ppm, which is the upper-limit concentration value of the brackish water.

It is shown in *Figures 7.20* and *7.21* that the agreement between the experimental and simulated values of both feed air pressure and feed water pressure is very good (within an average accuracy of 85%) for both initial feed air pressures. This demonstrates the effectiveness and accuracy of the models in describing the compressed air expansion and the pressure gained by feed water. More important is that the models have shown to exhibit a degree of transferability, i.e. the models are generally applicable for different initial feed air pressures and different feed water concentrations.

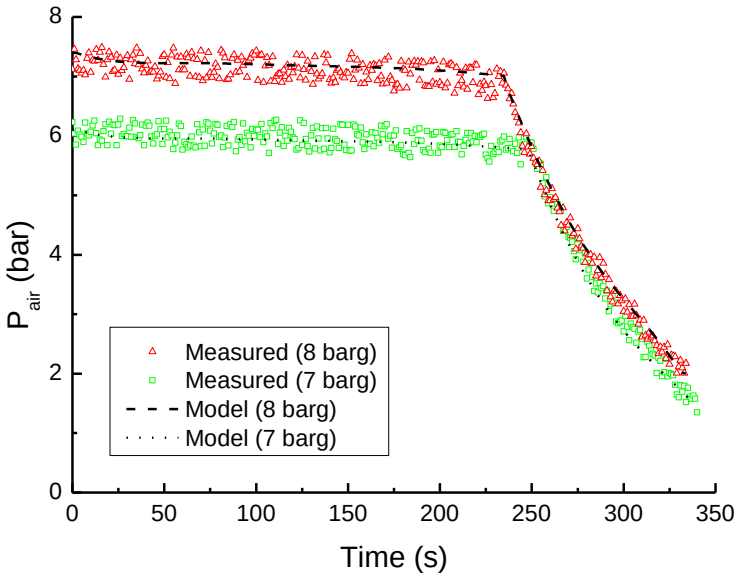

Figure 7.20 Feed air pressure using feed water of 4500 ppm

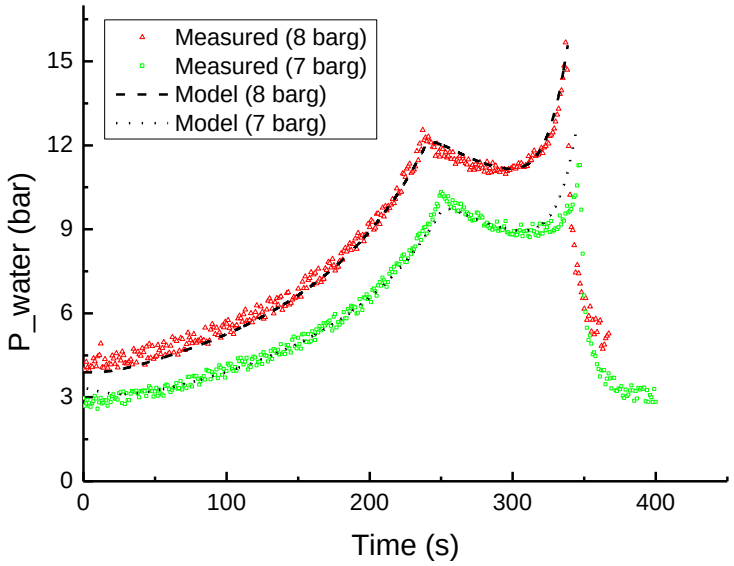

Figure 7.21 Feed water pressures using feed water of 4500 ppm

Experimental and simulated outputs, i.e. permeate flow rate and concentration, are compared for both initial feed air pressures in *Figures 7.22* and *7.23*, respectively. First, the predictions of permeate flow rate are in good agreement with the experiments, whereas the model could only qualitatively capture the changes of permeate concentration during the operation. Second, regardless of the less quantitative predictions of permeate concentration the model can be considered a valid tool for studying this property. This is because from *Figures 7.19* and *7.23*, it is clear that the model can predict correctly the different evolution profiles of permeate concentration, thus allowing a correct evaluation and comparison of the system performance for various operation conditions.

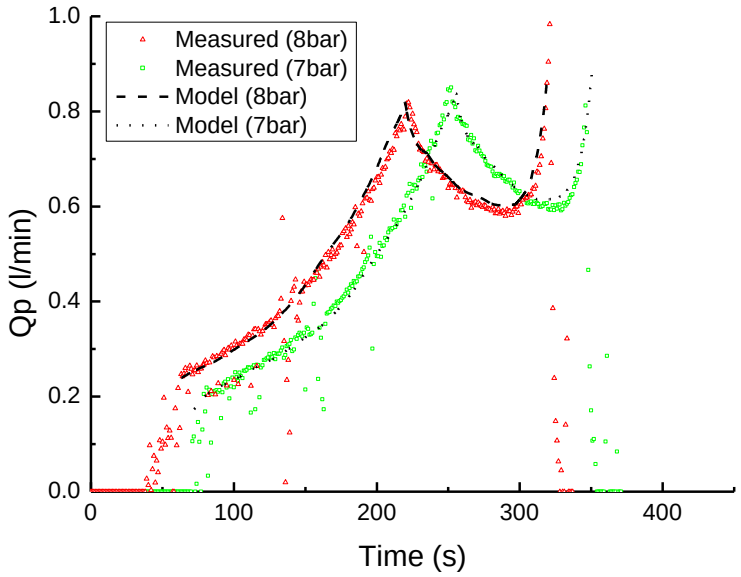

Figure 7.22 Permeate flow rates using feed water of 4500 ppm

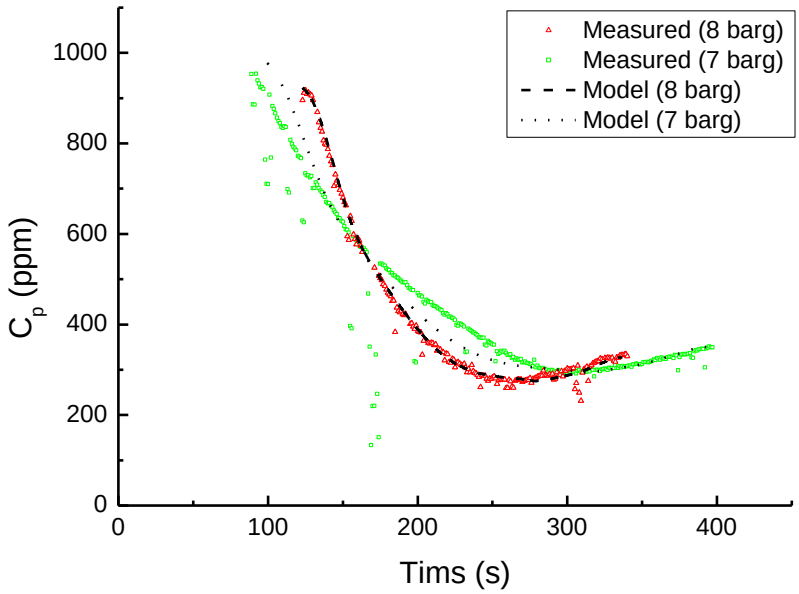

Figure 7.23 Permeate concentrations using feed water of 4500 ppm

7.8. Summary

In this chapter, the major subsystems of a prospective compressed air (to simulate steam in laboratory) powered batch-RO system are studied and experiments are conducted, the results show DesaLink has an efficiency of around 40% (*Figure 7.24*). The modelling procedures and the mathematical models of the subsystems are presented. The principle of modelling the DesaLink is to characterise its behaviour within the expected range of

operation. This means that the models developed can be expected to deliver a quantitative characterization and prediction of system performance for different operational conditions within the range tested (interpolation). Meaningful predictions may also be anticipated when using these models to study a wider range of operation conditions or even different system configurations. The reason is that models are based on known physical principles and the use of non-dimensional parameters makes them more readily applicable to systems of different configuration and size. The herein developed individual subsystem models were realized through the successful application of 'non-linear in the parameters Multiple Regression' fitting methods. On the basis of these models, a complete model of DesaLink in the Matlab/Simulink environment was built and was demonstrated and validated**.**

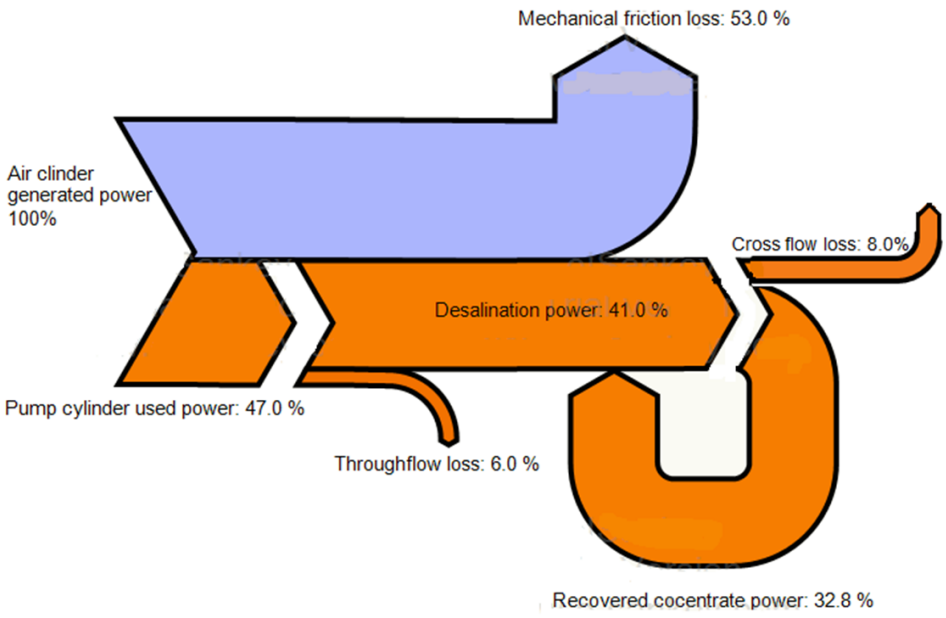

Figure 7.24 Sankey diagram of DesaLink (pressurization process), calculation based on 4000 ppm feed water, 8 bar of feed compressed air

Adjustments and refinements were implemented to the developed model, allowing for an accurate performance prediction for the various operation conditions of DesaLink. The refined model was validated by the good agreement between the model predictions and the additional experiments that were not needed for model development. This was expected because the individual component models had been optimized for the corresponding

subsystems. Nevertheless, the integration framework was proved successful while the refinement of the complete model was essential to improve the predictions. The final, refined Simulink model can be expected to deliver accurate predictions (less than 15% deviation from the experimental results) of the performance of DesaLink for feed water with different concentrations (2500–4500 ppm) and feed steam with different pressures (6.5–9 bar). Being able to do so computationally will allow us to assess critically and rapidly a wider range of system configurations and operation conditions, ultimately finding the optimal solution to a given real-world challenge.

Chapter 8

A CASE STUDY ON THE APPLICATION OF THE DESALINK SYSTEM TO A SMALL COMMUNITY IN A REMOTE, ARID AREA

Application of DesaLink was modelled for a real-world situation in which freshwater is supplied to a small community in a typical remote, semi-arid area. This case study exercise was conducted to demonstrate the feasibility and performance of integrated desalination systems that combined solar thermal technology and DesaLink. Different solar collectors were compared through theoretical investigations to assess different possible system configurations and, therefore, identify the optimum solution.

8.1. Introduction

As introduced in *Chapter 2*, the solar thermal cycle in the form of the Rankine cycle has appeared as a promising technology for powering RO desalination by converting heat into shaft work to power a conventional pump. The low efficiencies (less than 4%) of the few available solar RC-RO systems seem disappointing. Nevertheless, the overall solar powered RO desalination system performance, e.g. energy efficiency, can be markedly improved when the solar collector is coupled with the DesaLink batch process for desalination, as already described in earlier chapters. The solar-DesaLink can be especially attractive to meet the drinking-water demands for inhabitants of a small community in a remote, semi-arid area, where both water transmission systems and electrical power capacity are lacking. This chapter deals with the design of a tailor-made solar-DesaLink desalination system for a small community located in north-west India.

8.2. The system, modelling and optimisation method

The solar RC-DesaLink desalination system described in this chapter consists of a number of sub-systems integrated into one. As illustrated in *Figure 8.1*, the heat from solar radiation is absorbed through the vapour generator (e.g. solar collectors) and the temperature of the heat transferring or working fluid (depending on the particular RC configuration: heat transfer or direct vapor generation) rises and the fluid evaporates as vapour if the temperature higher than the boiling point under certain pressure. The vapour flows into the power cylinder of the DesaLink and thus drives the desalination process. After expansion, the exhausted vapour then flows back into the RC and is condensed in the condenser before it is compressed to the RC's highest pressure by the pump.

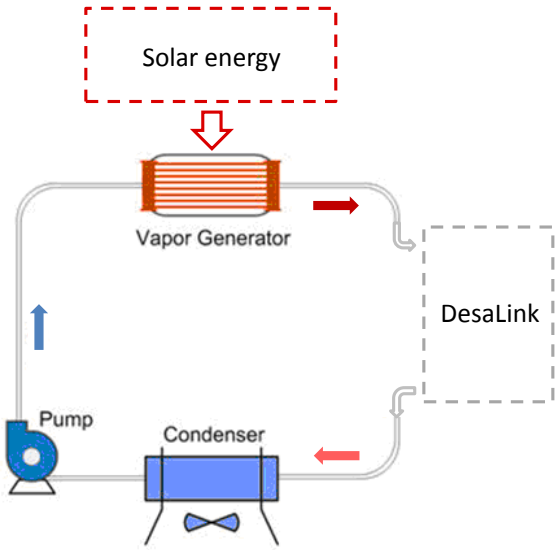

Figure 8.1 The integrated solar RC-DesaLink system

The main criterion for designing the solar-DesaLink system is that the water production capacity should be able to cover the drinking needs of a selected community. This required freshwater capacity implies a fixed vapour production from the vapour generator. Detailed steps of the solar-DesaLink design are as follows:

1. With the population of the selected community known, the required water production can be estimated according to the US Environmental Protection Agency

recommendation that at least 2 litres of freshwater (including the water contained in food) should be consumed for an average American adult (Agency 2011). Therefore, corresponding required vapor amount for the production of the certain quantity of water by using DesaLink is known, and the thermal input to generate such amount of high pressure vapor can be calculated.

2. With Step 1 determining thermal input from the absorption of solar energy, the required land occupation of the installed solar collectors can be obtained based on the solar collector efficiency and the meteorological data of the selected location.
3. Finally, based on the annual estimations of the hourly direct solar radiation, the production of the DesaLink system on a daily basis can be calculated.

Following the above described steps, the design studies were conducted and are represented in the following sections.

8.3. Case study description

8.3.1. Ground water resource of the Bikaner district, Rajasthan, India

The Bikaner district is located in the north-western part of Rajasthan and encompassed between northerly latitudes 27º11' to 29º03' and easterly longitudes 71º52' to 74º15'. According to a report from the Times of India (2010), drinking water shortage has reached an alarming proportion in most of the villages in the Bikaner district. The crisis has been further compounded due to the reduced supply from the Indira Cgandhi Canal and the fact that water tanker owners are charging huge amounts of money, which are beyond the reach of common villagers.

The ground water resources in the Bikaner district are brackish to saline with concentration values from 400 ppm to over 10000 ppm (*Figure 8.2*). Ground water with a concentration less than 400 ppm can be found in a small area around the northern part of Poogal Tehsil. The ground water with a concentration less than 2000 ppm can only be found in the small part of the south-eastern district, i.e. Nokha Tehsil, the north-western part of the district, i.e.Chhatargarh Tehsil and the north-eastern district, i.e. Lunkaransar Tehsil. In most

parts of the western and eastern district, the concentration of the ground water varies between 3000 to 10000 ppm with a maximum of around 12000 ppm ground water in most parts of Khajuwala Tehsil. In other words, the only viable water resources in the district are not readily suitable for domestic or irrigation purposes. Thus, it is worth exploring the potential of ground water desalination as an effective means to alleviate the local water shortage.

The Kolayat Tehsil was found to be the most interesting area for brackish water desalination. It is in the south western part of the district, having a groundwater resource with an average conductivity of around 7485 µs/cm (approximately 4000 ppm). Moreover, the area has abundant solar radiation over a large part of the year, making it an ideal case to assess the performance of our solar-DesaLink desalination system in a real-world application. One of the villages in Kolayat Tehsil, Rekh Ranasar, was selected for the case study. Rekh Ranasar is a small village inhabited by 163 residents according to the last census, which means 326 litres drinking water is required daily.

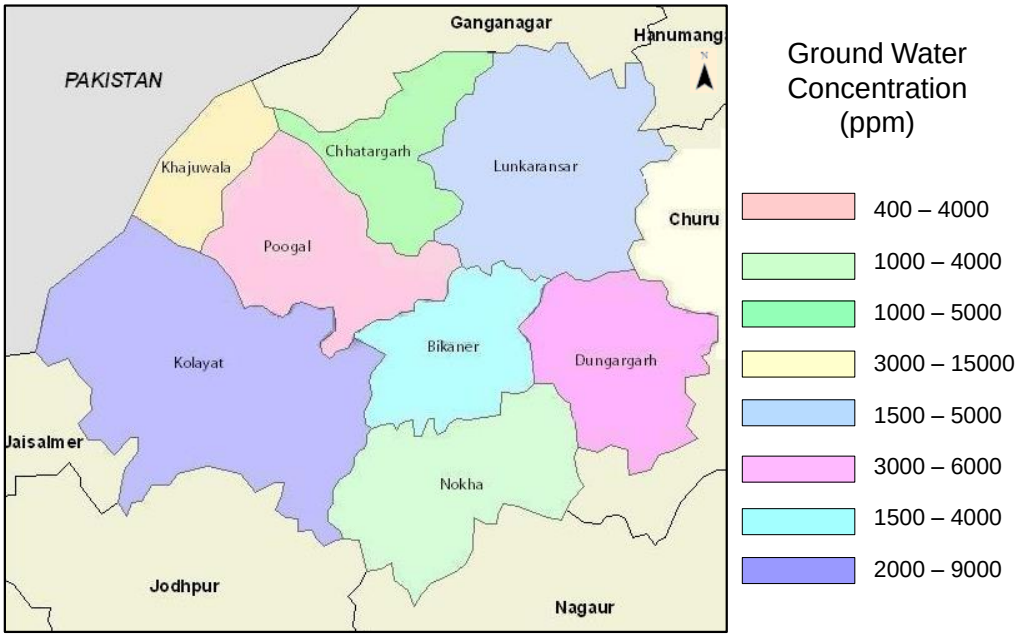

Figure 8.2 Distribution of ground water concentration in Bikaner district, Rajasthan. Picture is generated based on a government report: central ground water board (March, 2009).

8.3.2. Weather data

8.3.2.1. Air Temperature

The ambient air temperature affects solar collector efficiencies. The convective heat loss is proportional to the difference between some average temperature and ambient temperature. So it is preferable to install the solar collector in a warm place. Figure *8.3* shows the yearly variation of the monthly mean ambient temperatures in the Kolayat Tehsil, Bikaner district, Rajasthan, India. It is seen that the highest temperature happens in June. The average temperature during the summer (June, July and August) is 33 ºC. The average temperature, however, falls to 14 ºC during the winter (December, January and February). The daily temperature difference during day time is less than 15 ºC for both summer and winter (*Figure 8.4*). In the summer, larger amounts of freshwater are likely to be needed by the inhabitants as compared to the winter.

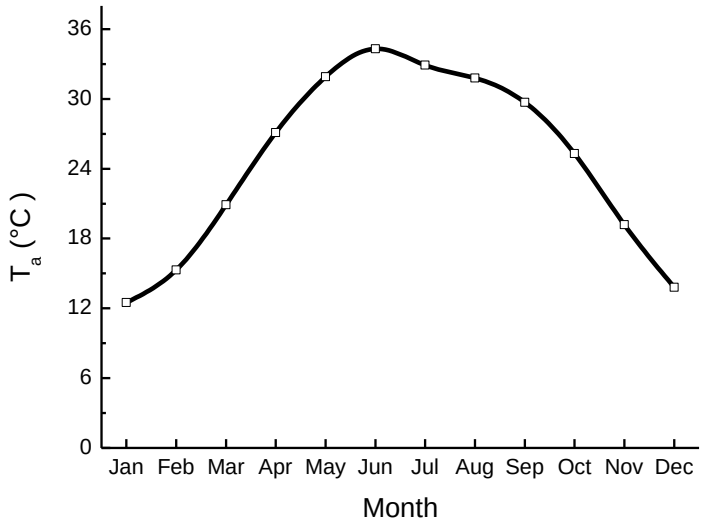

Figure 8.3 Climate data for Bikaner district

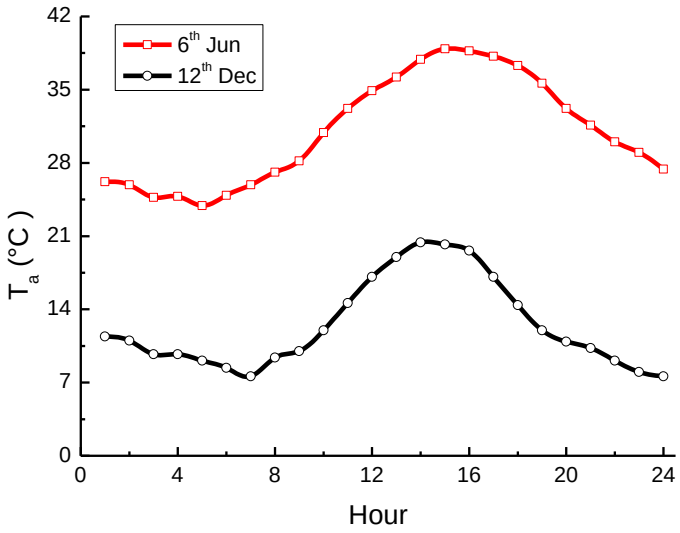

Figure 8.4 Hourly temperature changes in a day

8.3.2.2. Solar irradiance

The local solar irradiance data were acquired using the Meteonorm V4.0 software, which predicts solar irradiance for the chosen location, Kolayat. The site altitude is 230 m and the longitude and latitude are 72.6° and 27.7°, respectively. *Figure 8.5 (a)* shows the average hourly horizontal global irradiance (G_Gh) data for the year-long time. The maximum values of the mean irradiance of global radiation are 954 and 694 W/m^2 for the typical summer and winter day in *Figure 8.5 (b)*, and the solar irradiance effectiveness hours are 14 and 10 hours, respectively. Such high solar irradiances, especially in the summer, give rise to a big advantage of utilizing solar thermal technologies in this area.

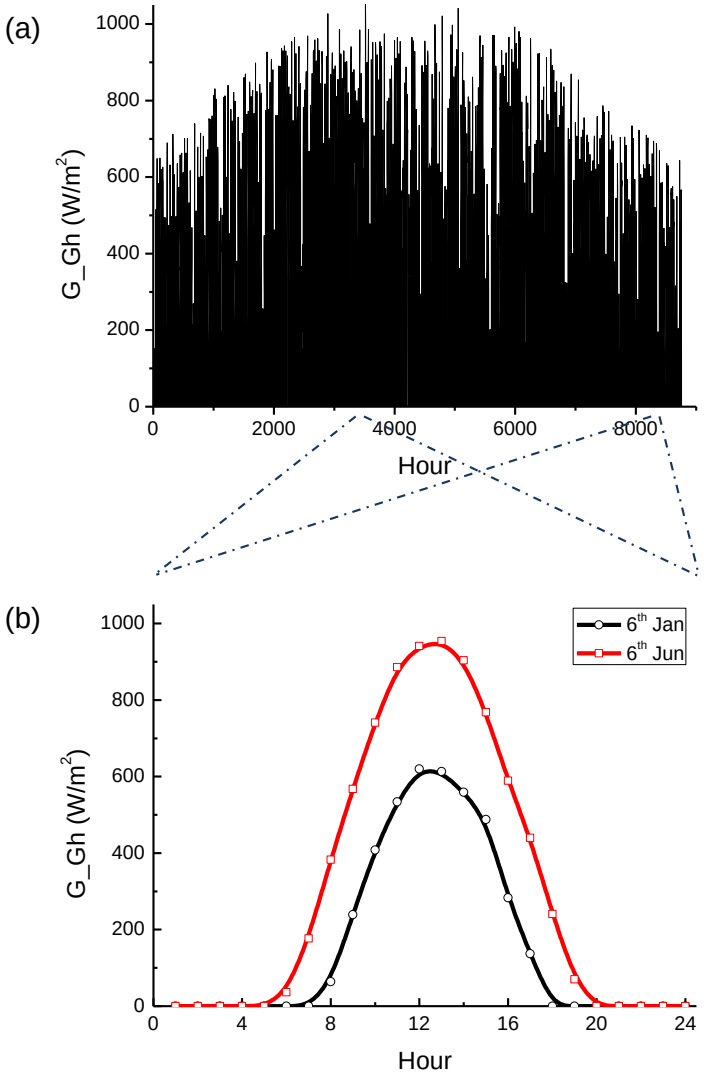

Figure 8.5 Yearly and daily horizontal global irradiance

8.4. The Kolayat Tehsil case

As previously stated, one of the villages in Kolayat Tehsil was selected as the location for demonstrating the applicability of the solar-DesaLink system to satisfying the needs of freshwater for the local residents. The village is inhabited by 163 residents, which means a freshwater production of 326 litres per day is required. DesaLink can produce around 2.5 litres of freshwater per cycle (takes around 6 minutes depends on feed air pressure and feed concentration) and the corresponding feed steam volume is 2 litres. In other words, a total steam volume of 260 litres (i.e. 1.21 kg in weight) is required, which leads to a total energy input of 2273 kJ for generating such an amount of steam.

8.4.1. Solar-DesaLink Model

A screen snapshot of the top layer of the solar-DesaLink model hierarchy is shown in *Figure 8.6*. The blocks used and their main functionalities are gathered in *Table 8.1*. The performance of the solar thermal field was examined for three different types of solar collectors, as discussed in the following section.

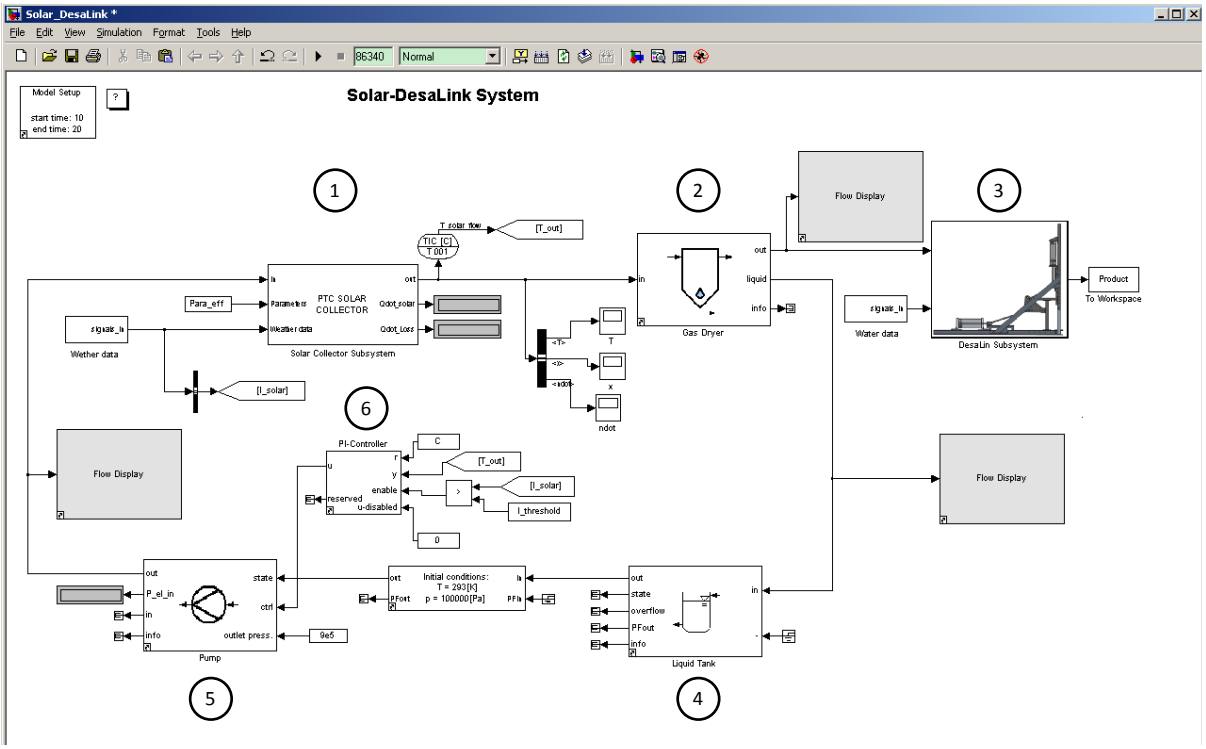

Figure 8.6 The top layer of the solar-DesaLink model hierarchy in Matlab/Simulink environment

Table 8.1 Detailed information of the blocks in solar-DesaLink model

No.	Block name	Inputs	Out puts	Main function
1	Solar collector subsystem	▪ Meteorological data depending on the geographical location, generated from MeteoNorm ▪ Solar collector efficiency parameters ▪ Incoming water flow	▪ Outgoing water flow ▪ heat input and loss	Models the solar collector subsystem by calculating the heat input to the working fluid and simulating the working fluid state changes
2	Gas dryer	Incoming heated flow	▪ Dried steam flow ▪ Remaining liquid flow	Reduces the liquid portion of the incoming flow of wet steam
3	DesaLink subsystem	▪ Feed water data ▪ Feed dry steam flow	Average concentration and volume of freshwater	Calculates the produced freshwater by integrating flow rate and salt passage
4	Feed water tank	Incoming water flow	Outgoing water flow	Source of the working fluid
5	Pump	▪ Incoming water flow ▪ Actuator value	Outgoing water flow	Increases the pressure of working fluid to desired value
6	PI controller	▪ Temperature of the fluid at the outlet of collector ▪ Solar irradiances	Actuator value	Manipulates the pump flow rate through the solar radiation and the outlet temperature of the solar collector

8.4.2. Solar thermal field

As stated in *Chapter 3*, water is the working fluid for the solar-DesaLink system. Thus, solar collectors which can reach a temperature higher than the saturation temperature of water at 9 bar (175.4 ºC) are considered, including the evacuated tube collector (ETC) and the parabolic trough collector (PTC). Other solar collectors such as the high temperature parabolic trough collector and the linear fresnel reflector are not considered in the present analysis, due to their large aperture area, high capital, M&O costs and high temperature ranges (up to 400 ºC) which are not necessary in this case.

The input parameters required (i.e. heat input Q_{solar} from the solar collector) for Simulink to integrate the solar collector subsystem into the Solar-DesaLink system was obtained by (*Eqs. 8.1* and *8.2*):

$$Q_{in} = I_{solar} \cdot A_{solar} \cdot \eta_{solar} \tag{8.1}$$

where I_{solar} is the direct solar irradiance (W/m^2), A_{solar} is the area of the solar collector (m^2), and η_{solar} is the efficiency of the solar collector efficiency, which has an expression as follows (Karellas, Terzis et al. 2011):

$$\eta_{solar} = \eta_0 - a_1 \cdot \left(\frac{T_{flu} - T_{air}}{I_{solar}}\right) - a_2 \cdot \frac{\left(T_{flu} - T_{air}\right)^2}{I_{solar}} \tag{8.2}$$

where η_0, a_1 and a_2 are the efficiency parameters, decided by the collector efficiency curves of solar collector, T_{flu} (ºC) and T_{air} (ºC) are temperature of the fluid at the outlet of the solar collector and the ambient temperature, respectively.

Three representative solar collectors were selected for this case study (datasheet is shown in *Appendix D.3*): two evacuated tube collectors (ETC), and a single tracking parabolic through collector (CPC). Their technical parameters are shown in *Table 8.2*. High

stagnation temperatures (>175.4 ºC) of both types of solar collectors indicate their capabilities to be used for the solar-DesaLink application. The PTC collector has a higher efficiency of around 60% compare to the ETC collector efficiencies of 45% (*Figure 8.7*), but on the other hand so is the cost. The ETC solar collector has its own advantages such as its smaller aperture area, lower cost, and low construction and maintenance cost because of the absence of a tracking system. In this case, the stationary compound parabolic collector (CPC) was not considered, because the large difference between T_f and T_a will yield a small efficiency.

Table 8.2 Technical data of solar collectors

		Evacuated tube collector (ETC)		Compact parabolic trough collector (PTC)
Technical data	Module	De Dietrich POWER7 (Forschung 2009)	VITOSOL 300 (Delgado-Torres and García-Rodríguez 2010)	Solitem PTC 1000 (I.E. Agency 2005)
	Maximum operating pressure (bar)	10	—	—
	Minimum flow rate (L/h)	30	—	40
	Stagnation temperature (ºC)	323	—	590
	Cost (€/m^2)	120–180	—	200–400
Efficiency parameters	η_0	0.745	0.73	0.75
	a_1 (w/m^{2}K)	1.53	1.26	0.12
	a_2 (w/m^{2}K^2)	0.0003	0.0041	0.0013
	Aperture area (m^2)	0.801	2.15	2

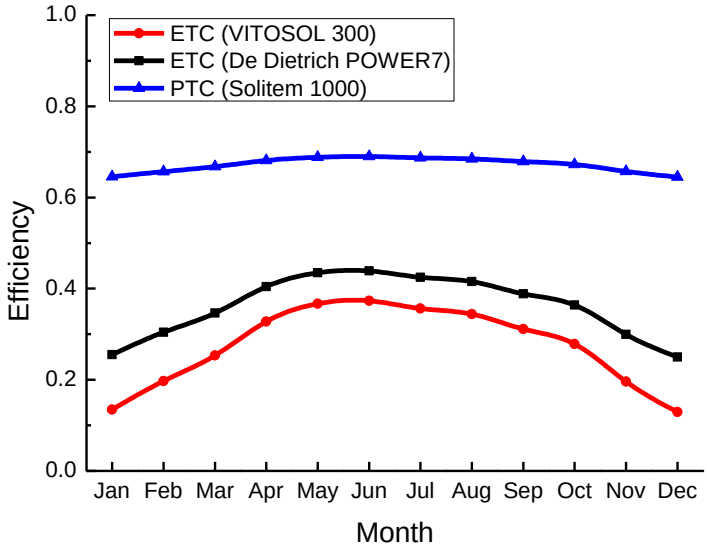

Figure 8.7 Solar collector efficiencies over the year (solar collector efficiency is calculated based on Eq. (8.2) using an average radiation of a typical day of each month, a fixed outlet temperature of the solar collector of 180 ºC and an average day time ambient temperature).

8.4.3. Results and Discussion

A case study for the village of the Kolayat Tehsil is performed to illustrate the applicability of the solar-DesaLink system. The criterion fixed to calculate the solar field size is a production of about 330 litres drinking water per day with the different types of collectors. In order to ensure a sufficient production of freshwater the whole year round, the production under the most disadvantageous weather conditions (least solar irradiance, lowest ambient temperature and shortest daytime) should be considered as the minimum requirement of the solar-DesaLink system. To decide on the area of the solar collector needed, we assume an average of 300 W/m^2 of solar irradiance (according to *Figure 8.5*, winter case) is received by the solar collector with an efficiency of 15% resulting in less than 2 m^2 (1.3 m^2) of solar collector being required to receive enough heat in an 8-hour day. In the case of solar-DesaLink system combined with ETC collector, the aperture area of the ETC collector (De Dietrich POWER7) is 0.8 m^2, thus, two modules of such solar collector totalling an area of 1.6 m^2 are adopted. In another case of using ETC (VITOSOL 300) and PTC (Solitem PTC 1000)

collectors, one module of collector, i.e. 2.15 and 2 m^2, respectively, was assumed for the modelling.

In all the simulated cases the meteorological data (solar irradiance and air temperature) for the Kolayat Tehsil area are generated using MeteoNorm V4.0. To obtain the maximum annual solar irradiance striking on a stationary ETC, the ETC collectors were modelled to be arranged in a true south orientation, i.e., Azimuth=0º, and a tilt angle of 25º was assumed. For the PTC with tracking system, a true south orientation was also assumed and the 'tracked radiation' function in MeteoNorm was used to obtain the solar irradiance. Then the meteorological data files were distributed in *.mat* format and integrated in the input files of the Solar-DesaLink model. The completed model can simulate the system performance during any period from a few hours up to one year. In this case, simulations are performed for days (from 0 to 86400 seconds) of 12 months to estimate the output for a typical day and the whole year.

First, the herein adopted modelling protocol is demonstrated with the simulation results for a typical day. *Figure 8.8* shows the solar irradiances and the actual heat input by the solar collector over the 24 hours of the day (86400 seconds). The actual heat input is given by multiplying the solar irradiances by solar collector efficiency (*Eq. 8.1*). It is also seen from *Figure 8.8* that the efficiency of the solar collector first decreases as the solar irradiance increases, and then increases after the solar irradiance's passing the highest point — the working fluid temperature rise to the evaporation temperature and then decreased.

The solar irradiance reaches the highest point in the noon, leading to the corresponding heat input also achieving the maximum which in turn give rise to the maximum mass and volume steam flow rates (*Figure 8.9*). As a result, the total volume of high pressure steam generated is around 800 litres which can be used to power DesaLink for almost 473 cycles, giving a nominal total freshwater production of 910 litres.

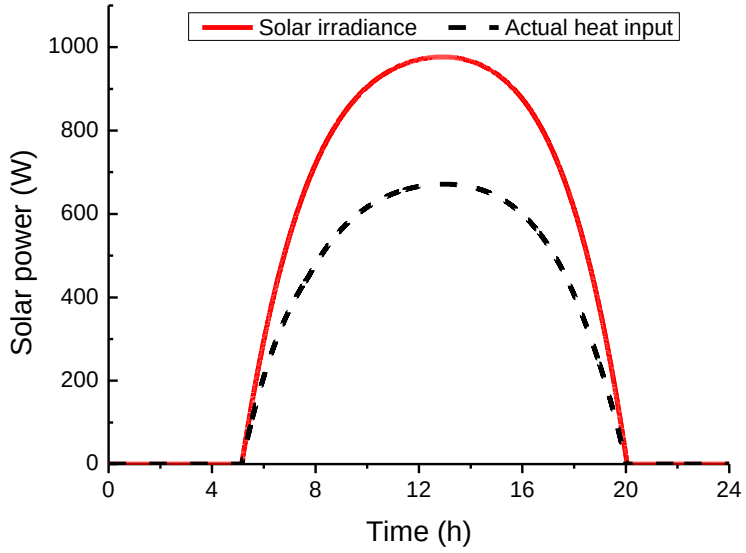

Figure 8.8 Solar irradiance and heat input from solar collector ETC (De Dietrich POWER7) over a typical summer day (6th Jun).

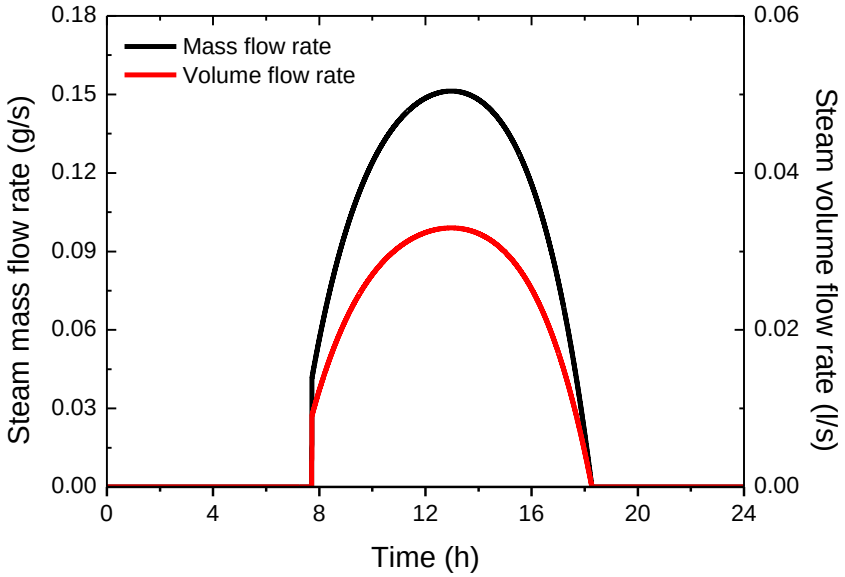

Figure 8.9 Mass and volume flow rate of steam over a typical summer day (6th Jun), coupled ETC (De Dietrich POWER7).

Once the thermal energy captured by the solar collector is calculated, the generated steam amount is also estimated as well as the desalted water amount. *Figure 8.10* shows a example of daily results. Here, the quotient between desalted water volume (V_p) and the solar collector aperture area applied (A_{solar}) is used as a performance parameter, named specific

volume of desalt water ($\dot{V}_p$). The obtained $\dot{V}_p$ using each solar collector model is given in *Figure 8.10* for typical summer and winter days.

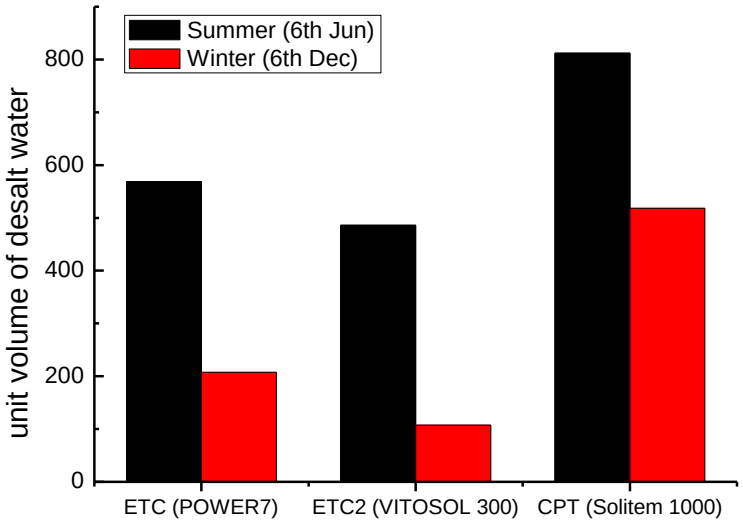

Figure 8.10 The amount of desalt water (l/m^2) by using different solar collectors

Second, using the above-detailed modelling approach, freshwater production of the particular solar-DesaLink configuration is examined on a monthly basis for a whole year (*Figure 8.11*). It is shown that the system can produce enough freshwater for the drinking needs of the village over the whole year. It also can be seen that the nominal water productions in the summer period (Jun, Jul and Aug) are three times the required amount. This means excess freshwater produced may be used for other purposes such as irrigation, or a shorter operation may be applied in hot summer days.

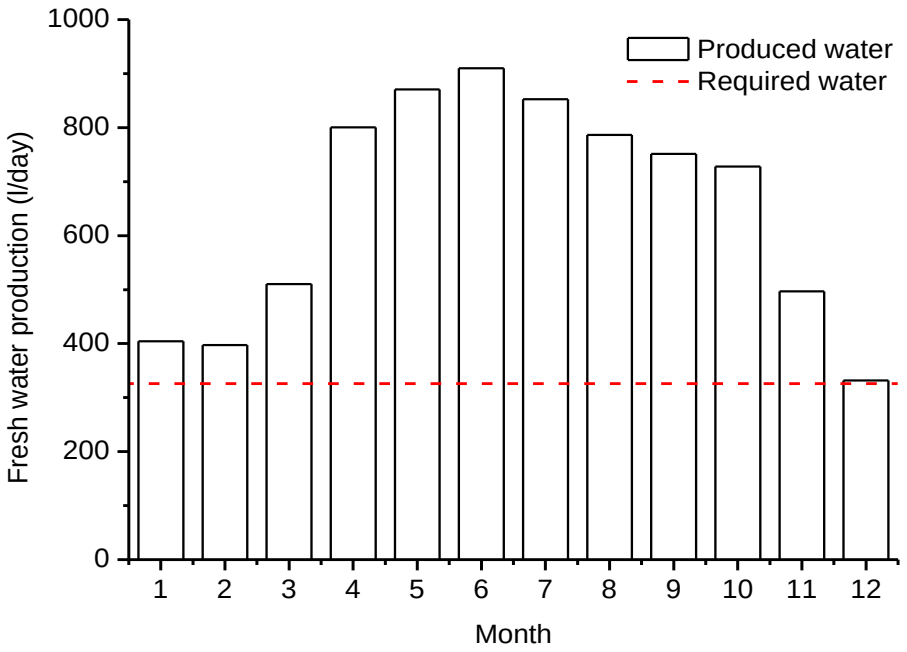

Figure 8.11 Simulated water production for a whole year, the red dash line shows the required amount of drinking water, coupled with ETC (De Dietrich POWER7).

Simulation results for the yearly system performance with the different feed water concentrations and solar collectors were gathered and are presented in *Table 8.3*. The desalted water qualities were calculated using the DesaLink simulation model block. The two investigated concentrations of feed brackish water were 2000 and 4500 ppm, representative of the concentration levels usually found in the ground water in the Kolayat Tehsil area (*Figure 8.2*).

Table 8.3 Results overview for Kolayat Tehsil area

	ETC1	ETC2	CPC
Solar collector areas (m^2)	1.6	2.15	2
Number of solar collectors	2	1	1
Evaporation temperature (ºC)	165-175	165-175	165-175
Feed water temperature (ºC)	20-30	20-30	20-30
Working fluid mass flow rate (g/s)	0.55	0.55	0.55
Nominal freshwater production (litre/d)	332-925	360-1150	840-2033
Freshwater concentration (ppm)	270-527	270-527	270-527
DesaLink efficiency*	35%-42%	35%-42%	35%-42%

Table 8.3 (Note:*DesaLink efficiency=pump used work/power generated work) demonstrates that when coupled to solar energy a very good performance of DesaLink can be expected. The water productions exceed the target (360 litres per day) and the concentrations of produced water meet the requirement of drinking water.

8.5. Summary

A case study has been presented to demonstrate the encouraging applicability of a solar-DesaLink system in real-world situations, such as the location chosen here (Rekh Ranasar village, Bikaner district, Rajasthan, India). The required areas of the chosen solar collectors were determined based on the need to produce 360 litres of freshwater per day to satisfy the consumption of local inhabitants. It was found that an ETC or PTC solar collector with an area of less than 1 m^2 could meet this water production over the whole year.

Compared to typical PV-RO and RC-RO systems, the solar-DesaLink system proposed in this work is promising for real-world applications. This originates from the markedly innovative design of DesaLink, which allows for an efficient use of solar energy, i.e. the system efficiency ratio is ten times that of a BW PV-RO system. For example, in a typical winter day (6^{th} Dec; the smallest water production, i.e. the lowest system performance), the total solar energy by a 1.6 m^2 solar collector is 6.1 kWh and the solar-DesaLink system can produce a total of 332 litres (0.332 m^3) freshwater. This gives a solar energy usage of 18.4 kWh/m^3, which is still much smaller compared to the ones (25–120 kWh/m^3) of typical PV-RO systems (*Table 2.2*, *Chapter 2*). To put this comparison into context, the proposed solar-DesaLink combination is certainly worth further exploring for providing freshwater to small communities, especially those in rural areas where electricity supplies are costly. Note that both PV-RO and RC-RO systems are prone to performance deficiencies as the system scale decreases, a direct result of the low efficiencies associated with small-size pumps and turbines. Future R&D work may be worth conducting to further reduce construction costs of DesaLink, making it affordable for even the most economically deprived regions. Nevertheless, the system still has to be tested in the field with real sources of solar thermal energy and brackish ground water. In practice, thermal losses will occur; however, the 10-

fold improvement reported here is sufficiently large that a substantial improvement is likely to be observed in practice.

Chapter 9
CONCLUSIONS

The key contributions of this research are summarized and discussed in the context of providing direct responses to the aims and objectives that are listed in Section 1.4. Further development and recommendations are outlined.

Salt water desalination by means of RO membrane has been identified as an effective method in helping to address the water crisis. To alleviate the energy shortage and to reduce impact on the environment, RO systems should be powered by renewable energy sources. Due to the fact that abundance of solar energy is usually available in arid areas, the choice of mature solar energy capturing technologies, either in the form of solar PV or thermal, combined with RO desalination is a reasonable and feasible approach to tackling the current water shortage issue, especially for the semi-arid areas which are far from the coast.

9.1. Background and batch-RO system development

Objective 1: Review the state-of-the-art in solar powered desalination technologies, to critically assess and evaluate current popular solar RO systems and compare their performances (Chapter 2).

With the help of the advanced technologies of both RO desalination and solar cells, medium and small scale solar PV-RO systems have been implemented widely in arid or semi-arid areas. They exhibit good performance in terms of their specific energy consumption (SECs) which can be as low as 5 kWh/m^3 (depending on system size). However, comparing their SECs with the ideal theoretical limit of energy usage (at 70%

recovery ratio) which is 0.15 kWh/m^3 for BWRO and 0.94 kWh/m^3 for SWRO (*Section 2.4.1*), it is clear that their performances leave much scope for improvement. In other words, there is still huge room for them to be improved by typically 40 times for SW PV-RO systems and 200 times for BW PV-RO systems (*Table 2.2*) according to the theoretical solar energy conversion limit.

An alternative to the PV-RO system is the solar RC-RO system. Since they are still at the early stage of development, with very few plants having been built, only a few modelling and design studies have been carried out based on different solar collector types and working fluids (*Table 2.3*). In principle, the parabolic trough collector behaves better than other collectors. However, the choice of working fluid remains controversial. Further analysis on choosing a cost effective solar collector, a suitable working fluid and a practical high efficiency expanding machine is required. Owing to its promising features, such as the efficiency, a lower cost than PV and applicable to a co-generation system, the RC-RO system was selected in this work for detailed investigation.

Objective 2: Understand the loss mechanisms in solar powered RO desalination system (Chapter 2).

For the large SWRO system adopted with high efficiency ERD, the energy losses are mainly dependant on membrane resistances which are heavily related to membrane types and conditions. Another energy loss is caused by longitudinal excess operation pressure. The energy losses can be much larger for current BWRO systems. Due to their low operational pressure and high recovery, these systems rarely include ERDs, resulting in further losses. Additionally, the smaller inverter and pumps which are adopted in the small or medium brackish water system have low efficiencies.

With regard to the solar PV-RO systems, usually mono- or multi-Si solar panels are adopted, not least because of their relatively low costs and commercial availabilities. Despite the fact that the RO desalination market is dominated by PV-RO, significant energy

inefficiencies of such systems still prevail. For the PV subsystem, successive losses (*Figure 2.10*) that happen during energy conversion mean the Si solar cells have less than 15% efficiency, which is much lower than the theoretical solar energy conversion limit—86.8%. In respect to the solar RC-RO systems, the preliminary studies reveal that the energy conversion efficiency of the RC subsystem is comparable with the solar PV cells, which is around 20% (*Table 2.3*). However, this number will be reduced when applying solar RC technology to small scale BWRO systems due to the low efficiencies of small size components, such as turbines, pumps and converters. Energy losses are unavoidable during energy conversion, i.e., solar (PV) or mechanical (RC) energy to electrical energy. This leads to an idea of saving energy losses by cutting energy conversion steps in solar RO desalination, therefore increasing system efficiency eventually.

Objective 3: Compare different configurations of RO system with regard to efficiencies and recovery, including multistage systems, system with and without energy recovery and batch or closed circuit systems (Chapter 3).

For the RO subsystem, beside the concentrate energy loss which can be reduced or eliminated by recovering the high pressure concentrate, another major loss is caused by longitudinal excess operation pressure. To reduce this type of energy loss, multi-stage operation is an option (*Section 3.2.1*). Theoretically, it can effectively save energy loss (by 30% at 70% recovery ratio), depending on the stage numbers and recovery ratio (*Figures 3.10 and 3.11*). However, adding more stages of RO module and booster pumps can significantly increase the capital and O&M costs; thus, an alternative means i.e. batch-RO system has been designed and developed to achieve an efficiency improvement. The main working principles of batch-RO system are (i) recycle high pressure concentrate back to feed water; and (ii) increase feed water pressure according to the rise of the feed water concentration. Theoretical analysis and comparison of batch-RO and other suggested RO systems with different configurations, i.e. multi-stage and CCD-RO systems have shown significant improvement of batch-RO systems (60% at 70% recovery ratio) in terms of SEC

(*Figure 3.11*). This improvement is reliant on assumptions regarding the robustness of the membrane module under variable-pressure (cycle of load and unload) conditions in batch operation.

At the stage of choosing a power system for the batch-RO, the solar PV and RC electrical technologies were discarded for system integration, because of additional inefficiencies in energy conversions. With regard to reducing the number of energy conversion steps, a mechanical means of using linkage subsystems was instead favoured; that is, the batch-RO is designed to be powered by mechanical energy (steam expansion) directly (*Section 3.5*).

9.2. Solute transfer in batch-RO system

Objective 4: Study in-depth specific loss mechanisms in the batch-RO system associated with solute transfer (longitudinal dispersion and concentration polarization) through theory and experiments (Chapters 5 and 6).

Energy losses that relate to dispersion and concentration polarization can deteriorate batch-RO performance. Thus, both dispersion and concentration polarization were investigated in order to understand the relationship between them and energy usage, then improve the system performance.

To investigate and understand the effects of longitudinal dispersion happening during the purging phase of DesaLink operation on performance deficiencies, both theoretical analyses and experiments were developed. The dispersion phenomena in the spiral wound RO elements used in this work were studied using the Taylor dispersion theory. It has been found that the dispersion can be either convection dominated or be combined with diffusion, depending on the feed flow rate under study, see *Figure 5.6* for an example. The herein developed theory for the dispersion in a spiral wound RO element was validated and further refined by experiments. Taking the results reported in *Figure 5.11* as an example, the volume of purging water, which is equal to the volume of the solution inside the module, was derived

and adopted to achieve a high recovery ratio with only a minimum deduction (around 5%) in system energy efficiency compared to the ideal, zero-dispersion situation.

With regard to the concentration polarization, Sherwood correlations have been found suitable to quantify the solute transfer in steady fluid systems. In the case of spiral wound RO membrane modules where non-steady flows arise from the complex module geometry, however, the conventional Sherwood correlation for plane channels is not accurate. Therefore, a new correlation, which is based on the Sherwood correlation, was proposed and further verified by experiments conducted with two different RO membrane modules. The good agreement between model predictions and experiments indicates that the newly proposed correlation might be generally applicable to other similar spiral wound RO membrane elements (*Figure 6.7*). Under non-steady flow conditions, i.e. batch-RO operation, reducing concentration polarization is crucial. The reason is that the feed water flow rate is low (less than 3 l/min), implying a small solute transfer rate, hence a large CP value can be expected. Experiments using different average feed flow rates were conducted using DesaLink in order to reveal the relationship between solute transfer rate and energy consumption; for example, it has been found that energy usage is increased by around 10% when the feed flow rate is decreased by 25%. The trade-off between these two factors (i.e., solute transfer rate and pump energy input) was decided with the help of the developed theoretical models. Moreover, to gain an understanding of the solute transfer in the RO system, experiments employing two different types of membranes were conducted (*Figures 6.3 and 6.4*) over a wide range of operation conditions (feed concentration 60-5000 ppm, feed pressure 6-9 bar). The popular models that are suited to describing and predicting mass transfer in respective RO membrane elements were validated by experiments; they can be applied in future model development for system modelling in other applications.

9.3. DesaLink development and modelling

Objective 5: Develop a practical system based on batch mode RO (namely, the DesaLink system) and characterise its performance through experimentation and modelling (Chapters 4 and 7).

With the specifically selected instrumentations that are centred on and controlled by NI LabVIEW software, the DesaLink system was built and tested. DesaLink used a compressed air system as power source under the laboratory conditions, which was demonstrated to yield a good DesaLink efficiency (around 40%) over a broad range of operation conditions (feed air of 6.5–9 bar, feed water concentration of 2000–4500 ppm). Moreover, DesaLink was subject to long-term membrane tests (6 hours) under intermittent and variable flow and pressure conditions; no apparent degeneracy in membrane module performance was observed, indicating a consistently good quality of produced water. The freshwater produced had an average permeate concentration of below 500 ppm, a quality that complies with drinking water standards in the literature. Such results, although established under laboratory testing, gives us confidence that a good performance may well be achieved when DesaLink is powered by solar-energy-generated high pressure steam, because similar expansion behaviour to compressed air can be expected. One potential concern is that the operation of an RO system in batch mode generally is prone to reductions in average flows compared to a continuous operation. Nevertheless, DesaLink, a system making use of batch-RO, can be attractive for providing essential healthy drinking water to small or medium communities in semi-arid remote poor areas, owing to its technical (simple structure and easy operation) and economical (low operation and maintenance cost) advantages over many other RO desalination systems on a similar scale.

The dispersion and concentration polarization phenomena in the systems of interest here were studied in detail. Numerical models to understand and quantify the corresponding effects were proposed and further validated against experiment; these models, initially developed for individual subsystems, were then integrated to afford an overall DesaLink

model (*Section 7.5*) that in turn was optimised and validated. The modelling representation of the linkage subsystem was developed based on its geometry, with its accuracy confirmed by experiments (*Section 7.3*). In particular, to improve the integrated model for the whole batch-RO system, modifications to the original (straightforwardly combined) model was introduced. This was achieved by including extra polynomial terms to compensate empirically for inaccurate of the chosen physical (subsystem) models for the overall system. Again, the refined models have been validated by experiment and have been shown to predict accurately the batch-RO performance; put precisely, compared to the experiments, errors were smaller than 5% in the simulated freshwater quantity and quality over a wide range of operation conditions (feed concentration 2000-4500 ppm, feed pressure 6-9 bar).

Objective 6: Apply the model to a specific case study of practical interest and investigate the influence of design parameters (Chapter 8).

After the completion of the DesaLink model with compressed air as the power source, modelling of the solar Rankine cycle was conducted using Matlab® Thermolib, making use of the Matlab-Simulink environment; the subsystem model developed for the Rankine cycle thereby was integrated with the DesaLink model. In other words, the final, complete model simulates the whole process starting from the absorption of solar irradiance by the chosen solar collector to the desalination of feed water by DesaLink. In Chapter 8, simulations were successfully applied to DesaLink powered by steam, which yielded an in-depth understanding in the variations of generated high pressure steam flows throughout the system with respect to the varying solar irradiance and feed-water concentration. The rate of water production varies throughout the day, resulting from different solar irradiance strengths over the time. Accordingly, the model can be used to perform an hour-by-hour prediction for a whole day; likewise, water productions for individual months in a year can be simulated. More instructive, perhaps, is that the model can also be used to evaluate various solar system configurations, as demonstrated in Chapter 8. Encouragingly, the simulations

suggest that the overall water production can meet the desired values (300–900 l/day) with a solar thermal collector having an area as small as 2 m^2.

9.4. Overview and Recommendation

Aim: define and develop a solution for desalination of brackish groundwater, suitable for use with low grade thermal energy such as solar energy.

To ensure the success in achieving this aim, the following three steps have been taken. Firstly, a careful review of the state-of-the-art desalination technologies was carried out. Special focuses were placed on the energy efficiencies and energy losses associated with commonly-used desalination systems. This actively afforded a good understanding in the topic and allowed for the successful identification of potential areas where innovations and/or improvements were needed.

Secondly, the batch-RO concept was proposed and described. The comparison of theoretical specific energy consumptions between the batch-RO and the conventional continuous RO operations suggested that batch-RO might provide an up to 60% improvement in system performance (that is, an improvement on the state-of-the-art with regard to energy efficiency and recovery). The influencing factors, namely, longitudinal dispersion and concentration polarization, were carefully examined and analysed, and corresponding theories were proposed for an accurate description of the phenomena.

Finally, the DesaLink system, a prototype that was made possible by our conceptual and theoretical investigations, was successfully constructed and extensively tested under laboratory conditions. In addition, the potential of coupling DesaLink with a solar-power source was evaluated computationally; both the experimental data acquired from the laboratory DesaLink tests and the simulated performances are encouraging, pointing strongly to the promise of DesaLink in real-world applications and, hence, to the necessity of a future continuation to this work.

It is clear, from the progress of the simulation work, that the adopted approach of experimental results assisting model development has been proven to be successful. For the power cylinder and linkage systems studied here, the literature based on theoretical models were sufficiently accurate when compared to the experimental results. For the RO subsystem, however, as stated in *Section 7.4,* all of the investigated "off-the-shelf" models that were aimed at describing diffusive and/or convective flows for continuous separation processes have been found not suited to predicting DesaLink performance. Therefore, these classic, physical models were augmented by simple, analytical terms to yield new, physically-motivated models that simulate accurately the performance of DesaLink under the variour operation conditions. By doing so, it is believed that the underlying physics of the DesaLink operation is well substantiated in our modelling, while anything that is missing from the physical models is implicitly accounted for by the extra empirical terms. In other words, this allowed us to predict accurately the system performance without introducing new parameters when adapting the model to the various batch-RO systems with different configurations. The modelling of DesaLink performance over a wide range of operation conditions (feed concentration 2000-4500 ppm, feed pressure 6-9 bar) has suggested possible directions for future investigations. Firstly, further improvement of the model could be carried out. In particular, membrane fouling can be a severe problem limiting the long term performance of desalination. Thus, the ability to predict accurately the membrane fouling and scaling factors under given conditions (for example, a deteriorating membrane performance over a long run) will undoubtedly bring technical and commercial benefits to actual experimentations and/or applications. Secondly, a pilot DesaLink system on site, ideally powered by steam that is generated by the heat coming from the sun, would be interesting not only to verify the reliability and accuracy of the theoretical model but also to assess the design principles of DesaLink in real-world scenarios.

Another aspect need to be considered for such systems is the pre-treatment process. Brackish surface water typically has a greater propensity for membrane fouling and requires more extensive pretreatment systems than groundwater resources. Different methods should

be carefully selected in order to cause minimum membrane fouling at the lowest possible cost. And the chemical dosing degrees has to be precisely calculated depending on the scale forming salts contained in the feed water. For example, for water with low bacteria content, pre-treatment may only require dosing with polyelectrolyte as flocculation agent, and dosing with H_2SO_4 to reduce the pH level and thus prevent $CaCO_3$ precipitation. On the other hand, in the case of water with high bacteria content, more steps of chlorine dosing and dechlorination should be added before the final stage consisting of a cartridge filter. Utilization of microfiltration (MF), Ultrafiltration (UF), or nanofiltration (NF) to pre-treat RO feed water, as effective substitute of conventional pre-treatment, has became a new trend. Pilot-scale testing of these membranes has been carried out by researchers. To date, UF membranes are the most common choice in research studies and pilot testing. Because UF membrane has smaller pore sizes than MF membranes that can achieve more effective removal, and higher flux than NF membranes to treat feed water with relatively lower energy consumption. All three membranes have advantageous characteristics, such as superior removal of organic and particulate matter. However, like the RO membranes, these pre-treatment membranes are easily fouled.

In general, the structure of DesaLink is simple and easy to construct, and its operation is also straightforward; nevertheless, the innovative design and concept have been shown to be elegant and effective throughout this work. When it comes to combining DesaLink with a solar thermal subsystem, even the least sophisticated solar collectors (e.g., the evacuated tube type) can be used to achieve a satisfactory water production. Regarding the maintenance for DesaLink, it is noteworthy that only the water pump required special treatment and follow-up maintenance to prevent water leakage, which has been mostly concerned with the initial stage of constructing DesaLink. However, after using a high-quality seal, together with a food-safe lubricant for the water pump piston, water leakage was not observed for a period of 3 months, at least.

The DesaLink system described in this thesis appears to be a technology that may be worth commercialising, with some further development, for example, to reduce capital costs.

In general, when considering combining RO systems with renewable energies the commercialization of the former appears to be restrained by the development in renewable energy technologies. In contrast, batch-RO systems are powered directly by mechanical energy, DesaLink being an example; they can be more technologically feasible and commercially attractive where thermal energy in any form is available to provide steam. We foresee that in the development of the next generation of high recovery BWRO desalination technology, batch-RO certainly deserves more intense research effort and may very well make remarkable contributions in the future.

REFERENCES

1. Agency, U. E. P. (2011). Exposure factors handbook 2011 edition (Final), US Environmental Protection Agency Washington, DC.
2. Agency, I. E. (2005). "Solar Heat for Industrial Processes, Medium Temperature Collectors." *State of the Art within Task 33/IV*(Subtask C).
3. Aghamohammadi, M., J. Zarinchang and M. Yaghoubi (2001). *Performance of a Solar Water Pump In Southern Part of Iran*.
4. Ahmad, G. E. and J. Schmid (2002). "Feasibility study of brackish water desalination in the Egyptian deserts and rural regions using PV systems." *Energy Conversion and Management* **43**(18): 2641-2649.
5. Ali, M. T., H. E. S. Fath and P. R. Armstrong (2011). "A comprehensive techno-economical review of indirect solar desalination." *Renewable and Sustainable Energy Reviews* **15**(8): 4187-4199.
6. Al-Karaghouli, A., D. Renne and L. L. Kazmerski (2010). "Technical and economic assessment of photovoltaic-driven desalination systems." *Renewable Energy* **35**(2): 323-328.
7. Alghoul, M., P. Poovanaesvaran, K. Sopian and M. Sulaiman (2009). "Review of brackish water reverse osmosis (BWRO) system designs." *Renewable and Sustainable Energy Reviews* **13**(9): 2661-2667.
8. Alley, W. M. (2003). Desalination of ground water: Earth science perspectives, US Department of the Interior, *US Geological Survey*.
9. Angelino, G. and P. Colonna di Paliano (1998). "Multicomponent Working Fluids For Organic Rankine Cycles (ORCs)." *Energy* **23**(6): 449-463.
10. Badr, O., S. D. Probert and P. W. O'Callaghan (1985). "Selecting a working fluid for a Rankine-cycle engine." *Applied Energy* **21**(1): 1-42.
11. Bhanushali, D., S. Kloos and D. Bhattacharyya (2002). "Solute transport in solvent-resistant nanofiltration membranes for non-aqueous systems: experimental results and the role of solute–solvent coupling." *Journal of Membrane science* **208**(1): 343-359.
12. Bikaner, Central Ground Water Board. *District Groundwater Brochure*, Ministry of Water Resources, Government of India, March, 2009.
13. Bird, R. B., W. E. Stewart and E. N. Lightfoot (1960). *Transport Phenomena*, J. Wiley.
14. Brian, P. L. T. (1965). "Concentration Polar zation in Reverse Osmosis Desalination with Variable Flux and Incomplete Salt Rejection." *Industrial & Engineering Chemistry Fundamentals* **4**(4): 439-445.

15. Bruno, J., J. López-Villada, E. Letelier, S. Romera and A. Coronas (2008). "Modelling and optimisation of solar organic Rankine cycle engines for reverse osmosis desalination." *Applied Thermal Engineering* **28**(17-18): 2212-2226.
16. Centre, U. I. E. T., A. C. f. t. S. o. A. Zones and D. Lands (2001). Source Book of Alternative Technologies for Freshwater Augmentation in West Asia, UNEP/Earthprint.
17. Chaudry, M. A. (2002). "Water and ions transport mechanism in hyperfiltration with symmetric cellulose acetate membranes." *Journal of Membrane science* **206**(1): 319-332.
18. Cipollina, A., G. Micale and L. Rizzuti (2009). *Seawater desalination: conventional and renewable energy processes*, Springer.
19. Cussler, E. L. (1997). *Diffusion: Mass transfer in fluid systems*, Cambridge Univ Pr.
20. Davies, P. A. (2011). "A solar-powered reverse osmosis system for high recovery of freshwater from saline groundwater." *Desalination* **271**: 72-79.
21. Dawoud, M. A. (2012). "Environmental Impacts of Seawater Desalination: Arabian Gulf Case Study." International Journal of Environment and Sustainability (IJES) 1(3).
22. De Carvalho, P. C. M., D. B. Riffel, C. Freire and F. F. D. Montenegro (2004). "The Brazilian experience with a photovoltaic powered reverse osmosis plant." *Progress in Photovoltaics* **12**(5): 373-385.
23. De Munari, A., D. P. S. Capao, B. S. Richards and A. I. Schafer (2009). "Application of solar-powered desalination in a remote town in South Australia." *Desalination* **248**(1-3): 72-82.
24. Delgado-Torres, A. and L. García-Rodríguez (2007). "Preliminary assessment of solar organic Rankine cycles for driving a desalination system." *Desalination* **216**(1-3): 252-275.
25. Delgado-Torres, A., L. García-Rodríguez and V. Romero-Ternero (2007). "Preliminary design of a solar thermal-powered seawater reverse osmosis system." *Desalination* **216**(1-3): 292-305.
26. Delgado-Torres, A. M. and L. García-Rodríguez (2007). "Comparison of solar technologies for driving a desalination system by means of an organic Rankine cycle." *Desalination* **216**(1-3): 276-291.
27. Delgado-Torres, A. M. and L. García-Rodríguez (2007). "Status of solar thermal-driven reverse osmosis desalination." *Desalination* **216**(1-3): 242-251.
28. Delgado-Torres, A. M. and L. García-Rodríguez (2010). "Analysis and optimization of the low-temperature solar organic Rankine cycle (ORC)." *Energy Conversion and Management* **51**(12): 2846-2856.
29. Delgado-Torres, A. M. and L. García-Rodríguez (2010). "Preliminary design of seawater and brackish water reverse osmosis desalination systems driven by low-temperature solar organic Rankine cycles (ORC)." *Energy Conversion and Management* **51**(12): 2913-2920.

30. Delgado-Torres, A. M. and L. García-Rodríguez (2012). "Design recommendations for solar organic Rankine cycle (ORC)–powered reverse osmosis (RO) desalination." *Renewable and Sustainable Energy Reviews* **16**(1): 44-53.
31. DeZuane, J. (1997). *Handbook of drinking water quality*, Wiley.
32. Efraty, A., R. N. Barak and Z. Gal (2012). "Closed circuit desalination series no-2: new affordable technology for sea water desalination of low energy and high flux using short modules without need of energy recovery." *Desalination and water treatment* **42**(1-3): 189-196.
33. Efraty, A. (2012). "Closed circuit desalination series no-3: high recovery low energy desalination of brackish water by a new two-mode consecutive sequential method." *Desalination and water treatment* **42**(1-3): 256-261.
34. Efraty, A. (2012). "Closed circuit desalination series no-4: high recovery low energy desalination of brackish water by a new single stage method without any loss of brine energy." *Desalination and water treatment* **42**(1-3): 262-268.
35. Efraty, A. and Z. Gal (2012). "Closed circuit desalination series No 7: retrofit design for improved performance of conventional BWRO system." *Desalination and water treatment* **41**(1-3): 301-307.
36. El-Ghonemy, A. M. K. (2012). "Water desalination systems powered by renewable energy sources: Review." *Renewable and Sustainable Energy Reviews* **16**(3): 1537-1556.
37. Elimelech, M. and W. A. Phillip (2011). "The Future of Seawater Desalination: Energy, Technology, and the Environment." *Science* **333**(6043): 712-717.
38. Eltawil, M. A., Z. Zhengming and L. Yuan (2009). "A review of renewable energy technologies integrated with desalination systems." *Renewable and Sustainable Energy Reviews* **13**(9): 2245-2262.
39. Fritzmann, C., J. Löwenberg, T. Wintgens and T. Melin (2007). "State-of-the-art of reverse osmosis desalination." *Desalination* **216**(1-3): 1-76.
40. Forschung, S. P. (2009). "Solar Collector Factsheet De Dietrich Power7." (C1021).
41. Fraidenraich, N., O. Vilela and G. Lima (2012). "Specific energy consumption of PV reverse osmosis systems. Experiment and theory." Progress in Photovoltaics: Research and Applications.
42. García-Rodríguez, L. and J. Blanco-Gálvez (2007). "Solar-heated Rankine cycles for water and electricity production: POWERSOL project." *Desalination* **212**(1-3): 311-318.
43. García-Rodríguez, L. and A. Delgado-Torres (2007). "Solar-powered Rankine cycles for fresh water production." *Desalination* **212**(1-3): 319-327.
44. Gekas, V. and B. Hallström (1987). "Mass transfer in the membrane concentration polarization layer under turbulent cross flow : I. Critical literature review and adaptation of

existing sherwood correlations to membrane operations." *Journal of Membrane science* **30**(2): 153-170.

45. Ghermandi, A. and R. Messalem (2009). "Solar-driven desalination with reverse osmosis: the state of the art." *Desalination and water treatment* **7**(1-3): 285-296.
46. Ghiu, S. M. S. (2003). *Mass transfer of ionic species in direct and reverse osmosis processes*, University of South Florida.
47. Gilron, J., N. Gara and O. Kedem (2001). "Experimental analysis of negative salt rejection in nanofiltration membranes." *Journal of Membrane science* **185**(2): 223-236.
48. Goldberg, D. E. (1989). *Genetic algorithms in search, optimization, and machine learning*, Addison-wesley.
49. Green, M. A. (2006). *Third generation photovoltaics: advanced solar energy conversion*, Springer.
50. Green, M. A. and K. Emery (1993). "Solar cell efficiency tables." *Progress in Photovoltaics: Research and Applications* **1**(1): 25-29.
51. Herold, D., V. Horstmann, A. Neskakis, J. Plettner-Marliani, G. Piernavieja and R. Calero (1998). "Small scale photovoltaic desalination for rural water supply-demonstration plant in Gran Canaria." *Renewable Energy* **14**(1-4): 293-298.
52. Herold, D. and A. Neskakis (2001). "A small PV-driven reverse osmosis desalination plant on the island of Gran Canaria." *Desalination* **137**(1-3): 285-292.
53. Hickey, P. J. and C. H. Gooding (1994). "Mass transfer in spiral wound pervaporation modules." *Journal of Membrane science* **92**(1): 59-74.
54. Hickey, P. J. and C. H. Gooding (1995). "Erratum." *Journal of Membrane science* **98**(3): 293.
55. Ho, W. S. W. and K. K. Sirkar (1992). *Membrane Handbook*, Kluwer Academic Pub.
56. Jonsson, G. and C. Boesen (1977). "Concentration polarization in a reverse osmosis test cell." *Desalination* **21**(1): 1-10.
57. Kalogirou, S. A. (2005). "Seawater desalination using renewable energy sources." *Progress in energy and combustion science* **31**(3): 242-281.
58. Karagiannis, I. C. and P. G. Soldatos (2008). "Water desalination cost literature: review and assessment." *Desalination* **223**(1): 448-456.
59. Karellas, S., K. Terzis and D. Manolakos (2011). "Investigation of an autonomous hybrid solar thermal ORC–PV RO desalination system. The Chalki island case." *Renewable Energy* **36**(2): 583-590.
60. Kelley, L. C. and S. Dubowsky (2013). "Thermal control to maximize photovoltaic powered reverse osmosis desalination systems productivity." *Desalination* **314**(0): 10-19.

61. Kosmadakis, G., D. Manolakos, S. Kyritsis and G. Papadakis (2009). "Comparative thermodynamic study of refrigerants to select the best for use in the high-temperature stage of a two-stage organic Rankine cycle for RO desalination." *Desalination* **243**(1–3): 74-94.

62. Laborde, H. M., K. B. Franca, H. Neff and A. M. N. Lima (2001). "Optimization strategy for a small-scale reverse osmosis water desalination system based on solar energy." *Desalination* **133**(1): 1-12.

63. Lee, S., G. Amy and J. Cho (2004). "Applicability of Sherwood correlations for natural organic matter (NOM) transport in nanofiltration (NF) membranes." *Journal of Membrane science* **240**(1): 49-65.

64. Li, C., G. Kosmadakis, D. Manolakos, E. Stefanakos, G. Papadakis and D. Goswami (2013). "Performance investigation of concentrating solar collectors coupled with a transcritical organic Rankine cycle for power and seawater desalination co-generation." *Desalination* **318**: 107-117.

65. Li, C., S. Besarati, Y. Goswami, E. Stefanakos and H. Chen (2013). "Reverse osmosis desalination driven by low temperature supercritical organic rankine cycle." *Applied Energy* **102**(0): 1071-1080.

66. Li, C., Y. Goswami and E. Stefanakos (2013). "Solar assisted sea water desalination: A review." *Renewable and Sustainable Energy Reviews* **19**(0): 136-163.

67. Li, F., W. Meindersma, A. B. de Haan and T. Reith (2002). "Optimization of commercial net spacers in spiral wound membrane modules." *Journal of Membrane science* **208**(1-2): 289-302.

68. Libert, J. J. and A. Maurel (1981). "Desalination and renewable energies-a few recent developments." *Desalination* **39**: 363-372.

69. Liu, B., K. Chien and C. Wang (2004). "Effect of working fluids on organic Rankine cycle for waste heat recovery." *Energy* **29**(8): 1207-1217.

70. Loo, S.-L., A. G. Fane, W. B. Krantz and T.-T. Lim (2012). "Emergency water supply: A review of potential technologies and selection criteria." *Water Research* **46**(10): 3125-3151.

71. Lu, Y. Y., Y. D. Hu, X. L. Zhang, L. Y. Wu and Q. Z. Liu (2007). "Optimum design of reverse osmosis system under different feed concentration and product specification." *Journal of Membrane science* **287**(2): 219-229.

72. Luque, A. and S. Hegedus (2011). *Handbook of photovoltaic science and engineering*, John Wiley & Sons.

73. Madhawa Hettiarachchi, H., M. Golubovic, W. Worek and Y. Ikegami (2007). "Optimum design criteria for an organic Rankine cycle using low-temperature geothermal heat sources." *Energy* **32**(9): 1698-1706.

74. Maizza, V. and A. Maizza (2001). "Unconventional working fluids in organic Rankine-cycles for waste energy recovery systems." *Applied Thermal Engineering* **21**(3): 381-390.

75. Malaeb, L. and G. M. Ayoub (2011). "Reverse osmosis technology for water treatment: State of the art review." *Desalination* **267**(1): 1-8.

76. Manolakos, D., G. Kosmadakis, S. Kyritsis and G. Papadakis (2009). "On site experimental evaluation of a low-temperature solar organic Rankine cycle system for RO desalination." *Solar Energy* **83**(5): 646-656.

77. Manolakos, D., G. Papadakis, E. S. Mohamed, S. Kyritsis and K. Bouzianas (2005). "Design of an autonomous low-temperature solar Rankine cycle system for reverse osmosis desalination." *Desalination* **183**(1-3): 73-80.

78. Margazoglou, T. (2013). ‘’Design and Evaluation of a Stand-Alone Hybrid System with NF-RO Desalination Unit for Emergency Conditions’’ MSc, Aston University.

79. Mathers, C. (1977). "Upper limit of efficiency for photovoltaic solar cells." *Journal of Applied Physics* **48**: 3181.

80. Merten, U. (1963). "Flow Relationships in Reverse Osmosis." *Industrial & Engineering Chemistry Fundamentals* **2**(3): 229-232.

81. Mochizuki, S. and A. L. Zydney (1992). "Dextran transport through asymmetric ultrafiltration membranes: comparison with hydrodynamic models." *Journal of Membrane science* **68**(1-2): 21-41.

82. Mohamed, E. and G. Papadakis (2004). "Design, simulation and economic analysis of a stand-alone reverse osmosis desalination unit powered by wind turbines and photovoltaics." *Desalination* **164**(1): 87-97.

83. Mohamed, E., G. Papadakis, E. Mathioulakis and V. Belessiotis (2008). "A direct coupled photovoltaic seawater reverse osmosis desalination system toward battery based systems--a technical and economical experimental comparative study." *Desalination* **221**(1-3): 17-22.

84. Mohamed, E. S., G. Papadakis, E. Mathioulakis and V. Belessiotis (2005). "The effect of hydraulic energy recovery in a small sea water reverse osmosis desalination system; experimental and economical evaluation." *Desalination* **184**(1-3): 241-246.

85. Nafey, A. S. and M. A. Sharaf (2010). "Combined solar organic Rankine cycle with reverse osmosis desalination process: Energy, exergy, and cost evaluations." *Renewable Energy* **35**(11): 2571-2580.

86. Davies, P.A. (2011). "A solar-powered reverse osmosis system for high recovery of freshwater from saline groundwater." *Desalination* **271**(1-3): 72-79.

87. Peñate, B. and L. García-Rodríguez (2012). "Current trends and future prospects in the design of seawater reverse osmosis desalination technology." *Desalination* 284(0): 1-8.

88. Pérez-González, A., A. M. Urtiaga, R. Ibáñez and I. Ortiz (2012). "State of the art and review on the treatment technologies of water reverse osmosis concentrates." *Water Research* **46**(2): 267-283.

89. Peterson, E. L. and S. R. Gray (2012). "Effectiveness of desalination powered by a tracking solar array to treat saline bore water." *Desalination* **293**(0): 94-103.

90. Probstein, R. F. (1995). Physicochemical hydrodynamics, Wiley.

91. Qiu, T. and P. Davies (2011). "The scope to improve the efficiency of solar-powered reverse osmosis." *Desalination and water treatment* **35**(1-3): 14-32.

92. Qiu, T. Y. and P. A. Davies (2010). Solar-powered reverse osmosis: how efficient can it be? *3rd Oxford Water and Membranes Research Event*, Desalination and Water Treatment.

93. Qiu, T. Y., O. N. Igobo and D. P.A (2012). *DesaLink: Solar powered desalination of brackish groundwater giving high output and high recovery*. Desalination for the Environment Clean Water and Energy, Barcelona, Spain, Desalination and Water Treatment.

94. Richards, B. S. and A. I. Schafer (2003). "Photovoltaic-powered desalination system for remote Australian communities." *Renewable Energy* **28**(13): 2013-2022.

95. Riffel, D. B. and P. C. M. Carvalho (2009). "Small-scale photovoltaic-powered reverse osmosis plant without batteries: Design and simulation." *Desalination* **247**(1-3): 378-389.

96. Ruppel, W. and P. Wurfel (1980). "Upper limit for the conversion of solar energy." *Electron Devices, IEEE Transactions on* **27**(4): 877-882.

97. Sablani, S., M. Goosen, R. Al-Belushi and M. Wilf (2001). "Concentration polarization in ultrafiltration and reverse osmosis: a critical review." *Desalination* **141**(3): 269-289.

98. Saleh, B., G. Koglbauer, M. Wendland and J. Fischer (2007). "Working fluids for low-temperature organic Rankine cycles." *Energy* **32**(7): 1210-1221.

99. Schiermeier, Q. (2008). "Water: Purification with a pinch of salt." *Nature* **452**: 260-261.

100. Schuster, A., S. Karellas, E. Kakaras and H. Spliethoff (2009). "Energetic and economic investigation of Organic Rankine Cycle applications." *Applied Thermal Engineering* **29**(8-9): 1809-1817.

101. Schwarzenbach, R. P., B. I. Escher, K. Fenner, T. B. Hofstetter, C. A. Johnson, U. Von Gunten and B. Wehrli (2006). "The challenge of micropollutants in aquatic systems." *Science* **313**(5790): 1072-1077.

102. Schwinge, J., P. Neal, D. Wiley, D. Fletcher and A. Fane (2004). "Spiral wound modules and spacers:: Review and analysis." *Journal of Membrane science* **242**(1-2): 129-153.

103. SERVICE, R. F. (2006). "Desalination freshens up." *Science(Washington, D. C.)* **313**(5790): 1088-1090.

104. Shafaghat, R., H. Shafaghat, F. Ghanbari and P. S. Rezaei (2012) "Design of a MSF Desalination Plant to be supplied by a New Specific 42 MW Power Plant Located in Iran." *World Academy of Science, Enginnering and Technology* **62.**

105. Shannon, M. A., P. W. Bohn, M. Elimelech, J. G. Georgiadis, B. J. Marinas and A. M. Mayes (2008). "Science and technology for water purification in the coming decades." *Nature* **452**(7185): 301-310.

106. Shockley, W. and H. Queisser (1961). "Detailed Balance Limit of Efficiency of p n Junction Solar Cells." *Journal of Applied Physics* **32**: 510.

107. Soteris A, K. (2005). "Seawater desalination using renewable energy sources." *Progress in Energy and Combustion Science* **31**(3): 242-281.

108. Spiegler, K. and O. Kedem (1966). "Thermodynamics of hyperfiltration (reverse osmosis): criteria for efficient membranes." *Desalination* **1**(4): 311-326.

109. Subramani, A. and J. G. Jacangelo (2014). "Treatment technologies for reverse osmosis concentrate volume minimization: A review." *Separation and Purification Technology* **122**(0): 472-489.

110. Sutzkover, I., D. Hasson and R. Semiat (2000). "Simple technique for measuring the concentration polarization level in a reverse osmosis system." *Desalination* **131**(1-3): 117-127.

111. Tandon, A., S. K. Gupta and G. P. Agarwal (1994). "Modelling of protein transmission through ultrafiltration membranes." *Journal of Membrane science* **97**: 83-90.

112. Taylor, G. (1953). "Dispersion of soluble matter in solvent flowing slowly through a tube." *Proceedings of the Royal Society of London. Series A, Mathematical and Physical Sciences* **219**(1137): 186-203.

113. Tchanche, B. F., G. Papadakis, G. Lambrinos and A. Frangoudakis (2009). "Fluid selection for a low-temperature solar organic Rankine cycle." *Applied Thermal Engineering* **29**(11–12): 2468-2476.

114. Thomson, M. and D. Infield (2003). "A photovoltaic-powered seawater reverse-osmosis system without batteries." *Desalination* **153**(1-3): 1-8.

115. Trivich, D. and P. Flinn (1953). "Maximum Efficiency of Solar Energy Conversion by Quantum Process." *Solar Energy Research," University of Wisconsin Press, Madison, Wis., sec. VI*: 143-147.

116. Turek, M., J. Was and P. Dydo (2009). "Brackish water desalination in RO–single pass EDR system." *Desalination and Water Treatment* **7**(1-3): 263-266.

117. Tzen, E., K. Perrakis and P. Baltas (1998). "Design of a stand alone PV-desalination system for rural areas." *Desalination* **119**(1-3): 327-333.

118. Van Weert, F., J. van der Gun and J. Reckman (2009). "Global overview of saline groundwater occurrence and genesis." International Groundwater Resources Assessment Centre.

119. Vince, F., F. Marechal, E. Aoustin and P. Breant (2008). "Multi-objective optimization of RO desalination plants." *Desalination* **222**(1): 96-118.

120. Vos, A. D. (1980). "Detailed balance limit of the efficiency of tandem solar cells." *Journal of Physics D: Applied Physics* **13**(5): 839.

121. UN World Water Development Report – 2012

122. Water, U. (2012). The United Nations World Water Development Report 4, Earthscan.

123. Xu, P., T. Y. Cath, A. P. Robertson, M. Reinhard, J. O. Leckie and J. E. Drewes (2013). "Critical Review of Desalination Concentrate Management, Treatment and Beneficial Use." *Environmental Engineering Science* **30**(8): 502-514.

124. Xuesong, W. (1987). "Mass transfer and the fluidized bed intensification of reverse osmosis." *Desalination* **62**: 211-220.

125. Yamamoto, T., T. Furuhata, N. Arai and K. Mori (2001). "Design and testing of the organic Rankine cycle." *Energy* **26**(3): 239-251.

126. Zhou, Y. and R. S. Tol (2005). "Evaluating the costs of desalination and water transport." *Water Resources Research* **41**(3): W03003.

127. http://desaldata.com/

128. http://iom.edu/Reports/2004/Dietary-Reference-Intakes-Water-Potassium-Sodium-Chloride-and-Sulfate.aspx

129. http://zeenews.india.com/news/eco-news/uae-to-set-up-world-s-largest-solar-desalination-plant_892791.html

130. http://en.wikipedia.org/wiki/Solar_thermal_collector

APPENDICES

Appendix A: NaCl Salt Solution

A.1. Concentration and Conductivity

The conductivity of sodium chloride solution in principle increases with the concentration. For accurate conversion between these two, the data of conductivity and corresponding concentration was fitted by a third-order polynomial trendline (*Figure A.1*). In this study, the maximum concentration considered is 10000, which is the upper limit of concentration of the brackish water.

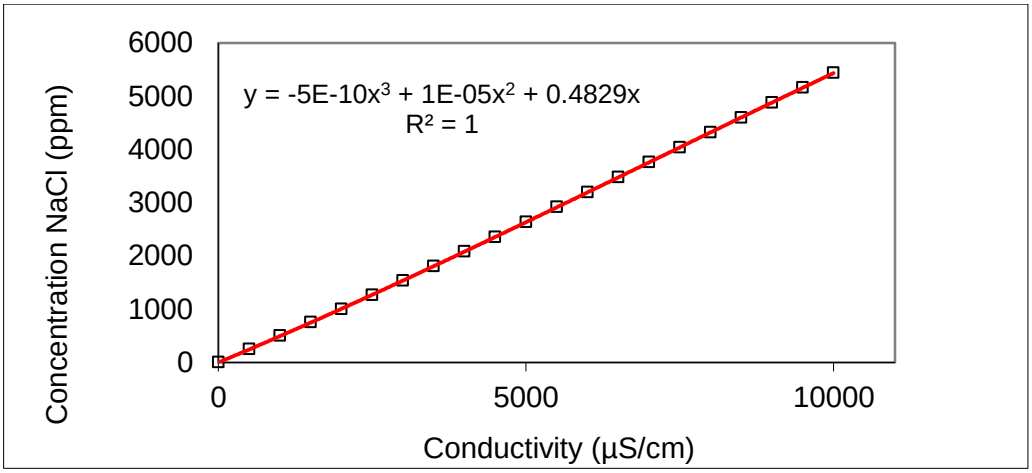

Figure A.1 Concentration vs. conductivity, from Dow Water & Process Solutions FILMTECTM Reverse Osmosis Membranes Technical Manual

A.2. Osmotic pressure of NaCl Solution

The osmotic pressure of salt solution is a function of the concentration, as well as the temperature. In the case of brackish water, it is a mix of different solutes, with NaCl being a major component. For experimental and modelling purposes, because the concentration is the essence of consideration factor, the use of NaCl solution with different concentrations within the brackish water concentration range is a common and reliable choice to allow

standardization and repeatability in test conditions and results. The osmotic pressure of NaCl solution is given by *Equation (A.1)*.

$$OsmP = i \cdot M \cdot R_{gas} \cdot T \quad \text{(A.1)}$$

where i is the dimensionless van't Hoff factor, M is the molarity, R_{gas} is the gas constant (0.0821 L·atm·K^{-1}·mol^{-1}) and T is the absolute temperature. In the case of 5000 ppm NaCl solution at room temperature of 25 °C ($i = 2$, $T = 298$ K, $M = 0.086$ mol·L^{-1}), the $OsmP$ is around 4 bar.

A.3. Variable brackish water sources

Table A.1 Brackish water compositions of different locations, from Margazoglou (2013)

Location	TDS	Ca^{2+}	Mg^{2+}	Na^{+}	K^{+}	SO_4^{2-}	Cl^{-}	pH
Pecos County, Texas, US	594	110	23	64	5.1	160	100	7.1
Eden Valley, Australia	1811	178	53	345	12	434	533	7.86
West Tahta, Egypt	4453	12	7	53	0.3	24	46	7.2
Haryana State, India	4685	90	70	648	12	940	863	7.6
Qinghai, China	969	51	81	109	9	273	83	7.97
Detritic aquifer, Spain	969	51	81	109	9	273	83	7.97

Appendix B: Mass Transfer in RO Module

B.1. Dispersion in RO SWM module

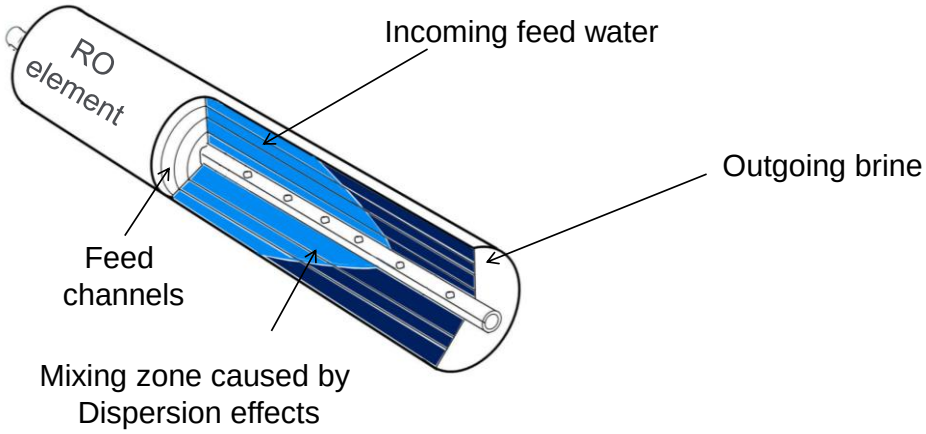

Figure A.2 Dispersion phenomena in purging phase of batch-RO operation

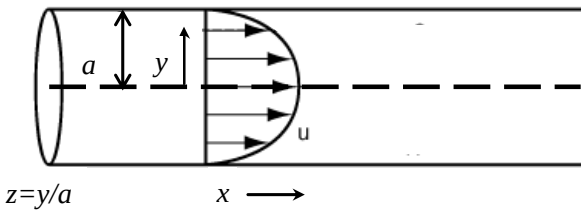

Figure A.3 The coordinates related to the series dispersion equations, Eqs.(5.11)-(5.20)

B.2. CP parameters fit MATLAB code

RLS_BSQ_linear(1).m

```
function [fval] = RLS_BSQ_linear(x,Re,Sc,Sh)

a = x(1);
alpha = x(2);
beta = x(3);

K = 4.685; % tuning constant for bisquare weight function

n = 5;

residual = zeros(n,1);
residual_adj = zeros(n,1);
u = zeros(n,1);
objF = 0.0;

for data = 1 : n
```

```
    residual(data,1) = Sh(data,1) - a*(Re^alpha)*(Sc^beta);

end

h = leverage(residual,'linear');
s = mad(residual,1)/0.6745;

for i = 1 : n

    residual_adj(i,1) = residual(i,1)/sqrt(1-h(i,1));
    u(i,1) = residual_adj(i,1)/(K*s);

end

for j = 1 : n

    if abs(u(i,1)) < 1
        objF = objF + (((K*s)^2)/6)*(1-(1-(u(j,1))^2)^3);
    else
        objF = objF + ((K*s)^2)/6;
    end

end

fval = objF;

end


[x fval]=fmincon(@(x)OLS(x,re,sh),x0,[],[],[],[],lb,ub,[],options)

optimset

x0=xlsread('x0.xlsx')

lb=xlsread('lb.xlsx')

x0=xlsread('x0.xlsx')

lb=xlsread('lb.xlsx')

ub=xlsread('ub.xlsx')

sh=xlsread('Sh.xlsx'

sh=xlsread('Sh.xlsx')

re=xlsread('Re.xlsx')

x0=xlsread('x0.xlsx')

x0=xlsread('C:\destop\matlab\x0.xlsx')

x0=xlsread('H:\Matlab\x0.xlsx')

lb=xlsread('lb.xlsx')
```

```
lb=xlsread('H:\Matlab\lb.xlsx')

ub=xlsread('H:\Matlab\ub.xlsx')

sh=xlsread('H:\Matlab\Sh.xlsx')

re=xlsread('H:\Matlab\Re.xlsx')

options=optimset('Display','iter','TolFun',1e-8,'TolX',1e-
6,'Algorithm','interior-point','FinDiffType','central')

[x fval]=fmincon(@(x)OLS(x,re,sh),x0,[],[],[],[],lb,ub,[],options)

[fval]=fmincon(@(x)RlS_BSQ_linear(x,re,sh),x0,[],[],[],[],lb,ub)

[x fval]=fmincon(@(x)RlS_BSQ_linear(x,re,sh),x0,[],[],[],[],lb,ub)

[fval]=fmincon(@RlS_BSQ_linear(x,re,sh),x0,[],[],[],[],lb,ub)

[fval]=fmincon(@(x)RlS_BSQ_linear(x,re,sh),x0,[],[],[],[],lb,ub)

x0

x0(1)=0.6

[x fval]=fmincon(@(x)RlS_BSQ_linear(x,re,sh),x0,[],[],[],[],lb,ub)

[x
fval]=fmincon(@(x)RlS_BSQ_linear(x,re,sh),x0,[],[],[],[],lb,ub,[],op
tions)

[x fval]=fmincon(@(x)OLS(x,re,sh),x0,[],[],[],[],lb,ub,[],options)

sh=xlsread('H:\Matlab\Shch.xlsx')

re=xlsread('H:\Matlab\Rech.xlsx')

[x
fval]=fmincon(@(x)RlS_BSQ_linear(x,re,sh),x0,[],[],[],[],lb,ub,[],op
tions)

[x fval]=fmincon(@(x)OLS(x,re,sh),x0,[],[],[],[],lb,ub,[],options)
```

Appendix C: System Components Details

C.1. Sensor details and calibration

Detailed information on the sensors specifications is summarised and presented in *Table A.2*. Conductivity probe was calibrated by using HANNA HI 7030M 12.88 mS conductivity calibration buffer solution.

Table A.2 Measurement sensors details

Instrument	Manufacturer	Model	Calibration	Range	Accuracy
Flow meter (feed solution)	Gems	Turbine type 173937C	Yes	1–10 l/min	±3%
Flow meter (permeate)	Gems	Turbine type 212460E	Yes	0.12–3 l/min	±3%
Conductivity probe (feed flow)	Cole-Parmer	19500-50	Yes	10–10000 µs/cm	±0.1%
Conductivity probe (permeate flow)	Cole-Parmer	Flow through 19500-58	Yes	10–1000 µs/cm	±0.15%
Pressure transmitter (water)	Gems	1000BGB1 601A3UA	No	0–16 bar	±0.25%
Pressure transmitter (air)	Gems	3100B0016 G01B000	No	0–16 bar	±0.25%
Pressure gauge (water)	Wika	7075597	No	0–25 bar	±0.15%
Temperature	Eutech	COND 500	No	0–100 ºC	±0.5ºC
Feed pump	Hozelock	HOZ2826 2826	No	1.1 bar, max flow 2200 l/min	—
Re-circulation pump	Wilo 500	4132507	No	max flow 50 l/min	—
Air compressor	Stanley	GCDV4G4S CR006	No	max pressure 10 bar	—

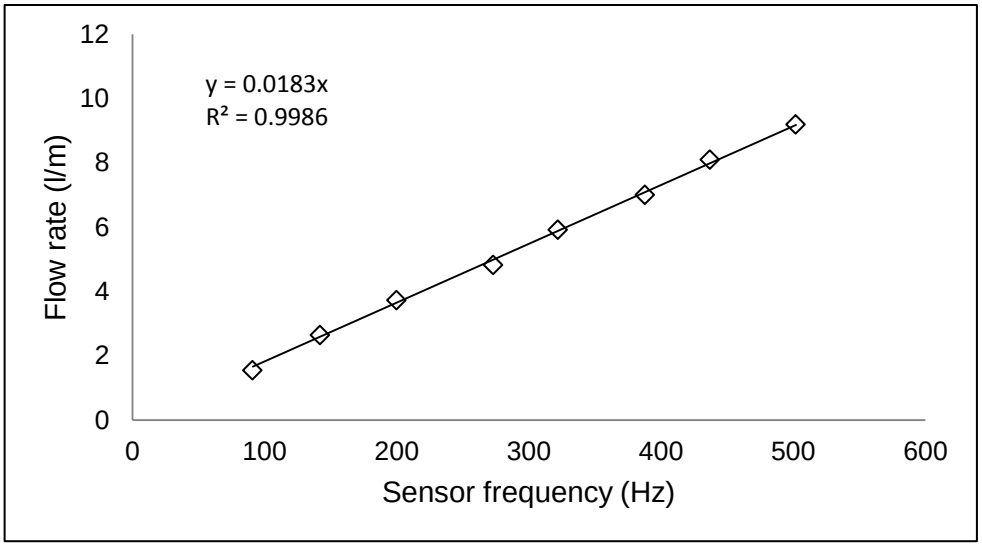

Figure A.3 Concentrate flow turbine flow rate sensor calibration

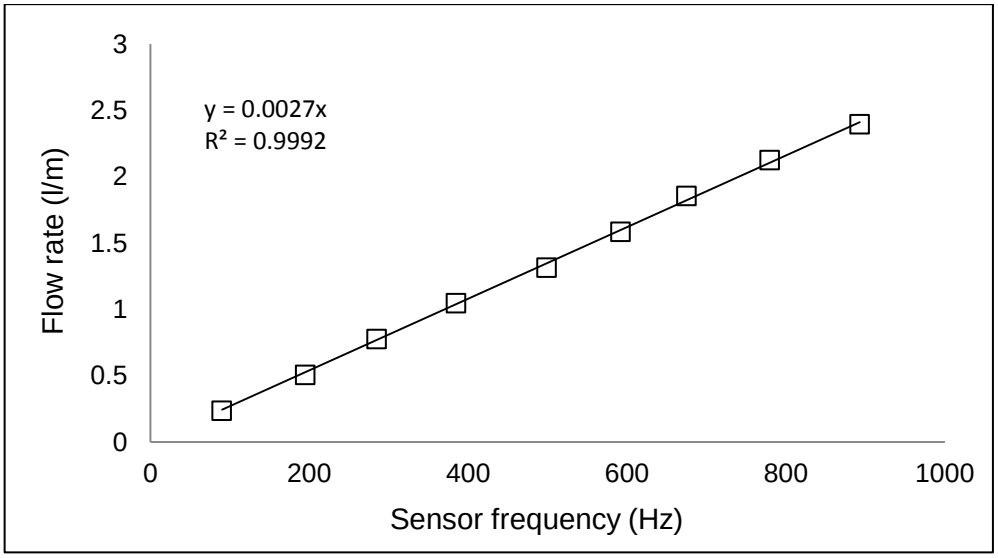

Figure A.4 Permeate flow turbine flow rate sensor calibration

C.2. Experimental error analysis

Experimental errors that were caused by either measurement means or calculated figures were considered during the whole study, *Table A.3* is an example.

Table A.3 Experimental errors for the KS model in RO SWM experiments

Parameter	Measurement method/Calculate equation	Experimental error
C_b	Direct measurement, equals C_f	0.1%
C_p	Direct measurement	0.15%
ΔP	Direct measurement	0.25%
V_p	Direct measurement	0.2%
Q_p	V_p/ time	0.2%
J_v	Q_p/A_{mem}	0.55%
A	$J_v/\Delta P$	0.45%
ΔC	C_{feed}-C_p	0.25%
C_{avg}	½(C_f+C_p)	0.25%
R_o	$R_o = \frac{C_b - C_p}{C_b}$	0.25%

Appendix D: System modelling

D.1. Hermite polynomials

$He_0(x) = 1$

$He_1(x) = x$

$He_2(x) = x^2 - 1$

$He_3(x) = x^3 - 3x$

$He_4(x) = x^4 - 6x^2 + 3$

$He_5(x) = x^5 - 10x^3 + 15x$

D.2. ROSA predictions for permeate flow

The formulations (i.e. *Eqs 7.17–7.18*) are commonly used by commercial RO modelling packages such as ROSA. During the initial modelling stage, ROSA provided by the membrane manufacturer DOW® was considered, since it has been widely used for RO system design and evaluation. ROSA can predict product rate and concentration for a known RO system configuration, such as RO module and element numbers, under certain conditions such as feed flow rates and concentrations, feed pressures, and objective recovery ratios.

Tests of conventional continuous RO operation were conducted. The feed solution of 5000 ppm was used. In order to evaluate the accuracy of the physical models as implemented in ROSA for a range of operating conditions (*Table A.4*). Experimental points were collected and modelling was performed accordingly.

Table A.4 Operation conditions of the test points

Test points	1	2	3	4	5	6	7	8	9	10
Feed pressure (bar)	5.5	6	7	8	9	10	11	12	13	13.5
Feed flow rate (l/min)	10.3	10	9.4	9	8.6	8	7.7	7.2	6.8	6.4

Figure A.5 shows the comparison of the permeate flows measured in the experiments and predicted by ROSA. The ROSA modelling consistently overestimated the permeate flows with the only outlier being the case at 5 bar, the lowest operation pressure investigated here. Nevertheless, the agreement between the experiments and predictions is fairly good. On the other hand, it is clearly demonstrated in *Figure A.6* that the discrepancies between the experimental and predicted permeate concentrations are considerably larger.

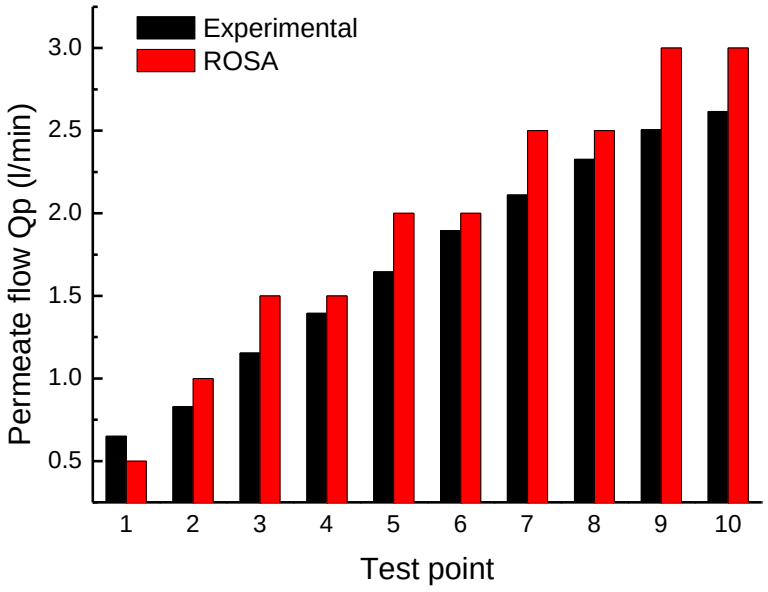

Figure A.5 Permeate flow rates comparison

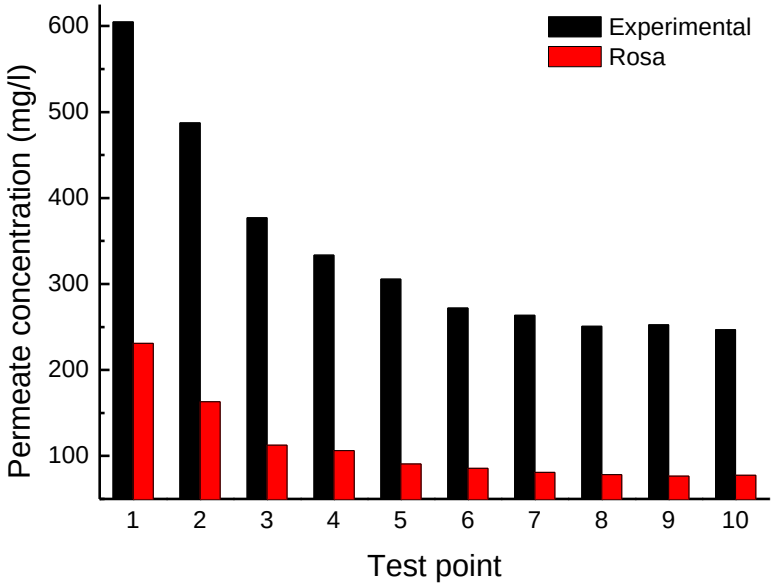

Figure A.6 Permeate flow concentration comparison

From the above results it follows that despite being one of the most popular tools for designing RO desalination systems, ROSA cannot be used to predict accurately either the product flow rate or concentration of the unsteady batch-RO operation adopted by DesaLink. The reason for this primarily resides in the theoretical models implemented in the software. In other words, *Eqs. (7.17–7.18)* cannot be utilized to predict the performance of DesaLink, because the feed water pressure and concentration are instantly changing along the batch-mode process, which cannot be expected to be described by the steady mode equations (i.e. *Eqs. 7.17–7.18*). Furthermore, within the DesaLink design the permeate flow rate and concentration (system outputs) have marked effects on the operation pressure and feed flow (system inputs), making the whole system too complex to be modelled by any simple linear regression to the steady mode relationships *(Eqs. 7.17–7.18)*. More importantly, the desired model for the RO module (and any other module) should not only provide an accurate prediction of the performance under various conditions but also be compatible with other component models to constitute the complete DesaLink Simulink model.

Thus, a different modelling approach was adopted to take into account the influence of the pressure, concentration and feed flow rate on the permeate flow. In these new models

the permeate flow rate and concentration are governed by the same input variables as suggested in *Eqs 7.17* and *7.18* but with different mathematical expressions.

D.3. Solar collector datasheet

De Dietrich POWER7:

TÜVRheinland®
DIN CERTCO

Summary of EN 12975 Test Results, annex to Solar KEYMARK Certificate Kurzfassung EN 12975 Test Ergebnisse, Anlage zum Solar KEYMARK-Zertifikat Synthèse des résultats d'essais selon EN 12975, annexe au certificat Solar KEYMARK	**Registration No.** Registernummer Numéro d'enregistrement	**011-7S412 R**
	Date / Datum / Date	12.03.2009

Company / Firma / Société	De Dietrich Thermique		**Country** / Land / Pays	France
Street / Straße / Rue	57, rue de la Gare		**Website**	
Postal Code, Place / PLZ, Ort / Code postal, Place	67580	Mertzwiller	**E-mail**	
			Tel. / Fax	33 390552913 / 388802709

Collector Type / Kollektorbauart / type de capteur	Evacuated tube / Vakuumröhrenkollektor / Capteur à tube sous vide
To be roof integrated / im Dach eingegliedert zu sein / pour etre intégré dans le toit	No / nein / non

Product name Produktbezeichnung Modèle	**Aperture area** Aperturfläche Superficie d'entrée	**Gross length** Länge (Aussenmass) Longueur hors tout	**Gross width** Breite (Aussenmass) Largeur hors tout	**Gross height** Höhe (Aussenmass) Epaisseur hors tout	**Gross area** Bruttofläche Superficie hors-tout	**Power output per collector unit** Leistung je Kollektormodul Puissance fournie par le capteur {note 1} G = 1000 W/m² Tm-				
						0 K	10 K	30 K	50 K	70 K
	[m²]	[mm]	[mm]	[mm]	[m²]	[W]	[W]	[W]	[W]	[W]
De Dietrich POWER7	0.80	1'700	610	99	1.04	596	584	559	534	509
De Dietrich POWER10	1.14	1'700	850	99	1.45	852	834	799	763	727
De Dietrich POWER15	1.72	1'700	1'250	98	2.13	1'278	1'252	1'199	1'146	1'092

Collector efficiency parameters related to aperture area Kollektorleistungsparameter bezogen auf die Aperturfläche {note 1} Paramètres de performances thermiques rapportées à la superficie d'entrée	η_{0a}	0.745	-
	a_{1a}	1.53	W/(m²K)
	a_{2a}	0.0003	W/(m²K²)
Stagnation temperature / Stagnationstemperatur / Temperature de stagnation {note 2}	t_{stg}	183	°C
Effective thermal capacity / Effektive Wärmekapazität / Capacité thermique effective	$c_{eff} = C/A_a$	14.2	kJ/(m²K)
Max. operation pressure / max. Betriebsdruck / pression d'opération de maximum {note 3}	p_{max}	1000	kPa

Incidence angle modifiers $K_\theta(\theta)$ Einfallswinkelkorrekturfaktoren $K_\theta(\theta)$ Facteur d'angle d'incidence $K_\theta(\theta)$	G_{DIF}/G_{TO} T min		θ_T / θ_L	50°	*10°*	*20°*	*30°*	*40°*	*60°*	*70°*
			$K_\theta(\theta_T)$	0.93	*0.98*	*0.92*	*0.87*	*0.88*	*1.09*	*1.04*
	0.12	0.14	$K_\theta(\theta_L)$	0.95	*1.00*	*1.00*	*0.99*	*0.98*	*0.88*	*0.75*
G_{DIF}/G_{TOT}: min&max while measuring / min&max während messen / min&max pendant qu'essayant					***Optional values** / Angaben optional / Données*					

Testing Laboratory / Prüflaboratorium / Laboratoire d'essais	SPF, CH-8640 Rapperswil
Website	www.solarenergy.ch
Test report id. number / Prüberichtsnummer / numéro d'identification de rapport des essais	C989LPEN, C989QPEN, C1021LPEN
Date of test report / Datum des Prüfberichts / date de rapport des essais	12-03-2009 / 12-03-2009 / 12-03-2009
Perf. test method / Leistungstestmethode / méthode d'essai de performance	EN 12975-2 6.1.4 (outdoor/außen/extérieur)

Comments of testing laboratory / Kommentare des Prüflaboratoriums / commentaires du laboratoire d'essais :

Note 1	**Test conditions** Prüfbedingungen conditions d'essais	**Fluid** Flüssigkeit Liquide	Water-Glycole Wasser-Glykol Eau-glycole	**Flow rate** Durchfluss Débit	0.037	kg/s per m²
Note 2	**Irradiance /** Bestrahlungsstärke / Irradiance **G_S=1000 W/m²** **Ambient temperature** / Umgebungstemperatur / Température ambiante: **t_a=30 °C**					
Note 3	**Given by manufacturer** / Herstellerangaben / Donnée par le fabricant